



Expanding the Y Dwarf Census with *Spitzer* Follow-up of the Coldest CatWISE Solar Neighborhood Discoveries

Aaron M. Meisner¹ , Dan Caselden², J. Davy Kirkpatrick³ , Federico Marocco^{3,4,13} , Christopher R. Gelino³, Michael C. Cushing⁵ , Peter R. M. Eisenhardt⁴, Edward L. Wright⁶ , Jacqueline K. Faherty⁷ , Renata Koontz⁸, Elijah J. Marchese⁸, Mohammed Khalil^{3,9,10}, John W. Fowler¹¹, and Edward F. Schlafly¹² 

¹ NSF's National Optical-Infrared Astronomy Research Laboratory, 950 N. Cherry Avenue, Tucson, AZ 85719, USA; ameisner@noao.edu

² Gigamon Applied Threat Research, 619 Western Avenue, Suite 200, Seattle, WA 98104, USA

³ IPAC, Mail Code 100-22, California Institute of Technology, 1200 E. California Boulevard, Pasadena, CA 91125, USA

⁴ Jet Propulsion Laboratory, California Institute of Technology, 4800 Oak Grove Drive, M/S 169-327, Pasadena, CA 91109, USA

⁵ Department of Physics and Astronomy, University of Toledo, 2801 West Bancroft Street, Toledo, OH 43606, USA

⁶ Department of Physics and Astronomy, UCLA, 430 Portola Plaza, Box 951547, Los Angeles, CA 90095-1547, USA

⁷ Department of Astrophysics, American Museum of Natural History, Central Park West at 79th Street, NY 10024, USA

⁸ University of California, Riverside, 900 University Avenue, Riverside, CA 92521, USA

⁹ International College, P.O. Box 113-5373 Hamra, Bliss Street, Beirut, Lebanon

¹⁰ Stanford University, 450 Serra Mall, Stanford, CA 94305, USA

¹¹ 230 Pacific Street, Apt. 205, Santa Monica, CA 90405, USA

¹² Lawrence Berkeley National Laboratory, Berkeley, CA 94720, USA

Received 2019 October 17; revised 2019 November 25; accepted 2019 November 27; published 2020 January 28

Abstract

We present *Spitzer* 3.6 and 4.5 μm follow-up of 170 candidate extremely cool brown dwarfs newly discovered via the combination of *Wide-field Infrared Survey Explorer* (*WISE*) and NEOWISE imaging at 3–5 μm . CatWISE, a joint analysis of archival *WISE* and NEOWISE data, has improved upon the motion measurements of AllWISE by leveraging a $>10\times$ time baseline enhancement, from 0.5 yr (AllWISE) to 6.5 yr (CatWISE). As a result, CatWISE motion selection has yielded a large sample of previously unrecognized brown dwarf candidates, many of which have archival detections exclusively in the *WISE* 4.6 μm (*W2*) channel, suggesting that they could be both exceptionally cold and nearby. Where these objects go undetected in *WISE* *W1* (3.4 μm), *Spitzer* can provide critically informative detections at 3.6 μm . Of our motion-confirmed discoveries, 17 have a best-fit *Spitzer* [3.6]–[4.5] color most consistent with spectral type Y. It is likely that CWISEP J144606.62–231717.8 ($\mu \approx 1''.3 \text{ yr}^{-1}$) is the reddest, and therefore potentially coldest, member of our sample with a very uncertain [3.6]–[4.5] color of $3.71 \pm 0.44 \text{ mag}$. We also highlight our highest proper-motion discovery, WISEA J153429.75–104303.3, with $\mu \approx 2''.7 \text{ yr}^{-1}$. Given that the prior list of confirmed and presumed Y dwarfs consists of just 27 objects, the *Spitzer* follow-up presented in this work has substantially expanded the sample of identified Y dwarfs. Our new discoveries thus represent significant progress toward understanding the bottom of the substellar mass function, investigating the diversity of the Y dwarf population, and selecting optimal brown dwarf targets for *James Webb Space Telescope* spectroscopy.

Unified Astronomy Thesaurus concepts: [Brown dwarfs \(185\)](#); [Y dwarfs \(1827\)](#); [Solar neighborhood \(1509\)](#); [T dwarfs \(1679\)](#); [Proper motions \(1295\)](#)

Supporting material: machine-readable tables

1. Introduction

How complete is our census of the Sun's closest neighbors? How far does the population of substellar objects born like stars extend into the planetary-mass regime? The *Wide-field Infrared Survey Explorer* (*WISE*; Wright et al. 2010), with its unique full-sky sensitivity at 4.6 μm , has unrivaled potential to answer these open questions by identifying the coldest brown dwarfs down to planetary masses. *WISE*-based discoveries already include the three nearest known brown dwarfs, among which is the coldest known brown dwarf (*WISE* 0855–0714), an $\sim 250 \text{ K}$ planetary-mass object (Luhman 2014a, 2014b, 2013). Wright et al. (2014) estimated that between 3 and 34 *WISE* 0855–0714 analogs should be detectable with *WISE*, yet only perhaps one such candidate has thus far been found (Marocco et al. 2019).

The coolest brown dwarfs revealed by *WISE* will be key *James Webb Space Telescope* (*JWST*; Gardner et al. 2006) targets, overlapping in mass and temperature with extrasolar giant planets and providing simplified laboratories for modeling planetary atmospheres, free of the irradiation and contaminating glare from a primary star. Indeed, *WISE* has already established the existence of a new brown dwarf spectral class with $T_{\text{eff}} \lesssim 500 \text{ K}$ (Y dwarfs; Cushing et al. 2011; Kirkpatrick et al. 2011). Although prior *WISE* brown dwarf searches have been highly successful (e.g., Cushing et al. 2011; Kirkpatrick et al. 2011, 2012, 2014, 2016; Griffith et al. 2012; Mace et al. 2013a; Luhman 2014a; Pinfield et al. 2014a; Schneider et al. 2016; Kuchner et al. 2017; Burningham 2018; Tinney et al. 2018), the Y dwarf census has stagnated in recent years at a sample size of just $\sim 25\text{--}30$ objects.

The discoveries of nearly all known Y dwarfs can be traced back to *WISE*. The *WISE* 3.4 μm (*W1*) and 4.6 μm (*W2*) bands were designed for optimal sensitivity to the coldest brown dwarfs (Mainzer et al. 2011b), such that selecting for large

¹³ NASA Postdoctoral Program Fellow.

$W1$ – $W2$ color is a highly effective search strategy (e.g., Kirkpatrick et al. 2011, 2012; Griffith et al. 2012). Even more powerful is the combination of *WISE*-based color and motion criteria, eliminating stationary extragalactic contaminants (e.g., Luhman 2014a, 2014b). Pinfield et al. (2014b) illustrated that faint, unrecognized Y dwarfs remain to be found in the *WISE* imaging, identifiable with novel search criteria using *WISE* data alone. Follow-up techniques such as methane on/off imaging (Tinney et al. 2012, 2018) and adaptive optics imaging (Liu et al. 2012; Dupuy et al. 2015) have also proven effective at pinpointing Y dwarfs among the numerous *WISE* solar neighborhood discoveries.

Our CatWISE analysis (Eisenhardt et al. 2019) represents a major step toward realizing the entire *WISE* data set’s full sensitivity for brown dwarf discovery. Mining the vast *WISE* imaging archive to its faintest depths is a formidable challenge, and prior *WISE* motion searches have generally been limited by restricting to bright single-exposure detections and/or the short half-year time baseline of 2010–2011 observations. CatWISE pushes several magnitudes deeper than the foregoing *WISE*-based motion surveys by jointly analyzing 4 yr of *WISE* and NEOWISE (Mainzer et al. 2011a, 2014) data spanning the 2010–2016 time period. CatWISE thereby provides long time baseline *WISE* proper motions for roughly a billion mid-infrared sources over the full sky.

Using the CatWISE Preliminary Catalog¹⁴ and drawing upon well-established faint moving-object selection/confirmation techniques (e.g., Lépine et al. 2002), we have performed an extensive motion-based search for previously undiscovered solar neighborhood constituents. As part of our ground- and space-based follow-up program, we have obtained *Spitzer* IRAC (Fazio et al. 2004; Werner et al. 2004) photometry of ~ 170 newly discovered brown dwarf candidates suspected of being extremely cold and/or nearby. At CatWISE depths, the hallmark of such targets is the presence of a moving $4.6 \mu\text{m}$ ($W2$) source with no firmly detected $3.4 \mu\text{m}$ ($W1$) counterpart.

Detectable motion and a $W2$ magnitude alone are insufficient to estimate the basic parameters of most immediate interest for these brown dwarf candidates: spectral type, temperature, luminosity, distance, and near-infrared (NIR) flux. The mid-infrared color, whether $W1$ – $W2$ from *WISE* or [3.6]–[4.5] from *Spitzer*, represents a critical diagnostic in obtaining estimates for all of these quantities, as both colors tend to increase monotonically toward later spectral types beyond mid-T (e.g., Patten et al. 2006; Kirkpatrick et al. 2011). For our targets with $W1$ nondetections, *Spitzer* provides the only opportunity to measure a mid-infrared color. With spectral type estimates based on IRAC colors in hand, luminosity, distance, and NIR flux estimates also follow.

Based on the *Spitzer* follow-up we present in this work, many of our discoveries have photometric spectral type estimates placing them within the 20 pc volume and/or very red [3.6]–[4.5] colors most consistent with spectral type Y. Among these, CWISEP J144606.62–231717.8 (hereafter CWISEP 1446–2317) stands out with an exceptionally large but highly uncertain [3.6]–[4.5] color of 3.71 ± 0.44 mag.

In Section 2 we briefly summarize the relevant characteristics of the *WISE* and NEOWISE missions. In Section 3 we provide a concise overview of CatWISE. In Section 4 we describe our selection of brown dwarf candidate targets for follow-up *Spitzer* photometry. In Section 5 we present the basic

properties of our *Spitzer* photometry target sample. In Section 6 we explain our *Spitzer* observing strategy. In Section 7 we present our *Spitzer* color measurements. In Section 8 we combine *WISE* and *Spitzer* astrometry to confirm the motions of our brown dwarf candidates. In Section 9 we present complementary NIR photometry drawn from our ground-based follow-up observations and archival data sets. We discuss the combined implications of our photometric and astrometric analyses in Section 10. We conclude in Section 11.

2. WISE/NEOWISE Overview

Launched into low-Earth orbit in late 2009, *WISE* is a satellite-borne 40 cm aperture telescope. During early and mid-2010, *WISE* mapped the entire sky in four broad infrared bandpasses centered at 3.4 ($W1$), 4.6 ($W2$), 12 ($W3$), and 22 ($W4$) μm . Although observations in the two longest wavelength channels were discontinued by late 2010 due to cryogen depletion, *WISE* kept observing in $W1$ and $W2$ until 2011 February as part of the NEOWISE mission (Mainzer et al. 2011a). *WISE* was placed into hibernation from 2011 February until 2013 December, at which point it recommenced surveying in $W1$ and $W2$ thanks to the NEOWISE-Reactivation (NEOWISE-R; Mainzer et al. 2014) mission extension. *WISE* has continued observations since reactivation to this writing (2019 October). A typical sky location is observed during an ~ 1 day time period once every 6 months, and *WISE* has now performed a total of more than 13 complete sky passes in $W1$ and $W2$. The high quality of $W1$ and $W2$ imaging has remained essentially unchanged throughout the entire *WISE* lifetime (Mainzer et al. 2014; Cutri et al. 2015).

3. CatWISE

Although NEOWISE-R has now supplied the vast majority of $W1/W2$ observations, the mission itself does not provide any coadded data products optimized for science beyond the inner solar system. As a result, AllWISE (Cutri et al. 2013) has remained the definitive coadded *WISE* catalog for many years, despite incorporating only the ~ 13 months of prehibernation *WISE* imaging.

Our CatWISE archival data analysis program (Eisenhardt et al. 2019) has combined ~ 4 yr of 2010–2016 *WISE*/NEOWISE data to build a deeper, longer time baseline successor to AllWISE at 3 – $5 \mu\text{m}$. Whereas the AllWISE Source Catalog directly modeled *WISE* single-exposure images, CatWISE instead applies the AllWISE cataloging software to “unWISE” coadds (Lang 2014) as a computational convenience. By detecting $W1/W2$ sources in 4 yr depth unWISE stacks (Meisner et al. 2018a), CatWISE extracts 5σ sources to Vega magnitudes of $W1 = 17.67$ and $W2 = 16.47$, ~ 0.6 mag deeper than AllWISE.¹⁵ CatWISE fits apparent linear motions for every source using a set of “time-resolved” unWISE coadds (Meisner et al. 2018b, 2018c). Each time-resolved coadd stacks the ~ 1 day of *WISE* frames together at a given sky location during a single sky pass, sampling the motion at 6 month intervals. Such coaddition results in effectively no loss of motion information for objects in the solar neighborhood¹⁶ ($\mu \lesssim 10'' \text{ yr}^{-1}$). By virtue of its

¹⁵ Magnitudes and colors quoted throughout this paper are in the Vega system unless otherwise noted.

¹⁶ The time-resolved unWISE coaddition would only begin to incur significant smearing of fast-moving sources at linear motions of order $100'' \text{ yr}^{-1}$. For comparison, the largest proper motion of any known star or brown dwarf is $10''4 \text{ yr}^{-1}$ (Barnard’s Star).

¹⁴ <https://catwise.github.io>

$>10\times$ extended time baseline and $4\times$ input imaging increase, CatWISE derives motions an order of magnitude more accurate than those of AllWISE for ~ 900 million sources over the full sky.¹⁷ We should therefore expect CatWISE motion and/or color selections to reveal many nearby brown dwarfs not previously identified with AllWISE. This includes objects below the AllWISE detection limit and also those with AllWISE motion measurements too noisy to be statistically significant.

Artifact flagging is a key ingredient in WISE-based rare-object searches, where anomalies due to bright stars and blending dramatically outnumber the astrophysical sources of interest. Our brown dwarf searches take advantage of two complementary artifact-flagging capabilities provided by CatWISE: (1) CC flags inherited from AllWISE via cross-match and (2) unWISE `ab_flags`, similar to the CC flags but available even in cases when a CatWISE source has no AllWISE counterpart.¹⁸

4. *Spitzer* Target Selection

Our *Spitzer* follow-up observations presented throughout this work were acquired as part of program 14034 (hereafter p14034; PI: Meisner). At the time of our Cycle 14 proposal submission (2018 March), *Spitzer*'s final observations were expected to take place on 2019 November 30. Given *Spitzer*'s impending retirement, we sought to fill our target list with the most exceptional WISE-based cold brown dwarf candidates selected by any/all means necessary, and as a result, virtually no emphasis was placed on sample uniformity/homogeneity.

Additionally, our search for *Spitzer* targets was performed as part of a larger effort to fully mine CatWISE (and unWISE/AllWISE) for moving-object discoveries, including earlier-type candidates accessible via our ground-based photometric/spectroscopic observing programs. Only a subset of our brown dwarf searches were specifically tailored to supply targets for our p14034 *Spitzer* campaign. Through the combination of multiple searches described in Sections 4.1–4.3, we discovered (and visually confirmed) a total of ~ 2500 previously unpublished moving objects. Most of these ~ 2500 discoveries are not appropriate *Spitzer* targets because they can be sensibly followed up from ground-based facilities. Discussion of additional CatWISE motion discoveries beyond those followed up via *Spitzer* p14034 is deferred to future papers.

We obtained p14034 observations for only the subset of our moving-object discoveries that would be extremely difficult to follow up from any platform other than *Spitzer* and/or for which *Spitzer* $3.6\ \mu\text{m}$ (hereafter ch1) and $4.5\ \mu\text{m}$ (hereafter ch2) photometry provides a critically informative diagnostic. We therefore selected only discoveries falling into one or more of the following categories when constructing our p14034 target list.

1. Nonstationary objects detected exclusively in *W2*. Detectable motion ($\mu \gtrsim 200\ \text{mas yr}^{-1}$ at the typical *W2* magnitude of our targets; Eisenhardt et al. 2019) suggests that such objects must be relatively nearby. For a moving source, nondetections in *W1* and all other shorter

wavelengths indicate an extremely cold temperature and low luminosity and hence a small distance. Moving objects detected solely in *W2* are thus prime close-by Y dwarf candidates, and they were considered the highest-priority target class for our *Spitzer* p14034 campaign.

2. Moving objects detected in *W1* but still potentially within 20 pc. In some cases, the presence of a faint *W1* counterpart indicated that a moving object was insufficiently red to plausibly be a Y dwarf. We nevertheless retained such objects for p14034 consideration if the photometric distance estimate implied by *W2* and *W1*–*W2* indicated that the object could potentially be a new member of the 20 pc sample. Completing the census of objects within this volume is crucial for space density and mass function analyses (Kirkpatrick et al. 2019a). Furthermore, *Spitzer* ch1/ch2 photometry can provide significantly refined photometric distance and spectral type estimates relative to those dependent upon low-significance *W1* detections. For these reasons, we deemed $d \lesssim 20$ pc candidates worthy p14034 *Spitzer* targets despite detection in *W1*.
3. Candidate very late type ($\gtrsim T0$) common proper-motion (CPM) companion objects potentially in wide-separation visual binary systems. Possible CPM status was usually noted serendipitously via our standard visual inspection motion-vetting process (Section 4.4) and subsequently checked using the similarity between the CatWISE motion of the candidate secondary and that of the putative primary. *Spitzer* ch1/ch2 observations for CPM candidates can provide a relatively accurate photometric distance and astrometry for an improved motion estimate. These can then be compared against the distance/motion of the primary to better test the comoving pair hypothesis. Late-type wide CPM companions are rare, so it is also highly valuable to obtain *Spitzer* ch1/ch2 photometric data points for these critical benchmarks. Presentation of late-type CatWISE CPM discoveries followed up via *Spitzer* p14034 in Marocco et al. (2020).
4. Objects with exceptionally large proper motion ($\mu \gtrsim 1''\ \text{yr}^{-1}$) and/or reduced proper motion¹⁹ ($H_{W2} \gtrsim 19.5$). Very high (reduced) proper motion of a source first recognized in the mid-infrared may be indicative of several interesting phenomena, including a late-type subdwarf, a very cold nearby neighbor to the Sun, and/or large tangential space velocity.

A given object can sometimes fall under more than one of the above target categories. But no moving-object discovery was placed on the p14034 program without meeting at least one of the above four selection criteria. All of our targets were, at the time of Astronomical Observation Request (AOR) submission to the p14034 program, never-before-published discoveries; our *Spitzer* campaign was not intended to provide supplementary follow-up of known objects drawn from the literature. Additionally, we vetoed candidates based on checking the *Spitzer* Heritage Archive (SHA) for existing unpublished observations by other teams targeting recent brown dwarf discoveries (e.g., Backyard Worlds; Kuchner et al. 2017) so as not to wastefully duplicate *Spitzer* pointings.

¹⁷ CatWISE can be queried via IRSA at <https://irsa.ipac.caltech.edu/applications/Gator/>.

¹⁸ The unWISE artifact flagging is described in detail in the Appendix of Meisner et al. (2019).

¹⁹ The *W2* reduced proper motion is defined as $H_{W2} = m_{W2} + 5 + 5\log_{10}(\mu)$, where μ is the total proper motion in units of arcsec yr^{-1} .

In our target selection decision-making, we sought to pursue a “high-risk, high-reward” strategy. We declined to place many of our unmistakable late-type moving-object discoveries on p14034 because secure *W1* detections made clear that they were simply T dwarfs at $\gtrsim 30$ pc. Instead of such “safe” objects, we opted to prioritize very faint *W2*-only candidates with Y dwarf potential, even those so marginal in *WISE* that they might ultimately turn out to be entirely spurious. The rationale is that mid-T dwarfs do not necessitate *Spitzer*’s unique capabilities in the same way that Y dwarfs do, so we ought to observe as many Y dwarfs as possible before *Spitzer*’s retirement, even at the expense of false positives. Similarly, to find the most superlative targets before *Spitzer*’s retirement, we chose not to limit ourselves to searches based strictly on CatWISE but instead leveraged additional data products at hand (the AllWISE Catalog and unWISE coadds; see Sections 4.2 and 4.3, respectively).

The following subsections provide a detailed list of our many (14) distinct searches that contributed at least one target to the p14034 photometry presented in Table 1. For convenience, we refer to each search by a shorthand that consists of one capital letter followed by one digit. Table 1 lists which specific search(es) discovered each target in the “search method” column. Our searches generally rely on motion selection, color selection of objects that are very red in *W1*–*W2*, or some combination of the two. Each search’s candidate identification yielded far more false positives than genuine newly discovered moving objects, so extensive visual inspection campaigns were performed to assess each candidate’s possible motion by eye (Section 4.4). The dominant sources of false positives are bright star artifacts, blends, and statistical measurement fluctuations that lead to the impression of potentially large motion and/or red *W1*–*W2* color.

4.1. CatWISE-based Selections

Most of our p14034 targets were discovered by directly mining the CatWISE Preliminary Catalog. We ran a total of 11 distinct moving-object searches on this catalog. Note that our searches were performed on early, unfinished versions of CatWISE, rather than the published CatWISE Preliminary Catalog described in Eisenhardt et al. (2019). In many cases, limited or no artifact flagging existed in these early CatWISE databases; this often shaped/constrained our tailoring of search criteria. Also, all CatWISE-based selections were run at a time when there was no distinction between sources now separated into the CatWISE “catalog” and “reject” tables.²⁰ Appendix A of Eisenhardt et al. (2019) provides column descriptions for the CatWISE quantities involved in our selection criteria.

Our 11 CatWISE-based searches fall under two broad categories: (1) traditional catalog queries, each implementing a set of hard cuts (Section 4.1.1), and (2) supervised machine-learning methods trained on human-verified late-type moving objects (Section 4.1.2).

4.1.1. CatWISE Catalog Cuts

Prior *WISE* motion surveys such as the AllWISE and AllWISE2 motion searches (Kirkpatrick et al. 2014, 2016) were performed via selections cutting on motion, color, and

artifact-flagging catalog columns. Motivated by the success of these previous *WISE*-based motion surveys, we modeled eight of our search methods after this same general approach but now applied to the newly available CatWISE data set.

Selection method C1 combines CatWISE color and motion information to isolate objects that are both red in *W1*–*W2* and have large *W2* reduced proper motion (H_{W2}). The usage of H_{W2} rather than simply proper motion itself is a way of prioritizing fast-moving objects of low luminosity, such as Y dwarfs and late-type subdwarfs. The C1 candidates are obtained from a full-sky CatWISE query requiring ($w2snr > 20$), ($w2snr_pm > 20$), ($H_{W2} > 15$), ($rchi2/rchi2_pm > 1.03$), ($w2rchi2_pm < 2$), ($W1-W2 \geq 1.5$), and ($Q < 10^{-5}$). Here Q is a significance-of-motion metric defined in Section 3.4.1 of Kirkpatrick et al. (2014) as $Q = e^{-\chi^2_{\text{motion}}/2}$, where $\chi^2_{\text{motion}} = (\text{pmra}/\text{sigpmra})^2 + (\text{pmdec}/\text{sigpmdec})^2$. Note that typical *WISE* sources such as main-sequence stars have a color of *W1*–*W2* ≈ 0 (Vega). The relatively high *W2* signal-to-noise ratio (S/N) requirements stipulated as part of this query were necessary to keep the candidate sample size manageable, as this search was performed at a time when no CatWISE artifact flagging was available.

Search C2 is a variant of search C1 replacing the ($W1-W2 \geq 1.5$) color cut with a proper-motion cut of $\mu > 0''.5 \text{ yr}^{-1}$. Again, search C2 was executed without the benefit of any artifact-flagging information.

Search C3 implements a combination of the cuts from C1 and C2 and was performed after artifact-flagging columns had been added to our working CatWISE database. By leveraging the artifact flagging to remove many spurious candidates, C3 extended to a lower *W2* S/N than C1/C2, specifically restricting to the range $10 < w2snr_pm \leq 20$. Also included in C3 was an additional requirement of ($w2snr_pm > w1snr_pm$). The significance of the motion criterion was made more stringent than in C1 and C2, requiring $Q < 10^{-6}$. Both the proper-motion cut $\mu > 0''.5 \text{ yr}^{-1}$ from C2 and the $H_{W2} > 15$ reduced proper-motion cut from C1/C2 were applied. Lastly, search C3 sought to eliminate artifacts by requiring ($ab_flags = "00"$).

Search C4 is a variant of C1 run after artifact flagging had been put in place. The CatWISE catalog cuts in C4 are the same as those in C1, aside from the following updates: C4 requires ($ab_flags = "00"$), flips the $rchi2/rchi2_pm$ cut to ($rchi2/rchi2_pm \leq 1.03$), and adds a new ($w1snr_pm = \text{null}$) *W1* nondetection requirement.

Although based on CatWISE catalog cuts, searches C5–C8 are not immediate descendants of the C1–C4 approaches. Search C5 consists of an all-sky CatWISE query requiring $Q < 10^{-5}$, ($w2mpro > 13$), ($w2snr > 10$), ($k1 = 0$), and ($k2 = 3$). Here $k1$ ($k2$) is a CatWISE column indicating, for each object, which scan direction(s) provided a successful photometric measurement in *W1* (*W2*); $k1 = 0$ means that neither ascending nor descending *WISE* scans provided good *W1* photometry, while $k2 = 3$ means that good *W2* photometry was obtained for both *WISE* scan directions. This query is thus, in effect, implementing an alternative means of identifying *W2*-only moving objects within the CatWISE catalog. Search C5 was also conducted prior to the existence of any CatWISE artifact-flagging capabilities.

Search C6 is a full-sky CatWISE query requiring ($w2snr > 10$), $w1flux < (w2flux \cdot 10^{-1.5/2.5} - 2 \cdot w1sigflux)$, ($rchi2/rchi2_pm > 1.03$), ($w2rchi2_pm < 2$), $Q < 10^{-6}$, and AllWISE CC flags = “0000” when available. The AllWISE CC flags were gathered via a CatWISE–AllWISE positional

²⁰ Only two of our p14034 targets are found in the CatWISE Preliminary reject table rather than in the main CatWISE Preliminary Catalog: CWISEPR J062436.84–071147.2 and CWISEPR J065144.62–115106.1.

Table 1
WISE and *Spitzer* Photometry

Name	Motion Confirmed	W1 (mag)	W2 (mag)	W1–W2 (mag)	AOR	ch1 (mag)	ch2 (mag)	ch1–ch2 (mag)	Search Method ^a
CWISEP J000006.01–704851.2	Yes	18.390 ± 0.153	15.834 ± 0.051	2.556 ± 0.161	68730112	17.293 ± 0.058	15.836 ± 0.022	1.457 ± 0.062	M2
CWISEP J000110.81–093215.5	Yes	18.598 ± 0.259	16.104 ± 0.086	2.494 ± 0.273	68727808	17.573 ± 0.065	15.889 ± 0.021	1.684 ± 0.068	M2
CWISEP J001146.07–471306.8	Yes	18.939 ± 0.272	15.986 ± 0.062	2.953 ± 0.279	68486656	17.744 ± 0.090	15.812 ± 0.021	1.931 ± 0.093	M1
CWISEP J003507.77–153233.8	Yes	17.351 ± 0.080 ^b	15.252 ± 0.039	2.099 ± 0.089	68235776	17.111 ± 0.065	15.228 ± 0.020	1.884 ± 0.068	C6
CWISEP J003915.43+360939.0	No	>19.043	16.303 ± 0.087	>2.740	68506112	18.191 ± 0.102	15.982 ± 0.021	2.210 ± 0.104	C8
CWISEP J004158.35+381811.9	Yes	18.654 ± 0.248	15.957 ± 0.065	2.697 ± 0.256	68486144	17.817 ± 0.095	16.069 ± 0.024	1.749 ± 0.098	M1
CWISEP J005802.63+723330.3	Yes	17.395 ± 0.072	16.109 ± 0.065	1.286 ± 0.097	68731904	17.500 ± 0.062	16.749 ± 0.034	0.751 ± 0.070	C3
CWISEP J010247.48–654226.4	No	19.416 ± 0.512	16.681 ± 0.099	2.735 ± 0.521	68509952	18.787 ± 0.159	16.432 ± 0.023	2.354 ± 0.160	C8
CWISEP J010527.69–783419.3	Yes	16.619 ± 0.035 ^b	14.996 ± 0.023	1.623 ± 0.042	68237568	17.289 ± 0.071	15.204 ± 0.019	2.085 ± 0.074	C1, C6
CWISEP J010650.61+225159.1	Yes	17.524 ± 0.103	15.045 ± 0.036	2.479 ± 0.109	68234752	16.490 ± 0.035	15.135 ± 0.020	1.354 ± 0.040	C1, C2, C6
CWISEP J012735.44–564110.5	No	17.996 ± 0.112	15.757 ± 0.048	2.239 ± 0.122	68495360	17.509 ± 0.072	15.726 ± 0.021	1.782 ± 0.075	M1
CWISEP J012748.35–631056.1	Yes	17.128 ± 0.057 ^b	15.507 ± 0.039	1.621 ± 0.069	68732672	16.872 ± 0.046	15.578 ± 0.022	1.294 ± 0.051	M1
CWISEP J014607.55–375705.6	Yes	18.166 ± 0.149	15.793 ± 0.057	2.373 ± 0.160	68497408	17.396 ± 0.062	15.680 ± 0.021	1.717 ± 0.066	M1
CWISEP J015613.24+325526.6	Yes	18.812 ± 0.416	16.063 ± 0.082	2.749 ± 0.424	68164096	17.564 ± 0.087	16.116 ± 0.030	1.448 ± 0.092	C3, C5, C6
CWISEP J020103.10+293801.8	Yes	18.049 ± 0.153	15.845 ± 0.067	2.204 ± 0.167	68504320	17.139 ± 0.052	15.963 ± 0.023	1.176 ± 0.057	C3, C6
CWISEP J020938.72+180427.7	Yes	18.461 ± 0.331	16.058 ± 0.086	2.403 ± 0.342	68500992	17.925 ± 0.089	16.141 ± 0.024	1.784 ± 0.092	M3
CWISEP J021243.55+053147.2	No	>19.118	15.931 ± 0.076	>3.187	68556032	18.931 ± 0.250	16.028 ± 0.024	2.903 ± 0.251	C8
CWISEP J021921.66–265451.8	Yes	17.755 ± 0.118	16.162 ± 0.081	1.593 ± 0.143	68730368	17.934 ± 0.093	17.029 ± 0.039	0.906 ± 0.101	C3
CWISEP J022122.41–564125.0	Yes	18.375 ± 0.138	15.825 ± 0.045	2.550 ± 0.145	68494848	17.389 ± 0.062	15.649 ± 0.021	1.740 ± 0.065	M1
CWISEP J022513.27+154854.8	No	18.653 ± 0.428	15.646 ± 0.063	3.007 ± 0.433	68725760	17.675 ± 0.099	15.818 ± 0.024	1.857 ± 0.102	M2
CWISEP J022631.82–203439.4	Yes	18.478 ± 0.216	16.208 ± 0.086	2.270 ± 0.232	68164352	17.602 ± 0.075	15.962 ± 0.025	1.640 ± 0.079	C3, C6
CWISEP J022935.43+724616.4 N	No	17.401 ± 0.077	15.240 ± 0.035	2.161 ± 0.085	26741760	17.423 ± 0.068	15.982 ± 0.045	1.441 ± 0.081	M2
CWISEP J022935.43+724616.4 S	No	17.401 ± 0.077	15.240 ± 0.035	2.161 ± 0.085	26741760	17.423 ± 0.068	15.819 ± 0.040	1.604 ± 0.078	M2
CWISEP J023842.60–133210.7	Yes	>19.118	16.192 ± 0.088	>2.926	68728576	19.058 ± 0.219	16.329 ± 0.024	2.729 ± 0.220	M2
CWISEP J024204.91–225604.6	Yes	>19.161	16.473 ± 0.112	>2.688	68557056	18.403 ± 0.113	16.431 ± 0.024	1.971 ± 0.115	C7
CWISEP J024710.25–145809.9	No	17.532 ± 0.099	16.197 ± 0.089	1.335 ± 0.133	68731392	17.463 ± 0.055	16.641 ± 0.028	0.822 ± 0.062	C3
CWISEP J024810.75–694127.9	No	>19.135	16.369 ± 0.065	>2.766	68726784	18.243 ± 0.110	16.352 ± 0.024	1.892 ± 0.113	M2
CWISEP J025747.92–205602.7	No	18.243 ± 0.163	15.625 ± 0.046	2.618 ± 0.169	68497152	16.992 ± 0.052	15.581 ± 0.022	1.411 ± 0.056	M1
CWISEP J031130.28+035931.8	Yes	18.768 ± 0.305	16.581 ± 0.123	2.187 ± 0.329	68507648	17.816 ± 0.071	17.040 ± 0.036	0.776 ± 0.079	M3
CWISEP J031557.05+203552.4	No	17.146 ± 0.079	15.530 ± 0.057	1.616 ± 0.097	68727296	17.091 ± 0.061	16.006 ± 0.027	1.086 ± 0.066	M2
CWISEP J031908.60+081120.4	No	17.465 ± 0.108	16.058 ± 0.086	1.407 ± 0.138	68498432	17.365 ± 0.064	17.026 ± 0.041	0.339 ± 0.076	M3
CWISEP J031935.50–041231.7	Yes	>18.625	16.420 ± 0.096	>2.205	68577280	18.844 ± 0.184	16.545 ± 0.026	2.298 ± 0.186	C7
CWISEP J032109.59+693204.5	Yes	>18.488	15.994 ± 0.061	>2.494	68498688	18.561 ± 0.188	15.928 ± 0.023	2.633 ± 0.190	M3
CWISEP J034336.27+184025.8	No	17.542 ± 0.110	15.984 ± 0.083	1.558 ± 0.138	68733952	17.374 ± 0.057	16.550 ± 0.030	0.824 ± 0.064	C3
CWISEP J034514.82+173528.1	No	18.222 ± 0.209	15.559 ± 0.050	2.663 ± 0.215	68728064	17.424 ± 0.076	15.450 ± 0.021	1.974 ± 0.079	M2
CWISEP J034755.11+123051.9	Yes	18.261 ± 0.216	15.273 ± 0.050	2.988 ± 0.222	68164608	16.763 ± 0.045	15.146 ± 0.020	1.617 ± 0.050	C1
CWISEP J034904.05–462827.9	Yes	18.929 ± 0.238	16.304 ± 0.070	2.625 ± 0.248	68487424	17.830 ± 0.083	16.305 ± 0.025	1.526 ± 0.086	M1
CWISEP J040106.67+085748.5	Yes	>18.629	15.855 ± 0.074	>2.774	68500736	17.596 ± 0.078	15.677 ± 0.023	1.918 ± 0.081	M3
CWISEP J040235.55–265145.4	Yes	18.030 ± 0.145	15.549 ± 0.047	2.481 ± 0.152	68727552	18.173 ± 0.150	15.453 ± 0.021	2.720 ± 0.152	M2
CWISEP J040324.67+185729.6	No	18.715 ± 0.446	16.150 ± 0.094	2.565 ± 0.456	68505856	17.856 ± 0.086	16.242 ± 0.027	1.615 ± 0.090	C8
CWISEP J040351.00–491605.6	Yes	18.001 ± 0.091	16.035 ± 0.050	1.966 ± 0.104	68487680	18.118 ± 0.130	16.127 ± 0.025	1.992 ± 0.132	M1
CWISEP J041025.10+033807.2	No	18.863 ± 0.466	16.264 ± 0.107	2.599 ± 0.478	68729856	17.794 ± 0.071	16.272 ± 0.024	1.522 ± 0.075	M1
CWISEP J042455.68+000221.4	No	>18.710	15.506 ± 0.050	>3.204	68728832	17.641 ± 0.090	15.432 ± 0.021	2.208 ± 0.093	C8
CWISEP J042404.54+665011.2	Yes	17.820 ± 0.104	15.639 ± 0.053	2.181 ± 0.117	68486912	17.409 ± 0.075	15.661 ± 0.023	1.748 ± 0.078	C6
CWISEP J043034.27+255653.7	Yes	17.086 ± 0.080 ^b	14.912 ± 0.035	2.174 ± 0.087	68556544	16.035 ± 0.025	14.788 ± 0.018	1.246 ± 0.031	M2
CWISEP J043309.31+100902.9	Yes	17.539 ± 0.101	15.094 ± 0.039	2.445 ± 0.108	68236544	16.927 ± 0.050	15.149 ± 0.020	1.778 ± 0.054	C1
CWISEP J044330.73+693828.3	No	17.608 ± 0.088	16.348 ± 0.083	1.260 ± 0.121	68728320	17.271 ± 0.046	16.583 ± 0.027	0.689 ± 0.054	C3

Table 1
(Continued)

Name	Motion Confirmed	W1 (mag)	W2 (mag)	W1–W2 (mag)	AOR	ch1 (mag)	ch2 (mag)	ch1–ch2 (mag)	Search Method ^a
CWISEP J044719.61+202158.1	Yes	17.363 ± 0.098	15.519 ± 0.061	1.844 ± 0.115	68726016	17.899 ± 0.122	15.743 ± 0.024	2.156 ± 0.124	C3
CWISEP J050521.29–591311.7	Yes	17.636 ± 0.059	16.129 ± 0.053	1.507 ± 0.079	68493056	17.541 ± 0.072	16.160 ± 0.025	1.381 ± 0.076	M1
CWISEP J052346.34–545314.7	Yes	19.055 ± 0.267	16.481 ± 0.072	2.574 ± 0.277	68499712	18.557 ± 0.144	16.185 ± 0.023	2.372 ± 0.146	C3, C6
CWISEP J053644.82–305539.3	No	18.926 ± 0.260	15.633 ± 0.046	3.293 ± 0.264	68508416	17.843 ± 0.114	15.518 ± 0.023	2.324 ± 0.116	M1
CWISEP J054233.06+793459.1	No	18.967 ± 0.261	16.119 ± 0.064	2.848 ± 0.269	68732928	17.699 ± 0.073	16.091 ± 0.023	1.608 ± 0.077	M2
CWISEP J055816.68–450233.6	No	18.573 ± 0.157	15.826 ± 0.049	2.747 ± 0.164	68492800	17.631 ± 0.078	15.861 ± 0.023	1.770 ± 0.081	M1
CWISEP J060132.96–592227.3 ^c	Yes	15.747 ± 0.020 ^b	14.468 ± 0.015	1.279 ± 0.025	M1
CWISEPR J062436.84–071147.2	Yes	17.614 ± 0.120	15.226 ± 0.037	2.388 ± 0.126	68491264	16.902 ± 0.054	15.308 ± 0.021	1.594 ± 0.058	A1, A2
CWISEP J062742.27–215908.1	Yes	18.654 ± 0.256	15.947 ± 0.069	2.707 ± 0.265	68504832	17.642 ± 0.087	15.929 ± 0.023	1.713 ± 0.090	C8
CWISEP J063257.49+274629.4	No	>18.109	15.648 ± 0.070	>2.461	68499200	17.629 ± 0.080	16.009 ± 0.026	1.620 ± 0.084	M3
CWISEP J063428.10+504925.9	Yes	19.068 ± 0.525	15.914 ± 0.069	3.154 ± 0.530	68495104	18.374 ± 0.154	15.955 ± 0.023	2.418 ± 0.155	C3, M1
CWISEP J063845.48–615937.2	Yes	18.891 ± 0.164	16.745 ± 0.074	2.146 ± 0.180	68488704	18.083 ± 0.094	16.614 ± 0.028	1.469 ± 0.098	M1
CWISEPR J065144.62–115106.1	Yes	18.388 ± 0.222	15.592 ± 0.056	2.796 ± 0.229	68493824	16.909 ± 0.049	15.398 ± 0.021	1.511 ± 0.054	M1
CWISEP J070055.19+783834.0	Yes	18.998 ± 0.287	16.595 ± 0.104	2.403 ± 0.305	68486400	17.918 ± 0.082	16.712 ± 0.029	1.207 ± 0.086	M1
CWISEP J070214.84–544041.7	Yes	19.252 ± 0.372	16.817 ± 0.095	2.435 ± 0.384	68496128	18.189 ± 0.104	16.541 ± 0.027	1.648 ± 0.107	M1
CWISEP J071626.02–371951.1	No	>18.378	16.176 ± 0.089	>2.202	68555776	17.360 ± 0.055	15.938 ± 0.022	1.422 ± 0.059	C8
CWISEP J071813.30–061421.1	Yes	>18.114	16.402 ± 0.124	>1.712	68508160	17.959 ± 0.078	17.077 ± 0.040	0.882 ± 0.087	C8
CWISEP J082400.43+075019.9	No	18.753 ± 0.387	16.380 ± 0.123	2.373 ± 0.406	68509184	18.016 ± 0.089	17.033 ± 0.041	0.983 ± 0.098	C8
CWISEP J084726.55+233558.1	No	17.745 ± 0.115	15.729 ± 0.070	2.016 ± 0.135	68488960	16.965 ± 0.053	15.660 ± 0.025	1.304 ± 0.058	M1
CWISEP J085348.15+112921.5	No	18.093 ± 0.181	15.443 ± 0.047	2.650 ± 0.187	68507904	16.693 ± 0.042	15.448 ± 0.022	1.245 ± 0.047	A1, M1
CWISEP J085820.46+500834.4	No	18.202 ± 0.170	16.084 ± 0.083	2.118 ± 0.189	68501504	17.500 ± 0.070	15.851 ± 0.023	1.649 ± 0.074	M3
CWISEP J085908.26+152527.1	Yes	17.692 ± 0.119	15.262 ± 0.042	2.430 ± 0.126	68238080	17.112 ± 0.060	15.229 ± 0.021	1.884 ± 0.063	C1, C6
CWISEP J085938.95+534908.7	Yes	>18.998	15.926 ± 0.069	>3.072	68556288	18.512 ± 0.171	15.998 ± 0.024	2.514 ± 0.173	C8
CWISEP J090547.50+700239.8	No	18.591 ± 0.226	15.939 ± 0.062	2.652 ± 0.234	68730880	17.848 ± 0.082	15.816 ± 0.021	2.031 ± 0.085	M2
CWISEP J090536.35+740009.1	Yes	18.247 ± 0.157	16.455 ± 0.093	1.792 ± 0.182	68489472	17.603 ± 0.061	16.407 ± 0.025	1.196 ± 0.066	M1
CWISEP J091558.51+254713.2	No	18.616 ± 0.347	15.943 ± 0.080	2.673 ± 0.356	68508672	17.684 ± 0.085	16.158 ± 0.028	1.526 ± 0.089	A1
CWISEP J093111.03+232502.1	Yes	17.897 ± 0.206	15.726 ± 0.064	2.171 ± 0.216	68492544	17.372 ± 0.076	15.703 ± 0.025	1.670 ± 0.079	C3, C6, M1
CWISEP J093236.66–180029.3	Yes	18.315 ± 0.271	15.915 ± 0.071	2.400 ± 0.280	68489216	17.711 ± 0.083	15.704 ± 0.021	2.007 ± 0.085	M1
CWISEP J093852.89+063440.6	Yes	17.961 ± 0.143	15.794 ± 0.064	2.167 ± 0.157	68494336	18.442 ± 0.164	15.962 ± 0.025	2.480 ± 0.166	C3, M1
CWISEP J094005.50+523359.2	Yes	>19.207	15.935 ± 0.064	>3.272	68503296	18.520 ± 0.174	15.754 ± 0.022	2.766 ± 0.175	C7, M3
CWISEP J094615.56+351434.3	Yes	18.044 ± 0.151	15.969 ± 0.077	2.075 ± 0.169	68493312	17.178 ± 0.053	16.076 ± 0.026	1.101 ± 0.059	C3, C6, M1
CWISEP J094742.83+384619.3	No	>18.486	16.217 ± 0.093	>2.269	68498176	18.191 ± 0.112	16.055 ± 0.025	2.136 ± 0.115	M3
CWISEP J094930.41+663937.2	Yes	>19.197	16.206 ± 0.074	>2.991	68729600	18.373 ± 0.118	16.097 ± 0.021	2.276 ± 0.120	M2
CWISEP J094957.15–422017.1	No	18.264 ± 0.173	16.302 ± 0.080	1.962 ± 0.191	68733184	18.213 ± 0.111	17.506 ± 0.056	0.707 ± 0.124	C3
CWISEP J095930.71–401046.8	Yes	>18.743	16.834 ± 0.139	>1.909	68577536	18.235 ± 0.102	17.734 ± 0.059	0.501 ± 0.118	C7
CWISEP J100629.01+105408.5	Yes	17.864 ± 0.136	15.487 ± 0.056	2.377 ± 0.147	68495616	17.615 ± 0.090	15.558 ± 0.022	2.057 ± 0.093	M1
CWISEP J100854.84+203136.6	No	>18.863	15.614 ± 0.060	>3.249	68732160	17.930 ± 0.126	15.696 ± 0.024	2.234 ± 0.128	M2
CWISEP J101841.86+513108.8	No	17.595 ± 0.091	16.185 ± 0.080	1.410 ± 0.121	68727040	17.234 ± 0.048	16.434 ± 0.027	0.800 ± 0.055	C3
CWISEP J102201.27+145520.2	Yes	>18.541	15.772 ± 0.072	>2.769	68503552	17.770 ± 0.087	15.831 ± 0.025	1.939 ± 0.090	M3
CWISEP J103453.14+161228.0	Yes	17.721 ± 0.126	14.899 ± 0.035	2.822 ± 0.131	68499456	16.589 ± 0.038	14.879 ± 0.019	1.710 ± 0.043	C1, C6
CWISEP J103607.94–304253.1	No	>18.846	16.279 ± 0.098	>2.567	68510208	17.674 ± 0.072	16.738 ± 0.034	0.935 ± 0.080	C8
CWISEP J104104.20+221613.6	Yes	>18.742	16.249 ± 0.102	>2.493	68509696	18.924 ± 0.199	16.650 ± 0.029	2.274 ± 0.201	C8
CWISEP J104446.56+001754.9	Yes	18.862 ± 0.519	16.160 ± 0.095	2.702 ± 0.528	68502528	18.076 ± 0.106	15.993 ± 0.023	2.083 ± 0.109	C8
CWISEP J104756.81+545741.6	Yes	>19.355	16.339 ± 0.095	>3.016	68500480	18.731 ± 0.166	16.257 ± 0.024	2.474 ± 0.168	C8
CWISEP J110021.08+094652.9	Yes	18.241 ± 0.192	15.514 ± 0.058	2.727 ± 0.201	68493568	17.481 ± 0.082	15.623 ± 0.025	1.858 ± 0.086	C6, M1
CWISEP J111055.12–174738.2	Yes	17.270 ± 0.082	15.010 ± 0.035	2.260 ± 0.089	68238592	16.615 ± 0.038	15.038 ± 0.019	1.576 ± 0.042	C1, C6
CWISEP J113010.21+313947.3	Yes	17.573 ± 0.092	15.371 ± 0.053	2.202 ± 0.106	68487936	16.556 ± 0.038	15.299 ± 0.020	1.257 ± 0.043	C6

Table 1
(Continued)

Name	Motion Confirmed	W1 (mag)	W2 (mag)	W1–W2 (mag)	AOR	ch1 (mag)	ch2 (mag)	ch1–ch2 (mag)	Search Method ^a
CWISEP J120444.33–235926.8	Yes	18.103 ± 0.175	15.273 ± 0.042	2.830 ± 0.180	68236800	16.907 ± 0.050	15.299 ± 0.021	1.608 ± 0.055	C1, C2, C6
CWISEP J121358.13+294237.0	No	18.715 ± 0.247	16.004 ± 0.076	2.711 ± 0.258	68505344	17.855 ± 0.084	16.010 ± 0.023	1.844 ± 0.087	M1
CWISEP J122010.03+281431.3	Yes	18.004 ± 0.128	15.767 ± 0.057	2.237 ± 0.140	68494080	17.422 ± 0.067	15.861 ± 0.023	1.561 ± 0.071	C3, M1
CWISEP J124138.41–820051.9	Yes	17.385 ± 0.061 ^b	15.163 ± 0.026	2.222 ± 0.066	68238848	17.367 ± 0.075	15.337 ± 0.021	2.030 ± 0.077	C1, C6
CWISEP J130255.54+191145.9	Yes	18.396 ± 0.188	15.607 ± 0.057	2.789 ± 0.196	68489984	17.381 ± 0.073	15.563 ± 0.023	1.818 ± 0.077	M1
CWISEP J131252.97+341746.5	Yes	>19.202	16.230 ± 0.077	>2.972	68510464	18.096 ± 0.104	16.392 ± 0.027	1.704 ± 0.108	C8
CWISEP J131208.16–105231.8	No	18.350 ± 0.205	16.071 ± 0.080	2.279 ± 0.220	68492032	18.227 ± 0.135	16.175 ± 0.028	2.052 ± 0.138	C3, M1
CWISEP J131221.97–310845.7	Yes	17.801 ± 0.188	15.766 ± 0.058	2.035 ± 0.197	68494592	17.691 ± 0.082	15.809 ± 0.023	1.882 ± 0.086	C3, C6, M1
CWISEP J131350.91–440352.2	Yes	18.620 ± 0.223	15.870 ± 0.066	2.750 ± 0.233	68490752	17.243 ± 0.054	15.599 ± 0.021	1.644 ± 0.058	M1
CWISEP J134143.75+574112.9	No	17.954 ± 0.105	15.456 ± 0.039	2.498 ± 0.112	68504576	17.241 ± 0.066	15.522 ± 0.021	1.719 ± 0.069	C4, M3
CWISEP J135336.29–003756.6 ^c	Yes	18.243 ± 0.174 ^b	15.495 ± 0.049	2.748 ± 0.181	C6
CWISEP J135937.65–435226.9	Yes	>18.374	16.132 ± 0.083	>2.242	68509440	18.379 ± 0.135	15.945 ± 0.023	2.434 ± 0.137	C8
CWISEP J140118.30+432554.2	Yes	17.614 ± 0.081	15.540 ± 0.041	2.074 ± 0.091	68235008	16.989 ± 0.052	15.641 ± 0.023	1.348 ± 0.057	C1, C2
CWISEP J140247.83+102132.6	Yes	15.717 ± 0.027	14.493 ± 0.024	1.224 ± 0.036	68487168	15.214 ± 0.016	14.436 ± 0.018	0.778 ± 0.024	M1
CWISEP J141206.85+234412.4	Yes	18.545 ± 0.196	16.239 ± 0.082	2.306 ± 0.212	68491776	17.452 ± 0.060	16.218 ± 0.025	1.234 ± 0.065	M1
CWISEP J141400.68+163153.9	No	17.390 ± 0.080 ^b	15.824 ± 0.058	1.566 ± 0.099	68729088	17.431 ± 0.065	16.360 ± 0.030	1.071 ± 0.072	C3
CWISEP J142552.36+485151.3	No	18.013 ± 0.110	16.410 ± 0.078	1.603 ± 0.135	68726528	17.948 ± 0.078	17.055 ± 0.035	0.892 ± 0.085	M2
CWISEP J143439.23–134421.4	Yes	>18.763	16.158 ± 0.101	>2.605	68500224	18.271 ± 0.130	16.150 ± 0.026	2.121 ± 0.133	M1
CWISEP J144606.62–231717.8	Yes	18.281 ± 0.292	15.998 ± 0.094	2.283 ± 0.307	68496896	19.511 ± 0.434	15.802 ± 0.024	3.709 ± 0.435	M1
CWISEP J145837.91+173450.1	Yes	16.677 ± 0.045	15.118 ± 0.033	1.559 ± 0.056	68726272	17.114 ± 0.059	15.281 ± 0.021	1.833 ± 0.063	C4
CWISEP J150252.82–304232.8	Yes	17.465 ± 0.093	15.071 ± 0.037	2.394 ± 0.100	68237056	16.577 ± 0.038	15.029 ± 0.019	1.548 ± 0.042	C1
CWISEP J151140.51–835918.0	No	19.057 ± 0.383	16.566 ± 0.091	2.491 ± 0.394	68507136	17.662 ± 0.057	16.581 ± 0.026	1.081 ± 0.063	C8
CWISEP J151521.22–215736.9 ^c	Yes	16.580 ± 0.050 ^b	14.951 ± 0.033	1.629 ± 0.060	C4, M1
WISEA J153429.75–104303.3	Yes	18.264 ± 0.372	16.072 ± 0.202	2.192 ± 0.423	68555520	16.691 ± 0.032	15.766 ± 0.023	0.926 ± 0.039	U1
CWISEP J153859.39+482659.1	Yes	17.797 ± 0.087	15.770 ± 0.046	2.027 ± 0.098	68238336	18.082 ± 0.140	15.809 ± 0.024	2.272 ± 0.142	C1
CWISEP J154151.59+523025.0 N	No	17.797 ± 0.080 ^b	15.703 ± 0.039	2.094 ± 0.089	68497920	18.205 ± 0.142	16.387 ± 0.030	1.818 ± 0.146	M3
CWISEP J154151.59+523025.0 S	No	17.797 ± 0.080 ^b	15.703 ± 0.039	2.094 ± 0.089	68497920	18.401 ± 0.154	16.566 ± 0.032	1.836 ± 0.157	M3
CWISEP J160311.60–104620.4	Yes	18.293 ± 0.216	15.675 ± 0.066	2.618 ± 0.226	68492288	17.326 ± 0.076	15.575 ± 0.023	1.752 ± 0.079	C3, M1
CWISEP J160835.01–244244.7	Yes	17.251 ± 0.096	15.133 ± 0.045	2.118 ± 0.106	68239104	16.621 ± 0.040	15.116 ± 0.019	1.504 ± 0.044	C1
CWISEP J161822.86–062310.2	Yes	17.886 ± 0.143	15.824 ± 0.063	2.062 ± 0.156	68499968	17.611 ± 0.079	15.660 ± 0.021	1.951 ± 0.082	M3
CWISEP J162225.92+370118.8	Yes	18.896 ± 0.239	16.053 ± 0.057	2.843 ± 0.246	68496384	17.522 ± 0.072	16.214 ± 0.026	1.308 ± 0.076	C3, C6
CWISEP J163200.11+002108.6	No	>18.625	16.354 ± 0.100	>2.271	68507392	18.461 ± 0.120	16.870 ± 0.032	1.591 ± 0.124	C8
CWISEP J165215.62+022918.5	Yes	17.771 ± 0.123	16.384 ± 0.104	1.387 ± 0.161	68506368	17.677 ± 0.065	16.953 ± 0.035	0.723 ± 0.074	M3
CWISEP J165359.67+214457.2	No	>18.723	16.256 ± 0.076	>2.467	68557312	18.047 ± 0.090	16.136 ± 0.023	1.911 ± 0.093	M2
CWISEP J170918.83+000950.5	No	>18.918	15.846 ± 0.058	>3.072	68729344	17.523 ± 0.073	15.747 ± 0.023	1.776 ± 0.077	M2
CWISEP J172104.42+595047.7	No	17.808 ± 0.058	16.081 ± 0.049	1.727 ± 0.076	3862272	17.545 ± 0.057	15.535 ± 0.030	2.009 ± 0.065	C6
CWISEP J175746.31+195112.6	No	17.873 ± 0.182	16.260 ± 0.084	1.613 ± 0.200	68502272	18.627 ± 0.149	16.381 ± 0.024	2.246 ± 0.151	C3, C5
CWISEP J182358.73–740246.0	Yes	16.722 ± 0.048	15.569 ± 0.051	1.153 ± 0.070	68233216	16.770 ± 0.047	15.566 ± 0.022	1.203 ± 0.052	C2
CWISEP J185658.80+601351.4	Yes	17.506 ± 0.059	15.734 ± 0.036	1.772 ± 0.069	68730624	16.814 ± 0.045	15.618 ± 0.022	1.196 ± 0.050	C4
CWISEP J193518.58–154620.3	Yes	18.534 ± 0.396	15.852 ± 0.079	2.682 ± 0.404	69998848	18.512 ± 0.030	15.528 ± 0.017	2.984 ± 0.034	M1
WISENF J193656.08+040801.2	Yes	>16.551	14.671 ± 0.222	>1.880	68576768	17.096 ± 0.061	14.689 ± 0.018	2.407 ± 0.064	U1
CWISEP J194027.48–345650.6	No	18.739 ± 0.432	16.440 ± 0.129	2.299 ± 0.451	68504064	17.347 ± 0.053	16.708 ± 0.030	0.639 ± 0.061	C8
CWISEP J194101.59+542335.9	Yes	17.297 ± 0.047	15.417 ± 0.029	1.880 ± 0.055	68498944	17.010 ± 0.054	15.507 ± 0.021	1.504 ± 0.057	C4, M1
CWISEP J194812.42–322334.9	Yes	17.669 ± 0.173 ^b	15.879 ± 0.082	1.790 ± 0.191	68503808	16.856 ± 0.041	15.827 ± 0.023	1.028 ± 0.046	C6
CWISEP J201146.45–481259.7	Yes	17.215 ± 0.081	15.379 ± 0.047	1.836 ± 0.094	68239360	17.814 ± 0.116	15.318 ± 0.021	2.496 ± 0.118	C1, C6
CWISEP J201510.68–675005.6	Yes	17.121 ± 0.072	15.014 ± 0.038	2.107 ± 0.081	68501248	15.918 ± 0.023	14.665 ± 0.018	1.254 ± 0.029	C1
CWISEP J203821.53–064930.9	Yes	18.804 ± 0.464	16.004 ± 0.080	2.800 ± 0.471	68556800	17.882 ± 0.087	15.619 ± 0.020	2.263 ± 0.089	C8

Table 1
(Continued)

Name	Motion Confirmed	W1 (mag)	W2 (mag)	W1–W2 (mag)	AOR	ch1 (mag)	ch2 (mag)	ch1–ch2 (mag)	Search Method ^a
CWISEP J205019.99–253652.8	Yes	17.348 ± 0.103	15.080 ± 0.040	2.268 ± 0.110	68233984	16.622 ± 0.040	15.079 ± 0.019	1.543 ± 0.044	C1, C2, C6
CWISEP J205908.95+024105.6	Yes	17.273 ± 0.079 ^b	15.620 ± 0.055	1.653 ± 0.096	68731136	17.163 ± 0.062	15.525 ± 0.022	1.638 ± 0.066	U1
CWISEP J210007.87–293139.8	Yes	>18.848	15.960 ± 0.078	>2.888	68503040	18.351 ± 0.161	15.959 ± 0.023	2.392 ± 0.163	M3
CWISEP J211909.29–192117.4	No	18.279 ± 0.319	15.907 ± 0.078	2.372 ± 0.328	68490240	17.606 ± 0.076	15.771 ± 0.021	1.836 ± 0.079	M1
CWISEP J212828.05+352912.4	Yes	18.240 ± 0.157	16.242 ± 0.079	1.998 ± 0.176	68236032	18.111 ± 0.118	17.059 ± 0.043	1.052 ± 0.125	C6
CWISEP J213249.05+690113.7	Yes	17.888 ± 0.094	15.179 ± 0.027	2.709 ± 0.098	68234496	17.244 ± 0.069	15.271 ± 0.021	1.974 ± 0.072	C1
CWISEP J213838.74–313808.5	Yes	18.000 ± 0.157	15.144 ± 0.042	2.856 ± 0.163	68234240	16.917 ± 0.052	15.136 ± 0.019	1.781 ± 0.055	C1, C2, C6
CWISEP J213930.45+042721.6	Yes	18.432 ± 0.295	15.804 ± 0.069	2.628 ± 0.303	68497664	17.915 ± 0.101	15.747 ± 0.022	2.168 ± 0.103	M1
CWISEP J215841.50+732842.7	Yes	17.007 ± 0.058	14.926 ± 0.029	2.081 ± 0.065	68502016	16.927 ± 0.052	15.160 ± 0.020	1.767 ± 0.055	M3
CWISEP J220452.02+063343.4	No	18.422 ± 0.338	15.976 ± 0.080	2.446 ± 0.347	68731648	17.856 ± 0.094	16.011 ± 0.025	1.845 ± 0.098	M2
CWISEP J221736.94–222647.6	No	17.820 ± 0.120	15.842 ± 0.069	1.978 ± 0.138	68235520	17.741 ± 0.103	15.968 ± 0.026	1.773 ± 0.106	C3, C6
CWISEP J222035.35–810322.6	Yes	18.448 ± 0.161	15.953 ± 0.058	2.495 ± 0.171	68233728	17.382 ± 0.075	16.003 ± 0.025	1.378 ± 0.079	C6
CWISEP J223022.60+254907.5	Yes	18.344 ± 0.205	16.094 ± 0.076	2.250 ± 0.219	68491008	19.119 ± 0.292	16.290 ± 0.026	2.830 ± 0.293	M1
CWISEP J223138.55–383057.2	Yes	>18.673	16.170 ± 0.087	>2.503	68506624	18.015 ± 0.095	16.098 ± 0.023	1.917 ± 0.098	C8
CWISEP J224747.42–004103.6	No	17.180 ± 0.079	15.728 ± 0.067	1.452 ± 0.104	46949376	17.010 ± 0.086	15.947 ± 0.036	1.063 ± 0.093	C3
CWISEP J224916.17+371551.4	Yes	18.718 ± 0.252	16.481 ± 0.104	2.237 ± 0.273	68505088	18.526 ± 0.138	16.201 ± 0.023	2.324 ± 0.140	C8
CWISEP J225059.28–432057.2	Yes	18.651 ± 0.232	16.322 ± 0.089	2.329 ± 0.248	68164864	18.032 ± 0.099	16.145 ± 0.023	1.887 ± 0.102	C6
CWISEP J225156.13+392408.4	Yes	18.030 ± 0.131	15.719 ± 0.052	2.311 ± 0.141	68237824	17.291 ± 0.067	15.620 ± 0.023	1.672 ± 0.070	C1
CWISEP J225109.50–074037.7	Yes	17.737 ± 0.123	15.202 ± 0.047	2.535 ± 0.132	68233472	16.869 ± 0.053	15.100 ± 0.019	1.769 ± 0.056	C1, C2, C6
CWISEP J225511.56–191516.3	No	18.278 ± 0.199	16.623 ± 0.141	1.655 ± 0.244	68508928	18.933 ± 0.181	18.010 ± 0.073	0.923 ± 0.195	C8
CWISEP J225628.97+400227.3	Yes	18.370 ± 0.183	15.928 ± 0.065	2.442 ± 0.194	68489728	18.820 ± 0.226	15.806 ± 0.021	3.014 ± 0.227	C3, M1
CWISEP J230158.30–645858.3	Yes	18.401 ± 0.166	15.264 ± 0.034	3.137 ± 0.169	68235264	17.273 ± 0.057	15.364 ± 0.019	1.909 ± 0.060	A2
CWISEP J231047.80+362004.6	No	18.126 ± 0.153	16.237 ± 0.082	1.889 ± 0.174	68732416	17.683 ± 0.066	16.473 ± 0.025	1.209 ± 0.070	M2
CWISEP J231114.50+135148.5	No	18.606 ± 0.343	15.996 ± 0.079	2.610 ± 0.352	68733440	17.382 ± 0.061	15.868 ± 0.023	1.513 ± 0.065	M2
CWISEP J233216.39–290025.0	Yes	18.528 ± 0.253	15.921 ± 0.078	2.607 ± 0.265	68496640	16.740 ± 0.036	15.601 ± 0.021	1.140 ± 0.042	M1
CWISEP J235130.42–185800.2	Yes	17.410 ± 0.092	15.432 ± 0.048	1.978 ± 0.104	68236288	17.618 ± 0.094	15.590 ± 0.022	2.028 ± 0.097	C1, C6
CWISEP J235547.99+380438.9	Yes	>18.395	15.976 ± 0.067	>2.419	68163840	18.444 ± 0.259	15.926 ± 0.026	2.518 ± 0.261	C3, C5, C6
CWISEP J235644.78–481456.3	Yes	18.910 ± 0.286	16.165 ± 0.078	2.745 ± 0.296	68165120	18.727 ± 0.218	16.040 ± 0.024	2.687 ± 0.220	C3, C6

Notes.

^a The search method names listed in this column are defined in Sections 4.1–4.3, which also contain explanations of each search’s moving-object candidate selection procedure.

^b *WISE* photometry may be contaminated by blending.

^c Object is scheduled for p14034 *Spitzer* observations in the near future but does not yet have *Spitzer* photometry available.

(This table is available in machine-readable form.)

cross-match. One notable aspect of this search is that a color cut of effectively ($W1-W2 > 1.5$) is implemented in terms of fluxes rather than magnitudes to avoid the complications associated with, e.g., quoting magnitudes in cases of zero or negative $W1$ flux (as can happen for a very red $W1$ nondetection). In the CatWISE catalog, both $w1flux$ and $w2flux$ have units of Vega nanomaggies.²¹

Search C7 is a variant of search C6 that lowers the $W2$ S/N threshold to ($w2snr > 5$) in an attempt to push fainter. To balance out the large influx of sources at relatively low S/N, the color criterion was made more stringent at effectively ($W1-W2 > 2.5$), with the actual flux-based cut being $w1flux < (0.1 \cdot w2flux - 2 \cdot w1sigflux)$. The significance-of-motion criterion was loosened to ($Q < 10^{-5}$) for search C7. We additionally required that AllWISE CC flags not contain a capital letter (when an AllWISE cross-match was available) and ($ab_flags = "00"$).

Search C8 is a pure color selection. We required that candidates not be significantly detected at $W1$ ($w1snr < 3$) and be well detected in $W2$ ($w2snr > 10$) in CatWISE. A negative cross-match ($2''.5$ radius) against AllWISE sources with ($w3mpro < 13$) was used to remove extragalactic contaminants that tend to be red in $W2-W3$ color. Search C8 made use of CatWISE ab_flags to require that candidates not be flagged as $W2$ ghosts, $W2$ latents, or $W2$ diffraction spikes.

4.1.2. CatWISE Machine Learning

Search method M1 is described fully in Section 3 of Marocco et al. (2019). In brief, M1 uses the *XGBoost* software package (Chen & Guestrin 2016) to perform supervised machine learning on the CatWISE catalog. A training set was constructed from the CatWISE sources corresponding to known high proper motion late-T and Y dwarfs, with the goal of finding other CatWISE entries displaying similar properties. Search M1 is restricted to CatWISE objects that are faint and red by only classifying the subset of CatWISE rows with ($w2mpro > 14$) and also satisfying

$$(w1mpro - (3 \times w1sigmpro)) - (w2mpro + (3 \times w2sigmpro)) \geq 1.0. \quad (1)$$

This enforces a requirement that each retained source would have a color of ($W1-W2 \geq 1$) even if the CatWISE-reported magnitudes turned out to be 3σ bright in $W2$ and 3σ faint in $W1$.

Search M2 is a variant of search M1, with the classifier trained on a sample including hitherto identified p14034 targets rather than a sample consisting exclusively of previously published late-type brown dwarfs.

Search M3 is also a modified version of search M1 but removing the $W1-W2$ color criterion in Equation (1). The motivation for this variant is the possibility of recovering overlooked late-type moving objects with *WISE* color measurements corrupted due to blending with background sources, plus the potential to find additional fast-moving sources irrespective of $W1-W2$ color.

²¹ A source with a total flux of 1 Vega nanomaggie has a magnitude of 22.5 in the Vega system.

4.2. AllWISE-based Selections

From our prior experiences searching the AllWISE database, we considered it likely that more late-T and Y dwarfs remained to be found in that data set, particularly with the aid of our recently upgraded suite of visualization tools used to scrutinize candidates (Section 4.4). Two AllWISE-based moving-object searches contributed to the p14034 target list, both utilizing only simple catalog cuts.

In search A1, our candidates are drawn from a full-sky query of the AllWISE catalog, requiring very red $W1-W2$ color ($w1mpro-w2mpro > 3$), relatively little $W3$ flux ($w2mpro-w3mpro < 3.5$) to weed out extragalactic contaminants, $w2sigmpro$ not null, and $W2$ CC flags not containing H, O, P, or D to avoid bright star artifacts. Because of the very extreme $W1-W2$ color cut imposed, this yielded a relatively small sample of candidates, ~ 500 in total, which were then subjected to visual inspection.

Search A2 likewise identifies candidates using a pure color selection method based on the AllWISE catalog. We retain only those AllWISE rows that are effectively $W1$ nondetections ($w1snr < 3$) and have very red $W1-W2$ colors ($w1mpro-w2mpro > 2$), ($|b_{gal}| > 10^\circ$) to avoid the crowded Galactic plane, ($nb = 1$) to remove blends, and no H, O, P, or D in either the $W1$ or $W2$ CC flags to discard bright star artifacts. This yielded a sample of ~ 2000 candidates spread across the entire $|b_{gal}| > 10^\circ$ sky.

4.3. unWISE-based Selection

One of our selection techniques (search U1) proceeded directly from image-level analysis of the unWISE coadds themselves, rather than the CatWISE or AllWISE catalog. From the time-resolved unWISE coadds (Meisner et al. 2018c), we created two full-sky sets of meta-coadds in each band: one built by stacking together all prehibernation epochs, and a second built by stacking together all postreactivation epochs. We subtracted the prehibernation $W2$ meta-coadds from the postreactivation $W2$ meta-coadds and ran SExtractor (Bertin & Arnouts 1996) on the difference images. The goal was to find sources that moved sufficiently during the ~ 3 yr *WISE* hibernation period so as to avoid self-subtraction. SExtractor forced photometry on each of our four sets of meta-coadds ($W1$ and $W2$, pre- and posthibernation) was performed at the positions of $W2$ postreactivation difference image detections.

The catalog of $W2$ difference detections, augmented with forced photometry, was then analyzed to select moving-object candidates. Specifically, we cross-matched the difference-detection catalog with a sample of known late-type brown dwarfs to form a training set. An *XGBoost* classifier similar to those described in Section 4.1.2 was then used to identify difference-detection catalog entries with properties similar to those of the training sample.

Search U1 was employed because we expected it to perform well for very fast-moving sources ($\mu_{tot} \gtrsim 2'' \text{ yr}^{-1}$), whereas CatWISE source detection might reasonably fail for extremely faint objects with exceptionally large proper motions. The fact that both of our discoveries presented in this work that lack CatWISE counterparts—WISEA J153429.75-104303.3 ($\mu_{tot} \approx 2''.7 \text{ yr}^{-1}$) and WISENF J193656.08+040801.2 ($\mu_{tot} \approx 1''.3 \text{ yr}^{-1}$)—were identified via search U1 attests to the capability of this method to find moving objects that the CatWISE pipeline was not optimized to handle properly.

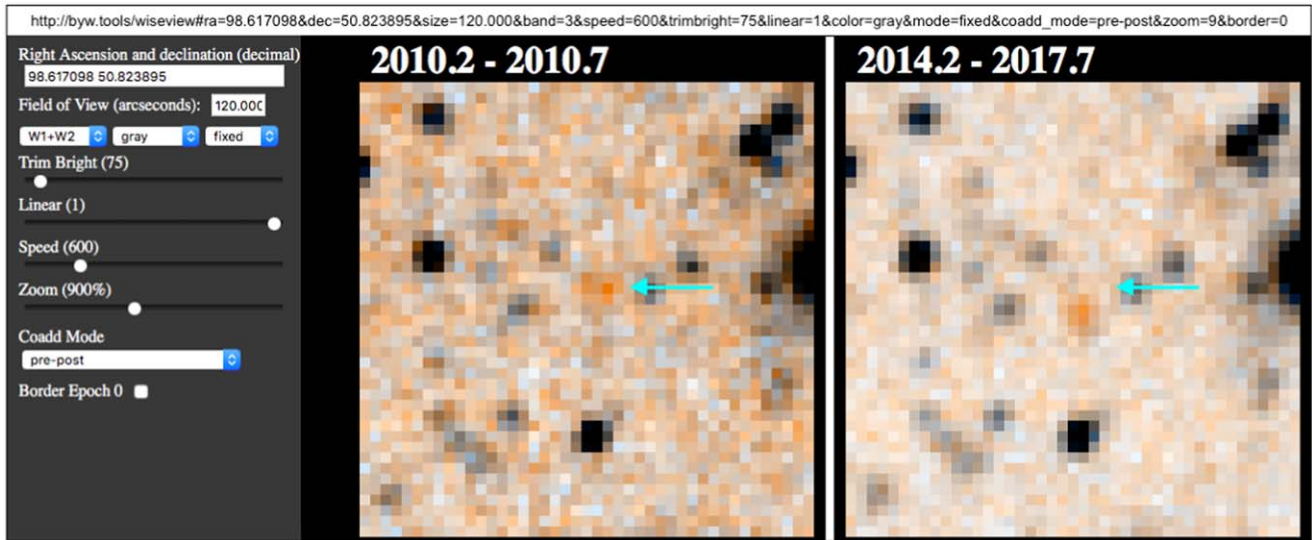


Figure 1. Depiction of the WiseView interactive image blinking tool (Section 4.4.2) used for visual inspection of potential p14034 targets. At left of the vertical white space is a screen shot of the WiseView interface, including blink tuning widgets and the first of two color composite images created based on the user-specified blink parameters. This blink sequence is centered on CWISEP J063428.10+504925.9, the orange source indicated by the cyan arrow. The cyan arrow remains at the same sky position in both panels; it is not present in WiseView but has been edited in to highlight the large southeasterly motion of this object. The “pre-post” coadd mode selected generates two meta-coadds per band, with the first spanning the full prehibernation time period (2010.2–2010.7 in this case) and the second spanning the available postreactivation time period (2014.2–2017.7 in this case). A screenshot of the postreactivation WiseView color composite is included at right of the vertical white space, with the WiseView widget panel omitted. Although these two images are shown side-by-side here, WiseView presents a single animated blink alternating between these two images, with both images aligned in the same position on the screen. The parameters of this blink are encoded in a WiseView URL provided at the top; one can experience this WiseView animation in action by visiting that URL.

4.4. Visualization Tools

Extensive visual inspection of moving-object candidates delivered by the searches described in Sections 4.1–4.3 played a vital role in providing a high-purity sample of brown dwarf targets for our *Spitzer* p14034 campaign. In total, we visually inspected $\sim 130,000$ candidates in the course of the searches described in Sections 4.1–4.3. A major factor enabling our discoveries based on CatWISE, AllWISE, and unWISE was our usage of visualization tools/aids that leveraged the full $W1/W2$ time baseline afforded by the combination of prehibernation and postreactivation *WISE*/NEOWISE imaging.

4.4.1. Finder Charts

We created a new, customized version of the multipanel, multiwavelength finder chart program used by prior *WISE* motion searches such as Kirkpatrick et al. (2016) and Kirkpatrick et al. (2016); for an example, see Figure 1 of Schneider et al. (2016). We added two sets of $W1/W2$ time-resolved unWISE coadd cutouts for each candidate, with one set at the beginning of the prehibernation *WISE* mission and one at the end of the third year of the postreactivation NEOWISE mission. Taking advantage of the ~ 6.5 yr *WISE*–NEOWISE time baseline in this way allowed us to perceive the source motion (or lack thereof) using only $W1/W2$ data at widely spaced epochs, rather than needing to obtain an appreciable time baseline by comparison of *WISE* images to shorter-wavelength data sets.

4.4.2. WiseView Interactive Blinker

Our visual inspection workflow relied heavily on a new visualization tool called WiseView (Caselden et al. 2018) not previously available for *WISE* moving-object searches such as the AllWISE and AllWISE2 motion surveys. In contrast to

static multiwavelength finder charts, WiseView is an interactive browser-based interface for creating customized animated blinks of time-resolved unWISE coadds. Numerous blink parameters are tunable in real time, including the band(s) shown ($W1$, $W2$, or both), central sky position, frame rate, stretch, and field-of-view size. Figure 1 illustrates an example of the WiseView interface as employed when vetting one of our $W2$ -only brown dwarf discoveries.

4.4.3. DESI Imaging Viewer

To select moving objects detected in $W2$ but not at any shorter wavelengths, we made extensive use of the DESI pre-imaging “Legacy Surveys” sky viewer²² to inspect red-optical survey images. This viewer allows for interactive exploration of wide-area survey data sets with deep z - and Y -band imaging, in particular DECaLS/MzLS ($z \approx 23.0$ AB at 5σ over $\sim 1/3$ of the sky; Dey et al. 2019) and Dark Energy Survey DR1 ($z \approx 23.4$ AB and $Y \approx 22.2$ AB at 5σ over $\sim 1/8$ of the sky; Abbott et al. 2018). Visible z and/or Y counterparts were generally treated as evidence that a moving-object candidate was either insufficiently red to be a Y dwarf or else extragalactic if the red-optical counterpart appeared extended.

4.4.4. IRSA Finder Chart

In some cases where conclusively confirming/denying motion by eye proved difficult, we consulted AllWISE $W3$ and $W4$ images via the IRSA Finder Chart application.²³ Because our motion candidates are so faint (median $W2 \sim 15.9$; see Section 5), a strong counterpart at $W3$ and/or $W4$ would only be expected in the case of a stationary extragalactic source, not for a late-type brown dwarf. We

²² <http://legacysurvey.org/viewer>

²³ <https://irsa.ipac.caltech.edu/applications/finderchart/>

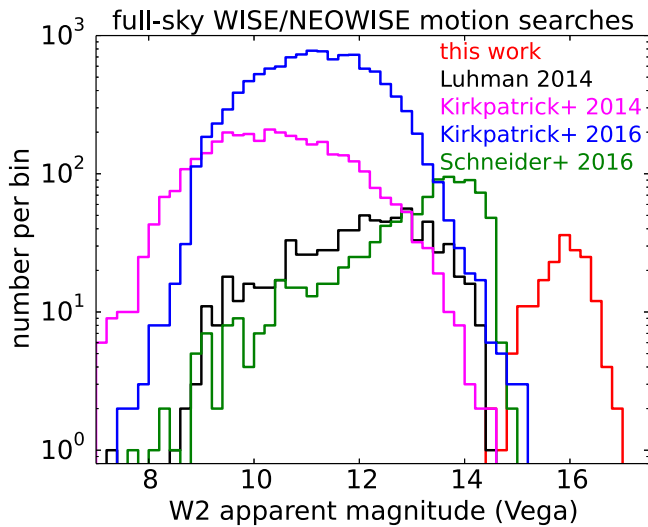


Figure 2. Comparison of $W2$ magnitude distributions for moving-object discoveries from published full-sky *WISE*/*NEOWISE* motion searches. Each histogram shows the number of new discoveries per 0.2 mag $W2$ bin for a given sample. Note the logarithmic scale. Red is our entire 174-object *Spitzer* p14034 target list (including four CPM targets and six spurious candidates from Section 7.1) plus our three brown dwarf candidates with $ch1/ch2$ photometry based on archival *Spitzer* imaging. Our discoveries are much fainter than those of previous full-sky *WISE*/*NEOWISE* motion searches.

therefore avoided selecting sources seen to have coincident $W3/W4$ emission as p14034 targets.

4.4.5. PanSTARRS-1 Cutouts

Before placing candidates on the p14034 target list, we inspected PanSTARRS-1 image cutouts²⁴ for objects north of $\delta \approx -30^\circ$ (Chambers et al. 2016). Visible detections in PanSTARRS-1 were in general used to veto potential Y dwarf candidates; given the faintness of our sample in $W2$, detection in any PanSTARRS-1 filter would be inconsistent with a Y dwarf spectral type.

5. General p14034 Sample Properties

We filled our allocated 40.5 hr of Cycle 14 *Spitzer* time with 174 unique brown dwarf candidate targets, each of which received a single corresponding AOR as detailed in Section 6. As discussed in Section 4, these 174 targets represent only a small subset of the visually vetted moving-object discoveries yielded by our searches. Figure 2 shows that our targets are much fainter than those of previous *WISE* motion surveys, including the AllWISE and AllWISE2 searches (Kirkpatrick et al. 2014, 2016). The median $W2$ magnitude of our targets is 15.93, with a dispersion of 0.47 mag. For comparison, the $W2$ single-exposure depth is $W2 \approx 14.5$, which has represented the faint limit of prior *WISE*-based motion searches (e.g., Luhman 2014a; Schneider et al. 2016). Figure 3 shows the $W2$ S/N distribution of our *Spitzer* photometry sample. The median (mean) $W2$ S/N is just 16.2 (18.4), with a dispersion of 8.6. Note that these values indicate the total $W2$ S/N when combining 4 yr of *WISE*/*NEOWISE* imaging; detections in any time slice of the available $W2$ imaging will generally be of even lower significance.

²⁴ <http://ps1images.stsci.edu/cgi-bin/ps1cutouts>

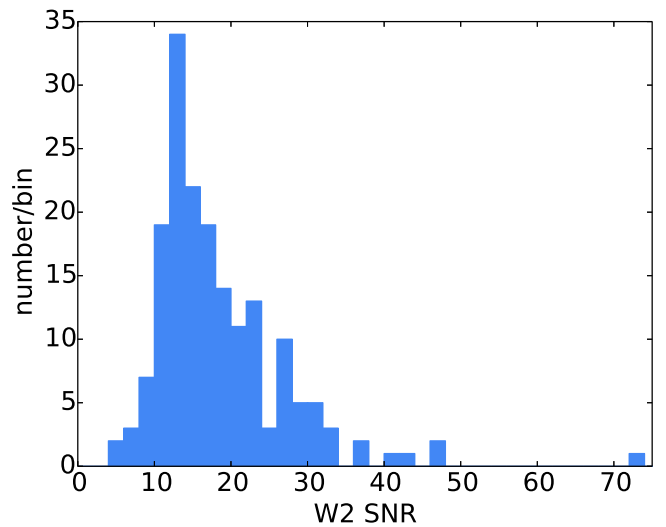


Figure 3. The $W2$ S/N distribution for our moving-object discoveries characterized with *Spitzer*. The histogram shows our entire 174-object *Spitzer* p14034 target list (including four CPM and six spurious candidates from Section 7.1) plus our three brown dwarf candidates with $ch1/ch2$ photometry based on archival *Spitzer* imaging. The median (mean) $W2$ S/N is 16.2 (18.4), with a dispersion of 8.6.

Figure 4 shows the spatial distribution of our p14034 targets, which, as expected, are scattered fairly uniformly across the entire sky while preferentially avoiding the confused Galactic plane.

5.1. Candidates with Archival $ch1/ch2$ Data

Three of our discoveries not previously recognized as brown dwarf candidates happened to have sufficient serendipitous archival $ch1/ch2$ imaging in SHA to enable robust phototyping without the need for additional p14034 observations. We performed our usual *Spitzer* photometry (Section 7) and astrometry (Section 8.4) on these archival observations to obtain $ch1-ch2$ colors. These three objects (CWISEP 0229+7246, CWISEP 1721+5950, and CWISEP 2247-0041) are denoted by blue squares in Figure 4.

5.2. Targets as Yet Unobserved by Spitzer

Three of our p14034 brown dwarf targets are scheduled for *Spitzer* photometry in the near future but remain unobserved by *Spitzer* as of this writing (2019 October; CWISEP 1353-0037, CWISEP 1515-2157, and CWISEP 0601-5922). In all three such cases, the motion is conclusively confirmed with *WISE* astrometry alone, so we have chosen to present these three discoveries in this paper despite the current lack of available *Spitzer* photometry/astrometry. These three targets are therefore listed in Table 1 but with the *Spitzer* photometry columns left empty.

6. Spitzer Observing Strategy

We based our observing strategy on those of prior *Spitzer* campaigns designed to measure the colors of *WISE*-selected late-T and Y dwarf candidates (e.g., programs 70062 and 80109; PI: Kirkpatrick). These foregoing *Spitzer* programs generally observed substantially brighter objects than those comprising our p14034 target list and showed that coaddition

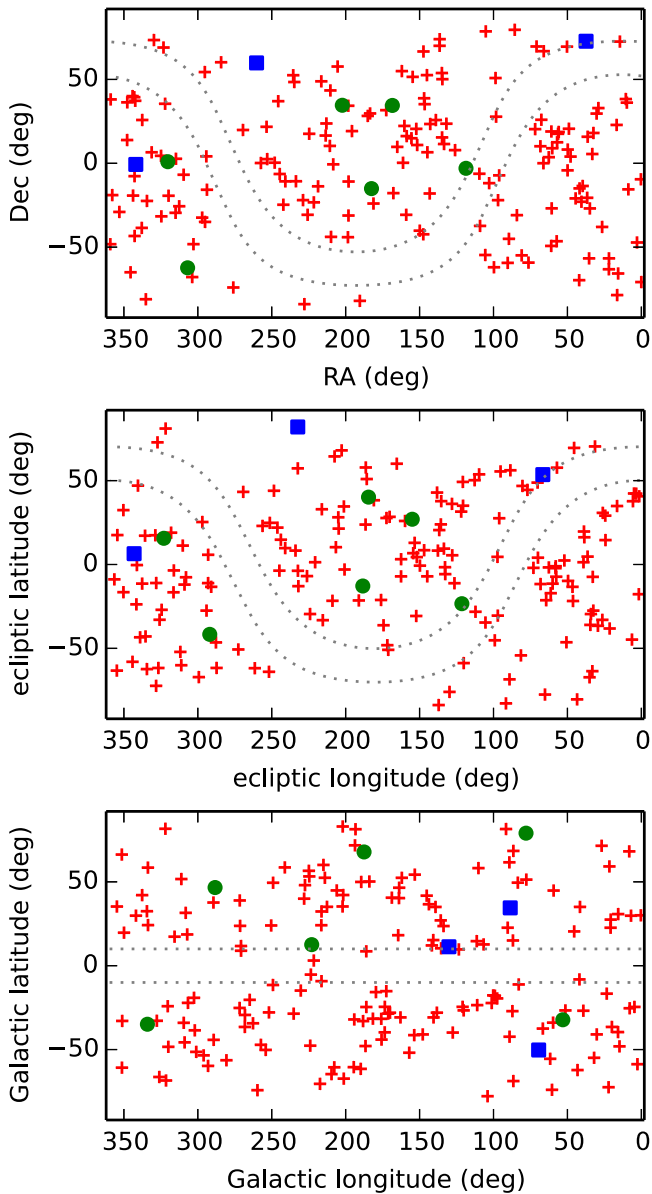


Figure 4. Spatial distribution of late-type brown dwarf candidates on p14034 or for which archival *Spitzer* data yielded a ch1–ch2 color. The CPM candidates have been removed, since they are presented separately in a forthcoming paper. Red plus signs are p14034 targets. Green circles are spurious p14034 candidates (see Table 2). Blue squares are brown dwarf candidates for which our ch1–ch2 colors are based on serendipitously available archival *Spitzer* imaging. Top: equatorial coordinates. Middle: ecliptic coordinates. Bottom: Galactic coordinates. In all cases, the dotted gray lines denote a Galactic latitude of $\pm 10^\circ$

of five 30 s ch1 dithers typically achieves an S/N of 10 (5) at a Vega magnitude of ch1 = 18.0 (18.75).

The boundary between the ch1–ch2 colors of late-T and Y dwarfs occurs at $\text{ch1} - \text{ch2} \approx 2.4$ (e.g., Kirkpatrick et al. 2019a), and our primary goal was to obtain ch1 imaging deep enough to distinguish between late-T and Y dwarfs. We therefore attempted to engineer our number of ch1 dithers such that a 5σ ch1 detection would always establish a color of at least $\text{ch1} - \text{ch2} = 2.75$ mag.

For each target, we chose either 5, 7, 9, 11, or 13 ch1 dithers (at 30 s dither⁻¹) so that we would achieve a ch1 S/N of at least 5 for $\text{ch1} - \text{ch2} = 2.75$, under the assumption that the ch2 mag

would be equal to the W2 mag. According to this strategy, $W2 \leq 16$ candidates receive five ch1 dithers, and the break point between five and seven dithers is $W2 = 16.0$. Then the break point between seven and nine dithers occurs at $W2 = 16.18$, and so forth. We exercised some case-by-case discretion in bumping up the exact number of dithers chosen but always used a ch1 S/N of 5 at $\text{ch1} - \text{ch2} = 2.75$ to enforce a minimum number of ch1 dithers.

For each target, both ch1 and ch2 were obtained as part of the same AOR. This minimizes slew overheads and ensures that our color measurements cannot be corrupted by any long timescale variability aliasing into images of the same target taken at large time separation. We always acquired the same number of 30 s dithers in both ch1 and ch2 for each target. This effectively maintains a fixed ch2 S/N of ~ 75 for the high-significance ch2 detection across all members of our sample, which ensures the high value of each target’s ch2 cycling detection for astrometry (Section 8.4). We dithered with a “cycling” pattern of medium scale.²⁵

The *Spitzer* p14034 imaging analyzed in this work was acquired between 2018 October 21 and 2019 August 16.

7. *Spitzer* Photometry

All of our *Spitzer* photometry/astrometry analyses presented in this work are based on custom mosaics built from the single-dither basic calibrated data (BCD) images with MOPEX (Makovoz & Khan 2005; Makovoz & Marleau 2005). We created one such custom mosaic per band (ch1, ch2) per AOR. Relative to using the default “PBCD” mosaics supplied for each AOR via SHA, creating our own custom mosaics provided us extra freedom to, for example, reject occasional problematic single-frame IRAC images with, e.g., a cosmic ray contaminating the targeted brown dwarf candidate. The algorithmic rejection of single-frame outliers such as cosmic rays also appears to be much better overall in our custom mosaics than in the PBCD stacks. In a handful of cases, we excised one or two BCD frames from our custom mosaics due to the presence of a cosmic ray contaminating the faint ch1 counterpart (CWISEP 0035–1532, CWISEP 0403–4916, CWISEP 1434–1344, CWISEP 2251–0740, and CWISEP 2355+3804).

Extraction and photometry of sources within our custom *Spitzer* mosaics proceeded as described in Section 4 of Marocco et al. (2019). In brief, we use the MOPEX/APEX software to detect sources in our custom mosaics and perform both point response function (PRF)-fit and aperture photometry (including the application of an aperture correction) in both ch1 and ch2. Note that our photometry was always run independently in ch1 and ch2; we did not employ a forced photometry approach. By default, we used an $S/N = 5$ source detection threshold. In the case of two very red objects (CWISEP 1434–1344 and CWISEP 1446–2317), obtaining a ch1 counterpart extraction required lowering the ch1 detection threshold to $S/N = 2$.

Table 1 lists our ch1 and ch2 photometry results. The quoted magnitude values and their uncertainties are derived by averaging the aperture-based and PRF-fit quantities for each target in each *Spitzer* band. Table 1 also reports the $W1$ and $W2$ photometry for each target. With only a small number of

²⁵ <https://irsa.ipac.caltech.edu/data/SPITZER/docs/irac/calibrationfiles/dither/>

Table 2
Spurious Candidates

p14034 AOR	CWISEP Designation	W2 (mag)
68510720	J075426.59–025947.8	16.36 ± 0.12
68502784	J111337.00+342927.0	16.48 ± 0.13
68505600	J121005.73–150533.3	15.97 ± 0.08
68733696	J132904.57+343524.4	16.31 ± 0.08
68577024	J202736.23–621855.5	16.68 ± 0.14
68506880	J212111.15+005640.0	16.34 ± 0.10

exceptions, such as our two discoveries not detected by CatWISE, this *WISE* magnitude information is drawn from the CatWISE columns w1mpro_pm, w1sigmpro_pm, w2mpro_pm, and w2sigmpro_pm.

7.1. Spurious Candidates

A small number of our p14034 targets turned out to be entirely absent in the deeper, higher-resolution *Spitzer* imaging we obtained (i.e., a *Spitzer* counterpart could neither be extracted nor visually identified). Table 2 lists such cases (6/174 = 3.4% of our targets). Throughout this paper, these six completely spurious targets are omitted from various tabulations and analyses, particularly those such as the ch1/ch2 photometry listed in Table 1, that would require a *Spitzer* detection.

We note that Eisenhardt et al. (2019) quoted a CatWISE reliability of just under 98% at $W2 = 16$. Given that our sample’s median magnitude is $W2 = 15.93$, a 3.4% rate of spurious sources is within reason.

7.2. Candidates with Two Spitzer Counterparts

In two cases, our *WISE*-based brown dwarf candidate turned out to have two distinct, closely spaced *Spitzer* ch2 counterparts. Candidate CWISEP 1541+5230 has two *Spitzer* counterparts in both ch1 and ch2, whereas CWISEP 0229+7246 has two *Spitzer* counterparts in ch2 but only one blended/elongated *Spitzer* counterpart in ch1. In these cases, we label the two components by adding a suffix of either “N” (northern) or “S” (southern) to their designations, based on their relative *Spitzer* ch2 (R.A., decl.) positions. In both of these cases, it remains plausible that there are simply two static *Spitzer* counterparts corresponding to our single *WISE* target, so we vetoed these candidates from being formally considered motion-confirmed in downstream analyses.

8. Astrometry

We seek to use motion as a proxy for confirming that an object is a nearby brown dwarf. High-significance motion establishes solar neighborhood membership, whereas objects consistent with remaining stationary may be, e.g., of extragalactic origin. Because we lack spectroscopic confirmations and our most interesting p14034 targets are detected only in *WISE* and *Spitzer*, detailed astrometric analysis is needed to best determine whether each source is indeed moving. In this section, we explain how we have combined astrometry from both *WISE* and *Spitzer* to best identify the subset of our brown dwarf candidates that have statistically significant proper motions. The inclusion of *Spitzer* astrometry is a critical component of this analysis, since our *Spitzer* data point provides a completely independent cross-check on the

perceived *WISE*-based motion used to select our candidates; if the *Spitzer* detection “lines up” along the *WISE* astrometric trajectory, then this gives us strong reassurance that the candidate was selected due to true motion rather than a rare fluke in the *WISE* data.

Using the methodology described here, we limit our astrometric analysis to fits of apparent linear motion; we do not seek to obtain/constrain the parallaxes of our targets. In general, fitting parallaxes for brown dwarfs as faint as our targets will require multiple epochs of *Spitzer* (or similarly precise) observations sampling both sides of the parallactic ellipse (e.g., Kirkpatrick et al. 2019a), whereas our p14034 imaging provides just a single *Spitzer* astrometric epoch. Additionally, as discussed in Section 8.3, we typically must coadd data acquired from both sides of *WISE*’s orbit in order to obtain $W2$ detections of our exceedingly faint targets, meaning that our *WISE* astrometry is generally unsuitable for parallax fitting.

Our astrometric analysis incorporates ch2 and $W2$ but never ch1 or $W1$. This is because our targets are very red in both ch1–ch2 and $W1$ – $W2$. For our p14034 *Spitzer* imaging, where both bands received the same total exposure time, the S/N of each target’s ch2 detection will be much higher than that of its ch1 detection. Further, because the ch1 and ch2 images of a given target are nearly contemporaneous, folding in ch1 does not offer the possibility of an appreciably extended time baseline, and in combination with ch2 astrometry, it would merely lead to a negligible improvement in the p14034 *Spitzer* positional precision. The same considerations apply with regard to $W1$: data acquisition in $W1$ and $W2$ is simultaneous, so $W1$ astrometry would provide only a set of much less precise positions at the same epochs as our $W2$ astrometric data points.

All *Gaia*-recalibrated $W2$ and ch2 (R.A., decl.) coordinates quoted throughout this paper are in the International Celestial Reference System (ICRS). The *Spitzer* and *WISE* positions reported in Tables 3 and 4 are relative rather than absolute; we did not attempt to correct for the typically very small parallaxes of our astrometric calibration sources.

8.1. Gauging Significance of Motion

There are various ways one could imagine quantifying significance of motion. In this work, we opt for a simple, intuitive metric that has been applied in the course of past *WISE*-based moving-object analyses:

$$\chi_{\text{motion}}^2 = (\mu_{\alpha}/\sigma_{\mu_{\alpha}})^2 + (\mu_{\delta}/\sigma_{\mu_{\delta}})^2. \quad (2)$$

This χ_{motion}^2 statistic has previously been used during, e.g., the AllWISE and AllWISE2 motion surveys (Kirkpatrick et al. 2014, 2016). It tends to increase with larger (absolute) linear motion components, as well as with decreasing uncertainties on the linear motion measurements. It can also be thought of as corresponding to a false-alarm rate, $Q = e^{-\chi_{\text{motion}}^2/2}$, where Q is the probability of a statistical fluke causing χ_{motion}^2 to be exceeded.

In this work, we set the threshold for *WISE*+*Spitzer* “motion confirmation” at $Q = 10^{-5}$, which corresponds to $\chi_{\text{motion}}^2 = 23.03$. Ignoring the relatively high-precision *Spitzer* astrometric data points available from p14034 follow-up, a substantial fraction of our sample’s targets (46% = 79/173) have CatWISE χ_{motion}^2 less than this threshold, illustrating the critical need to combine ch2 and $W2$ astrometry toward better confirming/refuting source motions.

Table 3
WISE W2 Positions Used in Joint *WISE+Spitzer* Linear Motion Fits

Name	R.A. (deg, ICRS)	Decl. (deg, ICRS)	$\sigma_{\text{R.A.}}$ (mas)	$\sigma_{\text{decl.}}$ (mas)	Time Slice ^a	Mean MJD
CWISEP J000006.01–704851.2	0.025954	–70.814036	424	408	pre	55,404.23
	0.024768	–70.814293	283	267	post	57,330.72
CWISEP J000110.81–093215.5	0.294481	–9.537603	678	691	pre	55,431.64
	0.295332	–9.537668	539	540	post	57,387.92
CWISEP J001146.07–471306.8	2.941300	–47.218389	620	625	pre	55,442.17
	2.942075	–47.218477	364	361	post	57,398.73
CWISEP J003507.77–153233.8	8.782612	–15.542104	422	426	pre	55,447.53
	8.782597	–15.542193	481	469	post0_1yr	56,747.59
	8.782337	–15.542798	396	394	post1_1yr	57,115.18
	8.782461	–15.542872	358	357	post2_1yr	57,476.03
	8.782416	–15.543088	469	472	post3_1yr	57,863.72

Note.

^a See Section 8.3 and Table 5 for discussion and definitions of the *WISE* time slices used for W2 astrometry.

(This table is available in its entirety in machine-readable form.)

8.2. Strategy for Combining *WISE* and *Spitzer* Astrometry

Given that CatWISE linear motion estimates are almost always available for our targets, one might imagine concocting a scheme to combine these with our *Spitzer* astrometric data points and thereby derive high-quality *WISE+Spitzer* linear motions. There are many reasons why we find this approach undesirable.

1. It is not entirely clear how to properly combine a CatWISE motion estimate and a *Spitzer* position in order to obtain a χ^2_{motion} value.
2. Two of our most exciting discoveries are absent from the CatWISE catalog (WISEA 1534–1043 and WISENF 1936+0408). Two other targets have “null” motion uncertainties in CatWISE (CWISEP 0402–2651 and CWISEP 0430+2556). So, in any event, we need to develop an alternative motion-fitting methodology not reliant on CatWISE to address this subset of our targets.
3. In cases when CatWISE linear motions are corrupted by blending at some subset of *WISE* epochs, this can be circumvented by careful subselection of epochal W2 detections.
4. CatWISE used an ad hoc scaling of unWISE pixel-level uncertainties, which could lead to nonoptimal CatWISE motion uncertainty estimates.
5. CatWISE only incorporated NEOWISE data through 2016, whereas additional NEOWISE data are now available.
6. CatWISE fits *W1* and *W2* simultaneously; any nonzero weighting of *W1* data in CatWISE motion fits will essentially have added noise to its motion measurements for our *W2*-only sources.

The alternative approach we prefer is to extract our own epochal *WISE* source catalogs and use these to assemble a vetted list of high-quality W2 astrometric detections for each brown dwarf candidate. For each target, its set of W2 detections can then be straightforwardly combined with our *Spitzer* astrometric data point via simple least-squares fitting of apparent linear motions in both R.A. and decl. Moreover, the carefully assembled lists of W2 positions derived during this process may be of substantial interest in their own right, as they can be combined with any

future astrometric follow-up acquired. Section 8.3 (Section 8.4) explains in detail how we obtain the *WISE* W2 (*Spitzer* ch2) astrometric detections for our targets.

8.3. *WISE* Astrometry

It is challenging to obtain a time series of *WISE* astrometric detections for moving sources as faint as our targets. By selection, our brown dwarf candidates tend to be completely undetected in *W1*. In *W2*, they typically have an S/N of just ~ 15 even when combining 4 yr of *WISE*/NEOWISE data (see Figure 3). As a result, it is almost never possible to extract single-exposure W2 astrometry for any target in our sample, and we do not attempt to do so. Furthermore, in most cases, it is not possible to obtain W2 detections of our targets even in time-resolved unWISE coadds that stack together the $\gtrsim 12$ W2 exposures at each sky location during each single 6 month *WISE* sky pass. Therefore, we often must perform source extraction on W2 stacks that combine multiple *WISE* sky passes.

The latest full-sky unWISE data release (Meisner et al. 2019) provides time-resolved coadds that bin W2 exposures into a series of single *WISE* sky passes, incorporating both the prehibernation time period (2010–2011) and the first 4 yr of NEOWISE-R observations (2013–2017). These time-resolved unWISE coadds form the starting point for our W2 astrometry analysis. Ideally, we would also have access to such unWISE coadds for the 2018 time period, but these have not yet been generated. However, since the 2018 NEOWISE-R data are only slightly earlier in time than our *Spitzer* p14034 imaging, there would be relatively little marginal benefit attained by including 2018 W2 data; this additional W2 imaging would not increase our overall *WISE+Spitzer* time baseline and would only contribute a relatively weak astrometric constraint adjacent in time to our much higher precision p14034 *Spitzer* data point. With the Meisner et al. (2019) unWISE data set, we typically have 5 yr of W2 imaging available at each sky location, corresponding to 10 time-resolved W2 coadds, which are labeled e000, e001, ..., e009. For concreteness, one representative cadence of such time-resolved unWISE coadds at fixed sky locations is e000 \sim 2010.4, e001 \sim 2010.9, e002 \sim 2014.4, ..., e009 \sim 2017.9.

Table 4
Recalibrated *Spitzer* ch2 Positions

Name	AOR	R.A. (deg, ICRS)	Decl. (deg, ICRS)	$\sigma_{R.A.}$ (mas)	$\sigma_{decl.}$ (mas)	MJD	Method Number ^a	N_{calib}
CWISEP J000006.01−704851.2	68730112	0.02385537	−70.81443752	42	36	58,711.09	2	13
CWISEP J000110.81−093215.5	68727808	0.29543643	−9.53797990	25	27	58,559.84	3	8
CWISEP J001146.07−471306.8	68486656	2.94245662	−47.21861888	47	59	58,531.38	3	9
CWISEP J003507.77−153233.8	68235776	8.78254804	−15.54325614	25	32	58,427.81	3	6
CWISEP J003915.43+360939.0	68506112	9.81402661	36.16052959	26	23	58,583.45	1	12
CWISEP J004158.35+381811.9	68486144	10.49371897	38.30336814	35	42	58,468.55	1	10
CWISEP J005802.63+723330.3	68731904	14.51001015	72.55856213	65	54	58,594.58	1	35
CWISEP J010247.48−654226.4	68509952	15.69697472	−65.70750484	62	40	58,473.60	6	12
CWISEP J010527.69−783419.3	68237568	16.36883289	−78.57247246	52	24	58,433.05	1	14
CWISEP J010650.61+225159.1	68234752	16.71061275	22.86605883	21	35	58,422.33	3	9
CWISEP J012735.44−564110.5	68495360	21.89769161	−56.68621504	27	57	58,499.03	3	7
CWISEP J012748.35−631056.1	68732672	21.95195768	−63.18183282	49	43	58,551.68	3	16
CWISEP J014607.55−375505.6	68497408	26.53242038	−37.95091598	21	20	58,552.20	3	7
CWISEP J015613.24+325526.6	68164096	29.05688486	32.92350544	46	46	58,440.24	2	16
CWISEP J020103.10+293801.8	68504320	30.26370010	29.63336271	33	30	58,470.04	3	11
CWISEP J020938.72+180427.7	68500992	32.41199524	18.07415696	32	45	58,471.93	3	8
CWISEP J021243.55+053147.2	68556032	33.18130221	5.52993419	29	30	58,599.83	3	6
CWISEP J021921.66−265451.8	68730368	34.84078553	−26.91396331	75	74	58,574.21	3	5
CWISEP J022122.41−564125.0	68494848	35.34405691	−56.69029231	23	21	58,472.54	2	10
CWISEP J022513.27+154854.8	68725760	36.30567186	15.81531619	145	83	58,602.87	9	11
CWISEP J022631.82−203439.4	68164352	36.63215752	−20.57838279	71	73	58,431.15	6	10
CWISEP J022935.43+724616.4 N	26741760	37.39850608	72.77155816	93	83	54,906.77	1	40
CWISEP J022935.43+724616.4 S	26741760	37.39665397	72.77113514	86	75	54,906.77	1	40
CWISEP J023842.60−133210.7	68728576	39.67740350	−13.53752892	62	54	58,603.20	3	7
CWISEP J024204.91−225604.6	68557056	40.52249074	−22.93446201	29	31	58,593.64	3	6
CWISEP J024710.25−145809.9	68731392	41.79265236	−14.96945429	67	42	58,593.43	9	7
CWISEP J024810.75−694127.9	68726784	42.04500470	−69.69113100	50	33	58,552.21	1	12
CWISEP J025747.92−205602.7	68497152	44.44969657	−20.93370573	22	34	58,470.58	3	8
CWISEP J031130.28+035931.8	68507648	47.87685640	3.99246667	61	64	58,467.98	2	10
CWISEP J031557.05+203552.4	68727296	48.98782628	20.59796257	42	38	58,617.90	1	11
CWISEP J031908.60+081120.4	68498432	49.78556821	8.18886652	75	74	58,467.53	3	5
CWISEP J031935.50−041231.7	68577280	49.89853078	−4.20885654	37	40	58,609.04	3	9
CWISEP J032109.59+693204.5	68498688	50.29368774	69.53427617	37	39	58,469.54	1	46
CWISEP J034336.27+184025.8	68733952	55.90073168	18.67369501	48	48	58,624.93	3	13
CWISEP J034514.82+173528.1	68728064	56.31200628	17.59095052	28	28	58,624.94	3	11
CWISEP J034755.11+123051.9	68164608	56.97973852	12.51497456	31	25	58,468.24	2	11
CWISEP J034904.05−462827.9	68487424	57.26737072	−46.47365188	32	35	58,473.58	3	10
CWISEP J040106.67+085748.5	68500736	60.27822056	8.96294780	28	37	58,468.53	3	14
CWISEP J040235.55−265145.4	68727552	60.64958777	−26.86361399	63	54	58,603.19	3	10
CWISEP J040324.67+185729.6	68505856	60.85263479	18.95816852	56	40	58,471.91	2	11
CWISEP J040351.00−491605.6	68487680	60.96303694	−49.26790141	38	41	58,471.68	3	10
CWISEP J041025.10+033807.2	68729856	62.60462293	3.63527815	33	30	58,635.20	2	11
CWISEP J042455.68+000221.4	68728832	66.23229318	0.03921896	43	30	58,633.86	2	12
CWISEP J042404.54+665011.2	68486912	66.02027373	66.83636451	34	48	58,479.14	1	27
CWISEP J043034.27+255653.7	68556544	67.64342191	25.94810246	31	32	58,635.21	1	18
CWISEP J043309.31+100902.9	68236544	68.28907254	10.15026354	27	37	58,471.05	2	15
CWISEP J044330.73+693828.3	68728320	70.87836222	69.64102641	50	46	58,648.83	1	22
CWISEP J044719.61+202158.1	68726016	71.83173489	20.36516650	32	28	58,640.93	1	16
CWISEP J050521.29−591311.7	68493056	76.34040148	−59.22162499	33	33	58,493.60	2	17
CWISEP J052346.34−545314.7	68499712	80.94401093	−54.88680636	42	37	58,490.76	3	10
CWISEP J053644.82−305539.3	68508416	84.18683452	−30.92759191	32	23	58,481.51	1	10
CWISEP J054233.06+793459.1	68732928	85.63799445	79.58314781	36	29	58,559.34	1	12
CWISEP J055816.68−450233.6	68492800	89.56940192	−45.04252697	87	44	58,481.69	2	17
CWISEPR J062436.84−071147.2	68491264	96.15341104	−7.19629315	40	26	58,516.85	1	41
CWISEP J062742.27−215908.1	68504832	96.92623170	−21.98606594	30	31	58,518.01	1	18
CWISEP J063257.49+274629.4	68499200	98.23934757	27.77502111	40	39	58,503.44	1	33
CWISEP J063428.10+504925.9	68495104	98.61732182	50.82257394	38	33	58,507.81	1	17
CWISEP J063845.48−615937.2	68488704	99.68882416	−61.99337025	71	46	58,490.24	1	20
CWISEPR J065144.62−115106.1	68493824	102.93589409	−11.85194477	27	26	58,535.78	1	38
CWISEP J070055.19+783834.0	68486400	105.23691074	78.64175314	46	46	58,494.47	1	10
CWISEP J070214.84−544041.7	68496128	105.56188808	−54.67901657	45	47	58,516.88	1	20
CWISEP J071626.02−371951.1	68555776	109.10839230	−37.33077950	39	33	58,535.13	1	32
CWISEP J071813.30−061421.1	68508160	109.55593921	−6.23914659	69	68	58,516.86	1	57

Table 4
(Continued)

Name	AOR	R.A. (deg, ICRS)	Decl. (deg, ICRS)	$\sigma_{R.A.}$ (mas)	$\sigma_{decl.}$ (mas)	MJD	Method Number ^a	N_{catib}
CWISEP J082400.43+075019.9	68509184	126.00164205	7.83894211	75	72	58,535.12	2	17
CWISEP J084726.55+233558.1	68488960	131.86076818	23.59920333	37	36	58,539.98	3	7
CWISEP J085348.15+112921.5	68507904	133.45069449	11.48919129	33	47	58,539.96	2	11
CWISEP J085820.46+500834.4	68501504	134.58499868	50.14282167	54	33	58,524.29	2	12
CWISEP J085908.26+152527.1	68238080	134.78440239	15.42385142	29	47	58,539.97	3	10
CWISEP J085938.95+534908.7	68556288	134.91174975	53.81867728	34	44	58,540.02	3	9
CWISEP J090547.50+700239.8	68730880	136.44865859	70.04452095	26	21	58,559.33	3	7
CWISEP J090536.35+740009.1	68489472	136.40333548	74.00079349	31	48	58,509.74	3	9
CWISEP J091558.51+254713.2	68508672	138.99385676	25.78653366	39	44	58,543.08	3	10
CWISEP J093111.03+232502.1	68492544	142.79561049	23.41658011	32	33	58,544.06	3	5
CWISEP J093236.66−180029.3	68489216	143.15217919	−18.00838695	34	31	58,567.17	1	20
CWISEP J093852.89+063440.6	68494336	144.72114196	6.57700050	46	50	58,555.38	4	10
CWISEP J094005.50+523359.2	68503296	145.02227353	52.56601748	46	24	58,542.98	3	11
CWISEP J094615.56+351434.3	68493312	146.56454664	35.24200351	58	51	58,542.05	2	11
CWISEP J094742.83+384619.3	68498176	146.92830968	38.77175299	91	49	58,542.04	6	11
CWISEP J094930.41+663937.2	68729600	147.37660966	66.66003119	54	45	58,553.28	3	10
CWISEP J094957.15−422017.1	68733184	147.48854442	−42.33802594	109	108	58,574.40	1	70
CWISEP J095930.71−401046.8	68577536	149.87817796	−40.18036991	112	111	58,577.93	1	45
CWISEP J100629.01+105408.5	68495616	151.62049970	10.90239112	35	29	58,577.18	2	10
CWISEP J100854.84+203136.6	68732160	152.22829729	20.52654386	37	58	58,558.69	6	5
CWISEP J101841.86+513108.8	68727040	154.67452734	51.51934616	40	44	58,553.29	3	9
CWISEP J102201.27+145520.2	68503552	155.50450138	14.92207108	33	41	58,559.99	3	6
CWISEP J103453.14+161228.0	68499456	158.72109612	16.20759141	34	65	58,559.98	3	5
CWISEP J103607.94−304253.1	68510208	159.03281467	−30.71484791	54	54	58,587.81	1	17
CWISEP J104104.20+221613.6	68509696	160.26712707	22.26973552	47	41	58,594.51	3	6
CWISEP J104446.56+001754.9	68502528	161.19281382	0.29845508	32	33	58,581.39	3	9
CWISEP J104756.81+545741.6	68500480	161.98547964	54.96133792	37	38	58,542.02	3	9
CWISEP J110021.08+094652.9	68493568	165.08682533	9.78115233	40	39	58,572.32	9	8
CWISEP J111055.12−174738.2	68238592	167.72963950	−17.79455020	70	40	58,602.18	3	13
CWISEP J113010.21+313947.3	68487936	172.54105818	31.66144612	42	64	58,600.82	9	5
CWISEP J120444.33−235926.8	68236800	181.18437510	−23.99145802	31	31	58,602.17	1	14
CWISEP J121358.13+294237.0	68505344	183.49219972	29.71013447	40	39	58,574.96	3	9
CWISEP J122010.03+281431.3	68494080	185.04120626	28.24171721	32	31	58,598.77	3	7
CWISEP J124138.41−820051.9	68238848	190.41152361	−82.01423050	57	50	58,425.32	1	33
CWISEP J130255.54+191145.9	68489984	195.73155415	19.19573617	53	83	58,602.15	3	7
CWISEP J131252.97+341746.5	68510464	198.22107861	34.29598342	55	49	58,591.64	3	8
CWISEP J131208.16−105231.8	68492032	198.03385882	−10.87573942	41	52	58,613.40	3	13
CWISEP J131221.97−310845.7	68494592	198.09075160	−31.14658275	31	30	58,624.55	1	10
CWISEP J131350.91−440352.2	68490752	198.46126925	−44.06479216	38	32	58,622.95	1	31
CWISEP J134143.75+574112.9	68504576	205.43234762	57.68666593	29	78	58,573.15	3	6
CWISEP J135937.65−435226.9	68509440	209.90630307	−43.87448090	35	41	58,633.49	1	37
CWISEP J140118.30+432554.2	68235008	210.32602811	43.43087557	43	30	58,419.34	3	8
CWISEP J140247.83+102132.6	68487168	210.69909427	10.35917083	49	42	58,613.41	9	7
CWISEP J141206.85+234412.4	68491776	213.02755699	23.73700131	48	34	58,613.43	3	8
CWISEP J141400.68+163153.9	68729088	213.50312991	16.53217610	61	69	58,613.42	3	8
CWISEP J142552.36+485151.3	68726528	216.46796266	48.86471825	58	61	58,588.79	3	9
CWISEP J143439.23−134421.4	68500224	218.66269634	−13.73975795	53	46	58,633.47	2	13
CWISEP J144606.62−231717.8	68496896	221.52628287	−23.28947384	33	37	58,633.48	2	18
CWISEP J145837.91+173450.1	68726272	224.65736126	17.58070375	32	27	58,626.15	2	10
CWISEP J150252.82−304232.8	68237056	225.71946267	−30.70927564	25	33	58,427.80	1	13
CWISEP J151140.51−835918.0	68507136	227.91888011	−83.98841937	42	40	58,490.23	1	19
WISEA J153429.75−104303.3	68555520	233.62091671	−10.72358186	27	28	58,644.32	1	20
CWISEP J153859.39+482659.1	68238336	234.74784024	48.44903282	45	54	58,418.52	3	7
CWISEP J154151.59+523025.0 N	68497920	235.46579224	52.50681563	57	91	58,598.11	3	9
CWISEP J154151.59+523025.0 S	68497920	235.46449495	52.50617877	61	93	58,598.11	3	9
CWISEP J160311.60−104620.4	68492288	240.79914670	−10.77353243	30	26	58,469.19	1	11
CWISEP J160835.01−244244.7	68239104	242.14628653	−24.71251400	33	25	58,442.21	1	36
CWISEP J161822.86−062310.2	68499968	244.59521009	−6.38637035	26	31	58,469.19	1	13
CWISEP J162225.92+370118.8	68496384	245.60729535	37.02130786	38	46	58,469.15	2	10
CWISEP J163200.11+002108.6	68507392	248.00057619	0.35253114	46	46	58,469.17	1	11
CWISEP J165215.62+022918.5	68506368	253.06567761	2.48859715	58	57	58,469.16	1	21
CWISEP J165359.67+214457.2	68557312	253.49875382	21.74888542	40	33	58,657.06	2	17
CWISEP J170918.83+000950.5	68729344	257.32831459	0.16432932	26	27	58,669.54	1	26

Table 4
(Continued)

Name	AOR	R.A. (deg, ICRS)	Decl. (deg, ICRS)	$\sigma_{R.A.}$ (mas)	$\sigma_{decl.}$ (mas)	MJD	Method Number ^a	N_{calib}
CWISEP J172104.42+595047.7	3862272	260.26838196	59.84667974	61	40	52,975.74	1	16
CWISEP J175746.31+195112.6	68502272	269.44282233	19.85352764	32	32	58,471.97	1	31
CWISEP J182358.73-740246.0	68233216	275.99657525	-74.04641231	56	52	58,448.99	1	23
CWISEP J185658.80+601351.4	68730624	284.24430005	60.22964024	30	36	58,559.33	1	12
CWISEP J193518.58-154620.3	68488448	293.82778626	-15.77235013	29	25	58,493.51	1	52
WISENF J193656.08+040801.2	68576768	294.23235507	4.13120728	31	20	58,525.50	1	92
CWISEP J194027.48-345650.6	68504064	295.11449035	-34.94751455	48	47	58,493.51	1	23
CWISEP J194101.59+542335.9	68498944	295.25670541	54.39298422	31	34	58,471.96	1	34
CWISEP J194812.42-322334.9	68503808	297.05120413	-32.39295664	42	27	58,494.13	1	21
CWISEP J201146.45-481259.7	68239360	302.94397653	-48.21692427	43	33	58,503.06	1	14
CWISEP J201510.68-675005.6	68501248	303.79406769	-67.83508286	31	37	58,472.53	2	12
CWISEP J203821.53-064930.9	68556800	309.58944064	-6.82578390	36	25	58,510.33	1	17
CWISEP J205019.99-253652.8	68233984	312.58304287	-25.61494640	26	37	58,508.48	2	13
CWISEP J205908.95+024105.6	68731136	314.78863725	2.68416011	30	30	58,551.33	1	17
CWISEP J210007.87-293139.8	68503040	315.03349264	-29.52788224	37	38	58,509.48	2	17
CWISEP J211909.29-192117.4	68490240	319.78904654	-19.35486447	31	26	58,517.11	2	15
CWISEP J212828.05+352912.4	68236032	322.11672271	35.48637727	75	75	58,432.61	1	51
CWISEP J213249.05+690113.7	68234496	323.20530812	69.02077519	55	44	58,425.07	1	24
CWISEP J213838.74-313808.5	68234240	324.66221995	-31.63611554	22	35	58,515.05	1	13
CWISEP J213930.45+042721.6	68497664	324.87702071	4.45537284	25	22	58,531.97	1	16
CWISEP J215841.50+732842.7	68502016	329.67344392	73.47850960	114	29	58,467.44	1	23
CWISEP J220452.02+063343.4	68731648	331.21632223	6.56188601	64	43	58,551.77	6	16
CWISEP J221736.94-222647.6	68235520	334.40396987	-22.44652307	49	38	58,529.15	2	12
CWISEP J222035.35-810322.6	68233728	335.14895865	-81.05653137	51	43	58,435.14	1	10
CWISEP J223022.60+254907.5	68491008	337.59325011	25.81806309	47	38	58,548.77	1	19
CWISEP J223138.55-383057.2	68506624	337.91150228	-38.51649715	35	27	58,523.83	3	9
CWISEP J224747.42-004103.6	46949376	341.94749199	-0.68427358	58	65	56,312.31	1	12
CWISEP J224916.17+371551.4	68505088	342.31707292	37.26374196	32	31	58,554.12	1	19
CWISEP J225059.28-432057.2	68164864	342.74751734	-43.34975131	38	73	58,523.86	3	11
CWISEP J225156.13+392408.4	68237824	342.98339318	39.40224969	24	29	58,420.28	1	21
CWISEP J225109.50-074037.7	68233472	342.79053727	-7.67692220	40	36	58,548.47	2	11
CWISEP J225511.56-191516.3	68508928	343.79803367	-19.25520324	131	131	58,541.14	2	10
CWISEP J225628.97+400227.3	68489728	344.12214325	40.04078021	29	29	58,562.32	1	24
CWISEP J230158.30-645858.3	68235264	345.49336781	-64.98352893	34	21	58,490.77	3	10
CWISEP J231047.80+362004.6	68732416	347.69962913	36.33475502	37	33	58,574.50	1	18
CWISEP J231114.50+135148.5	68733440	347.81001500	13.86352942	32	48	58,559.36	3	9
CWISEP J233216.39-290025.0	68496640	353.06832785	-29.00730341	28	21	58,540.94	3	10
CWISEP J235130.42-185800.2	68236288	357.87760747	-18.96682764	40	27	58,425.09	6	9
CWISEP J235547.99+380438.9	68163840	358.95117559	38.07755247	38	41	58,422.31	1	21
CWISEP J235644.78-481456.3	68165120	359.18817070	-48.24923064	29	29	58,412.37	3	5

Notes. Here N_{calib} is the number of *Gaia* DR2 calibrators used for *Spitzer* ch2 astrometric recalibration of each AOR, as discussed in Section 8.4.1.

^a The astrometric calibrator selection “method number” here refers to the method number listed in Table 6 and explained in Section 8.4.1.

(This table is available in machine-readable form.)

In gathering astrometric detections for our brown dwarf candidates, we always attempt extractions from all available *e*?? *W2* unWISE coadds. Because this still leaves many of our faint targets undetected, we also generate and perform source extraction on a set of *W2* “meta-coadd” time slices. This set of meta-coadd slices is listed in Table 5. The “pre” slice stacks all prehibernation *e*?? *W2* unWISE coadds together to form a deeper 2010–2011 meta-coadd. Analogously, the “post” slice stacks all posthibernation *e*?? *W2* unWISE coadds together, resulting in a deep 2013–2017 coadd. The “post?_1yr” meta-coadd slices stack the posthibernation *e*?? *W2* unWISE coadds within a series of four nonoverlapping 1 yr time intervals. Lastly, the “post?_2yr” meta-coadd slices stack the postre-activation *e*?? *W2* unWISE coadds within a series of two nonoverlapping 2 yr time intervals.

We generate our *W2* meta-coadds for the full $1^{\circ}56 \times 1^{\circ}56$ unWISE coadd tile footprint containing each target. This has multiple advantages relative to considering only small postage stamps about our targets. First, it allows us to obtain a large number of *Gaia* DR2 (Gaia Collaboration et al. 2018) calibrator sources with which to produce refined world coordinate system (WCS) solutions for each *W2* time slice (Section 8.3.1). Second, it provides sufficient numbers of bright point sources to accurately model the *W2* point-spread function (PSF) within each time slice.

We create *W2* meta-coadds by performing an inverse variance-weighted sum of the contributing *e*?? unWISE coadds, making use of the unWISE `-invvar-m` inverse variance maps. Using these same inverse variance weights, we also create a corresponding map of the mean MJD for each

Table 5
unWISE Meta-coadd Time Slices

Time Slice Name	Approx. Time Period (Calendar Years)
pre	2010.0–2011.1
post	2014, 2015, 2016, and 2017
post0_1yr	2014
post1_1yr	2015
post2_1yr	2016
post3_1yr	2017
post0_2yr	2014 and 2015
post1_2yr	2016 and 2017

meta-coadd, enabling us to quote MJD values corresponding to our *W2* astrometric detections.

Our modeling of the time-resolved unWISE coadds and meta-coadds, including source detection and centroiding, was performed using the `crowdsourc` crowded field photometry pipeline (Schlafly et al. 2019). The `crowdsourc` pipeline has proven adept at modeling unWISE *W1* and *W2* images during creation of the full-sky unWISE Catalog (Schlafly et al. 2019). It derives a PSF model for each unWISE image it processes and reports profile-fit astrometry that is equivalent to flux-weighted centroiding because the nominal PSF center is defined to coincide with the PSF model’s flux-weighted centroid.

For the unWISE tile footprint containing each target, we ran `crowdsourc` on all *W2* time-resolved coadds (e??? time slices) and all meta-coadds (Table 5 time slices). Next, we proceeded to select the subset of these `crowdsourc` detections that are counterparts to each brown dwarf candidate and will ultimately be combined with *Spitzer* astrometry during our final linear motion fits. We began by identifying a visually vetted set of prehibernation *W2* `crowdsourc` counterparts, one for each target. In combination with our *Spitzer* positions (Section 8.4), this allowed us to bracket each target’s ~ 2010 – 2019 trajectory and derive a crude linear motion estimate. Using this preliminary motion estimate, we then identified all `crowdsourc` detections near the moving object’s trajectory in all time slices. We visually inspected all such potential counterparts, removing severe blends and static contaminants.

The last step in selecting `crowdsourc` detections for our final *WISE+Spitzer* motion fits is to pare down the full set of available detections for each target into a list that incorporates information from each *WISE* sky pass exactly once.²⁶ In this context, our faintest targets are the simplest. These objects will only have *W2* detections in the deepest meta-coadds on each side of the *WISE* hibernation boundary: the “pre” and “post” time slices. Indeed, the simple combination of “pre” and “post” `crowdsourc` astrometry was adopted for 104 of our 167 targets,²⁷ as can be seen in Table 3. For brighter targets, we have the freedom to choose the specific set of time slices

²⁶ In some rare cases, such as moving objects severely blended with static contaminants at certain *WISE* epochs, it was not possible (or desirable) to achieve this idealized goal.

²⁷ In the course of this work, we consider a total of 177 moving-object candidates: 174 from our p14034 campaign and three with archival *Spitzer* imaging. Table 3 omits four of these discoveries that will be presented in an upcoming paper on CatWISE CPM systems (Marocco et al. 2020) and another six targets that turned out to be spurious (Section 7.1), leaving 167 objects in Table 3.

adopted. For instance, bright targets will have e000, e001, and “pre” time slice detections available. We cannot use all of these in our joint *WISE+Spitzer* fits, since this would effectively double count *W2* imaging during the 2010–2011 time period. In these situations, we carefully constructed lists of `crowdsource` detections for each target that omitted as few *W2* sky passes as possible while never double counting. In doing so, we enforced a preference for shorter time slices, with the rationale being that longer time slices incur more smearing of the moving object, which is nonoptimal for centroid measurements. Table 3 lists the *W2* time slices employed for each target in our production *WISE+Spitzer* linear motion fits. On average, ~ 3 *W2* detections per target are used.

8.3.1. *W2* Astrometric Recalibration

The time-resolved unWISE coadds inherit low-level (up to a few hundred mas) astrometric systematics by virtue of propagating the single-exposure *WISE* astrometry without modification (Meisner et al. 2018b, 2019). We therefore sought to improve the accuracy of our `crowdsourc` *W2* astrometry by recalibrating it to *Gaia* DR2.

For the `crowdsourc` catalog corresponding to each time slice of each unWISE tile footprint, we seek to compute a scalar astrometric offset along each sky direction so as to bring our *W2* centroids into best agreement with *Gaia* DR2. In practice, this is accomplished by adding a small offset to each of the two CRPIX components in the native *W2* unWISE coadd WCS.

Each coadd from which we draw a brown dwarf candidate *W2* detection covers an ~ 2.4 deg² sky area, resulting in an abundance of available *Gaia* DR2 calibrators. To assemble a set of *Gaia*–`crowdsourc` calibration sources, we cross-match the full list of `crowdsourc` detections against a subset of *Gaia* DR2 rows using a 2'' radius. We require that our *Gaia* DR2 astrometric calibrators have *Gaia* proper motions available, and we use these to propagate each calibrator’s position to the mean epoch of the *W2* coadd under consideration. We do not attempt to correct for the *Gaia* calibrator parallaxes, which have a mean amplitude of only ~ 1 – 2 mas. The median number of *Gaia* DR2 calibrators employed per *W2* coadd is 6880.

With *Gaia* positions at the relevant epoch in hand, we calculate the two-element shift that needs to be applied to the native CRPIX to zero out the median offsets between the *Gaia* calibrators and their `crowdsourc` matches along the coadd *x* and *y* pixel directions. We then apply this offset to create a slightly modified CRPIX value that, in combination with the other native *W2* WCS parameters, provides a recalibrated astrometric solution most consistent with *Gaia* at zeroth order.

The mean amplitude of the per-coordinate offsets applied to the native CRPIX values is ~ 50 mas. Using the recalibrated WCS for each coadd, the typical bright end scatter (assessed with $10 < W2 < 11.6$ unsaturated sources) relative to the *Gaia* “truth” is just 44 mas (41 mas) in R.A. (decl.). This is a very small fraction of the $\sim 6''$ *W2* PSF FWHM ($\sim 1/150$ FWHM), providing confidence in the astrometric fidelity of our *W2* (meta-)coadds.

The systematics floor of our *W2* astrometry as characterized by the bright end scatter is very small compared to the typical per-coordinate statistical uncertainties on our *W2* `crowdsource` centroids, which have a median value of 515 mas. The *W2* centroid statistical uncertainties are large because of

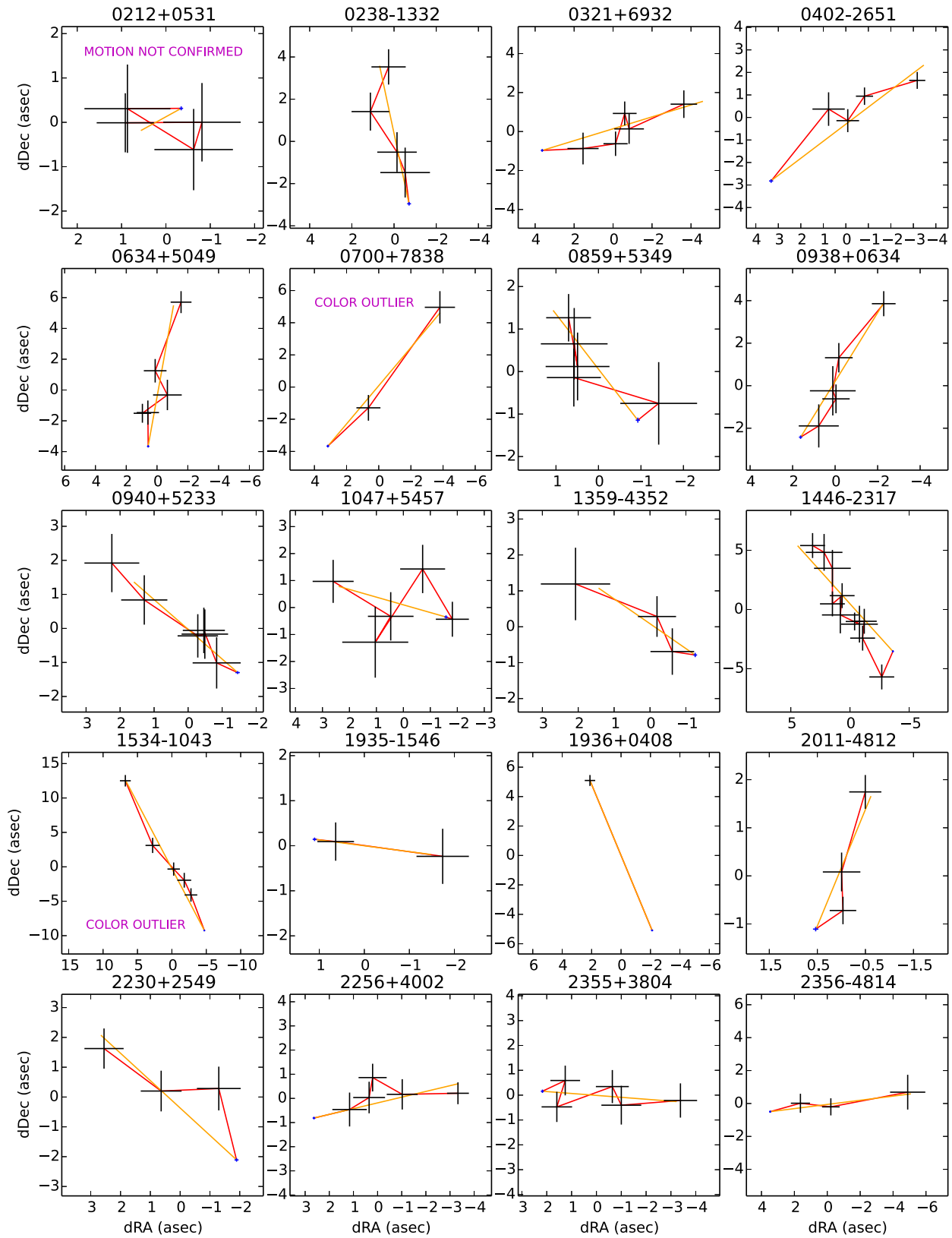


Figure 5. Combined *WISE*+*Spitzer* astrometric trajectories for all 18 of our discoveries with the best-fit $ch1-ch2$ color most consistent with type $\geq Y0$. Except for CWISEP 0212+0531, all of these brown dwarf candidates are motion-confirmed according to our χ^2_{motion} criterion. Also included are two fast-moving ($\mu_{\text{tot}} > 1'' \text{ yr}^{-1}$) targets with unusually large $J - ch2$ colors relative to their $ch1 - ch2$ colors: WISEA 1534+1043 and CWISEP 0700+7838 (see Figure 7). The black plus signs are centered on the *WISE* detections, with line segments extending $\pm 1\sigma$. The much smaller blue plus signs provide the same information for each target's *Spitzer* p14034 astrometric data point. Red lines connect positions adjacent to one another in time. Orange lines show the best-fit linear motion trajectory (Table 7) over the same time period spanned by the combination of *WISE* and *Spitzer* data points.

the broad $W2$ PSF and low S/N of our `crowdsources` $W2$ detections (median S/N = 9.8). Figure 5 provides a visual illustration of the large statistical noise inevitably present in our $W2$ centroids.

Table 3 provides the positions and associated metadata of all $W2$ detections that feed into our final *WISE+Spitzer* linear motion fits. The $\sigma_{\text{R.A.}}$ and $\sigma_{\text{decl.}}$ values quoted each result from summing the statistical centroid uncertainty and bright end scatter systematics floor in quadrature (even though the former strongly dominates over the latter). Here $\sigma_{\text{R.A.}}$ is in angular rather than coordinate units.

8.4. Spitzer Astrometry

Whereas our typical per-coordinate $W2$ centroid precision is larger than 500 mas, we should expect the ch2 per-coordinate centroid precision to be characteristically an order of magnitude smaller. This is simply due to the much higher S/N of our target detections in ch2 (median S/N ≈ 77) than in $W2$ (median S/N ≈ 10) and $\sim 3\times$ narrower ch2 PSF. Because our centroid uncertainties are so much smaller in ch2 than in $W2$, the uncertainties on our eventual *WISE+Spitzer* linear motion measurements will be almost entirely dictated by the $W2$ positional uncertainties. Thus, we need not become fixated on obtaining *Spitzer* astrometry that achieves the ch2 imaging’s theoretically optimal precision floor.

Kirkpatrick et al. (2019a) described a procedure for measuring *Spitzer* ch2 astrometry while achieving a systematics floor of just 10 mas coordinate⁻¹. This entailed a rather involved analysis that proceeded directly from the set of individual *Spitzer* BCD frames contributing to each AOR. On the other hand, Martin et al. (2018) demonstrated that a systematics floor of ~ 20 mas coordinate⁻¹ could be achieved via a substantially more convenient procedure based on astrometric measurements performed on MOPEX mosaics. Because reducing our ch2 systematics floor from ~ 20 to ~ 10 mas would negligibly decrease the uncertainties on our *WISE+Spitzer* linear motions, and we already have MOPEX mosaics/extractions in hand for each target’s field (Section 7), we opt to perform a mosaic-based *Spitzer* astrometric analysis.

Our approach for deriving recalibrated *Spitzer* ch2 astrometric measurements from the p14034 imaging is largely modeled after the procedure laid out in Martin et al. (2018). Our starting point is the list of ch2 MOPEX/APEX pixel coordinate centroids and (R.A., decl.) world coordinate values for all sources in each of our AORs. These are the same MOPEX/APEX catalogs used previously to obtain our ch2 magnitudes for each target in Section 7. The world coordinates natively provided by MOPEX/APEX rely on a WCS solution calibrated to the Two Micron All Sky Survey (2MASS) and typically show offsets of several tenths of a mosaic pixel ($0''.6$ pixel⁻¹) relative to *Gaia*. The systematics inherent in the initial 2MASS WCS solutions are thus much larger than the systematics floor attainable through astrometric recalibration to *Gaia*.

8.4.1. ch2 Astrometric Recalibration

The primary challenge in recalibrating each ch2 mosaic’s astrometry is identifying a sufficient number of *Gaia* DR2 calibration sources (N_{calib}) with high-S/N ch2 counterparts. In selecting astrometric calibrators, we always restrict to the “nonflanking” region of each p14034 ch2 mosaic (the portion

of the mosaic built from single-frame BCD images that contain the brown dwarf candidate’s location). Given our dither strategy, this results in a full frame coverage sky area from which to select *Gaia* calibrators of only 13–15 arcmin², depending on the number of dithers.

Ideally, we would be able to obtain at least 10 *Gaia* DR2 calibrators in each ch2 mosaic’s nonflanking, full-coverage sky region with very high S/N ch2 counterparts (S/N ≥ 100) and *Gaia* proper motions available. However, this was possible for just 67 of our 164 ch2 mosaics (see the first row of Table 6). In cases where this ideal set of calibrator selection criteria (which we refer to as method 1) yielded fewer than 10 calibrators, we tried a sequence of somewhat loosened cuts in order to always obtain at least five *Gaia* calibrators.²⁸ We sequentially tried each set of selection criteria listed in Table 6, in order of ascending “method number” (leftmost column in Table 6), until a set of selection cuts yielded $N_{\text{calib}} \geq N_{\text{calib, min}}$. Method 2 is the same as our ideal set of cuts but reduces the ch2 counterpart S/N threshold to 50. Method 3 further reduces the ch2 S/N threshold to 30 and additionally reduces the minimum required number of *Gaia* calibrators from 10 to five (as specified in the $N_{\text{calib, min}}$ column of Table 6).

Methods 4, 5, and 6 are the same as methods 1, 2, and 3, respectively, but with the requirement of *Gaia* DR2 proper-motion availability dropped (see the Boolean “*Gaia* PM required” column of Table 6). Our inability to correct for calibrator motion between the *Gaia* 2015.5 epoch and our *Spitzer* ch2 epoch a few years later is regrettable but a necessary compromise when resorting to methods 4–6. The typical motions of our *Gaia* DR2 calibrators are very small, so this should have a negligible impact on our final *WISE+Spitzer* linear motion results, and only seven of 164 AORs end up using *Gaia* calibrators lacking proper motions.

Methods 7, 8, and 9 are the same as methods 1, 2, and 3, respectively, but reduce the minimum mosaic BCD frame coverage requirement from full coverage to at least 50% coverage. While this is not ideal, only five of 164 AORs needed to employ this lowered frame coverage requirement.

The “method number” column of Table 4 specifies which set of *Gaia* DR2 calibrator selection criteria was used in determining each row’s recalibrated *Spitzer* ch2 position. The N_{calib} column of Table 4 lists the number of *Gaia* DR2 calibrators employed for each recalibrated ch2 position measurement. The minimum (maximum) number of astrometric calibrators per AOR is five (92). The median (mean) number of astrometric calibrators per AOR is 12 (16). In all cases where our selection criteria demand that *Gaia* DR2 calibrators have proper motions available, we use these proper motions to propagate the *Gaia* calibrator positions to the *Spitzer* ch2 epoch.

Having selected a set of *Gaia* DR2 calibrators for each AOR, we proceed to refit six parameters of each ch2 mosaic’s WCS: all four elements of the CD matrix and the two CRPIX components. The bright end systematics floor achieved via our recalibrated ch2 mosaic WCS solutions is very similar to that of Martin et al. (2018). The median per-mosaic bright end scatter is 25 (23) mas in R.A. (decl.). The 16th–84th percentile ranges are 15–44 mas in R.A. and 14–39 mas in decl. For comparison, Martin et al. (2018) cited a typical systematics floor of ~ 15 –40 mas for their ch2 mosaic WCS recalibration.

²⁸ Five is the minimum number of calibrators used for any field in the *Spitzer* ch2 parallax-fitting astrometric analysis of Kirkpatrick et al. (2019a).

Table 6
Cuts Defining *Spitzer–Gaia* Astrometric Calibrator Samples

Method Number	Min. ch2 S/N	Min. BCD Cov. Frac.	<i>Gaia</i> PM Required	$N_{\text{calib,min}}$	Number of AORs
1	100	1.0	Yes	10	67
2	50	1.0	Yes	10	28
3	30	1.0	Yes	5	57
4	100	1.0	No	10	1
5	50	1.0	No	10	0
6	30	1.0	No	5	6
7	100	0.5	Yes	10	0
8	50	0.5	Yes	10	0
9	30	0.5	Yes	5	5

Table 4 lists the recalibrated ch2 (R.A., decl.) position obtained for each target, including metadata such as the AOR used and the MJD. The uncertainties $\sigma_{\text{R.A.}}$ and $\sigma_{\text{decl.}}$ are computed by summing the per-AOR bright end scatter in quadrature with the statistical uncertainty on each target’s ch2 centroid measurement.

8.5. WISE+*Spitzer* Linear Motion Fits

For each brown dwarf candidate, we gather its combined list of *WISE* and *Spitzer* positions, corresponding MJD values, and positional uncertainties from Tables 3 and 4. The typical combined *WISE+Spitzer* time baseline for targets with p14034 imaging available is ~ 8.6 yr. Along each coordinate direction (R.A. and decl.), we fit a linear model to the combined list of *WISE* and *Spitzer* positions as a function of MJD in order to measure μ_{α} and μ_{δ} . Throughout this paper, the quoted μ_{α} values are in angular rather than coordinate units; i.e., they already have the $\cos(\delta)$ factor multiplied into them. Through these same per-coordinate linear fits, we also obtain parameters α_0 and δ_0 , the object’s (R.A., decl.) coordinates at a fiducial time MJD_0 . This is the inverse variance-weighted mean MJD of the contributing astrometric data points, and it typically ends up being similar to the MJD of the *Spitzer* observation, since the ch2 positional uncertainties are much smaller than those in *W2*. Our linear fits are performed using weighted linear least-squares and so naturally produce uncertainties on the fiducial location and best-fit linear motion components via simple matrix algebra. The measurement uncertainties fed to the weighted linear least-squares routine are the $\sigma_{\text{R.A.}}$ and $\sigma_{\text{decl.}}$ values provided in Tables 3 and 4. No rescaling of the $\sigma_{\text{R.A.}}$, $\sigma_{\text{decl.}}$ positional uncertainties is performed.

We do not allow for any outlier rejection in our per-coordinate linear motion fits. All detections used in our *WISE+Spitzer* motion fits were visually vetted, so there should be no need for outlier rejection.

For our targets that turned out to have two *Spitzer* counterparts (Section 7.2), we performed separate linear motion fits for each *Spitzer* counterpart, where the two motion fits both use the same set of *WISE* detections (since, in such cases, the brown dwarf candidate appears as just a single object in *WISE*).

Table 7 lists our linear motion fit results for all targets. The μ_{α} , σ_{α_0} , and $\sigma_{\mu_{\alpha}}$ values are all in angular rather than coordinate units. The total motion μ_{tot} values are calculated by summing the R.A. and decl. linear motion components in quadrature, and

the quoted μ_{tot} uncertainties are based on first-order propagation of the $\sigma_{\mu_{\alpha}}$, $\sigma_{\mu_{\delta}}$ errors.

Figure 6 shows a histogram that vertically stacks the number of non-motion-confirmed targets (black) on top of the number of motion-confirmed targets (blue). Targets with $\mu_{\text{tot}} > 380 \text{ mas yr}^{-1}$ are always motion-confirmed. The motion-confirmed fraction decreases to 50% at $\mu_{\text{tot}} \approx 265 \text{ mas yr}^{-1}$. The minimum best-fit μ_{tot} of any motion-confirmed member of our sample is 139 mas yr^{-1} . The minimum value of $\mu_{\text{tot}}/\sigma_{\mu_{\text{tot}}}$ for any motion-confirmed target is 4.85, which suggests that, roughly speaking, our $\chi^2_{\text{motion}} = 23.03$ threshold is akin to a requirement of 5σ significant motion. Of our discoveries, 114 are motion-confirmed via the astrometric analysis presented in this work, as indicated in the Boolean “motion-confirmed” column of Table 1.

9. Ground-based Photometry

Although *Spitzer* ch1–ch2 color provides the most efficient means for constraining the spectral types of our brown dwarf candidates, *J*-band photometry can further inform spectral type estimates and represents a crucial step toward ultimately obtaining NIR spectroscopic confirmations. Beyond T5, *J – W2* color increases rapidly toward later spectral types, with the T/Y boundary at *J – W2* ~ 5 mag (Kirkpatrick et al. 2011). For candidates thought to be potential very late T or Y dwarfs, we therefore sought to obtain ground-based *J*-band follow-up to a depth of at least *J* ~ 21 (given that *W2* ≈ 16 is typical for our sample, as discussed in Section 5). Our NIR imaging was not intended to be used for high-fidelity astrometry, and we do not attempt to incorporate ground-based NIR data into our astrometric analyses for several reasons. Among these, the NIR observations generally do not extend our overall time baseline appreciably beyond our *Spitzer* p14034 epoch.

9.1. Gemini/FLAMINGOS-2 Follow-up

For southern targets, we acquired follow-up *J*-band imaging at Gemini South. Through program GS-2019A-Q-316 (PI: C. R. Gelino), we obtained FLAMINGOS-2 (Eikenberry et al. 2006) *J*-band photometry for 16 of the discoveries presented in this paper. The *J*-band photometry from Gemini that we provide is in the MKO photometric system. To calibrate the photometry in each target’s field using 2MASS, we applied the color transformation equation from Hodgkin et al. (2009):

$$J_{\text{MKO}} = J_{2\text{MASS}} - 0.065 \times (J_{2\text{MASS}} - H_{2\text{MASS}}). \quad (3)$$

For each target, we requested a 60 s exposure time per dither with a nine-position dither pattern.

9.2. Palomar Hale/WIRC Follow-up

For northern targets, we obtained follow-up *J*-band imaging with the Wide Field Infrared Camera (WIRC; Wilson et al. 2003) at the Palomar Hale 200 inch telescope (PI: F. Marocco). This WIRC photometry is also in the MKO system, and we again used Equation (3) to photometrically calibrate each field. We obtained WIRC *J*-band photometry for 32 of the discoveries presented in this paper. The total exposure time varied depending on environmental conditions and the anticipated *J*-band magnitude of each target, but 15 dithers at

Table 7
WISE+Spitzer Linear Motion-fitting Results

Name	α_0 (deg, ICRS)	δ_0 (deg, ICRS)	σ_{α_0} (mas)	σ_{δ_0} (mas)	MJD ₀	μ_α (mas yr ⁻¹)	μ_δ (mas yr ⁻¹)	μ_{tot} (mas yr ⁻¹)	χ^2_{motion}	χ^2	No. dof	χ^2_ν
CWISEP J000006.01–704851.2	0.0238910	–70.8144313	42	36	58,656.07	–277 ± 40	–153 ± 38	317 ± 40	63.3	0.08	2	0.04
CWISEP J000110.81–093215.5	0.2954347	–9.5379786	26	27	58,552.36	345 ± 72	–194 ± 73	396 ± 72	30.2	3.34	2	1.67
CWISEP J001146.07–471306.8	2.9424406	–47.2186142	47	58	58,486.49	325 ± 63	–117 ± 63	346 ± 63	30.2	0.29	2	0.15
CWISEP J003507.77–153233.8	8.7825466	–15.5432421	25	32	58,394.44	20 ± 41	–553 ± 41	553 ± 41	181.8	14.45	8	1.81
CWISEP J003915.43+360939.0	9.8140272	36.1605309	27	23	58,577.21	–127 ± 78	–227 ± 79	260 ± 79	10.9	1.75	2	0.87
CWISEP J004158.35+381811.9	10.4937097	38.3033679	35	42	58,437.39	297 ± 51	–8 ± 52	297 ± 51	34.1	0.54	2	0.27
CWISEP J005802.63+723330.3	14.5100692	72.5585540	64	54	58,534.48	–474 ± 61	196 ± 59	513 ± 60	72.1	6.72	2	3.36
CWISEP J010247.48–654226.4	15.6969790	–65.7075044	62	41	58,453.38	–186 ± 85	–35 ± 82	189 ± 85	5.0	1.88	6	0.31
CWISEP J010527.69–783419.3	16.3685566	–78.5724495	48	23	58,280.05	333 ± 21	–180 ± 18	378 ± 21	340.3	22.84	2	11.42
CWISEP J010650.61+225159.1	16.7106177	22.8660649	22	35	58,385.82	–167 ± 34	–278 ± 35	324 ± 35	87.6	13.37	8	1.67
CWISEP J012735.44–564110.5	21.8976927	–56.6862172	27	57	58,455.16	4 ± 40	8 ± 40	9 ± 40	0.1	3.59	2	1.80
CWISEP J012748.35–631056.1	21.9518596	–63.1818606	47	42	58,445.67	660 ± 37	307 ± 35	728 ± 37	392.2	27.96	8	3.49
CWISEP J014607.55–375705.6	26.5324150	–37.9509194	21	21	58,541.43	510 ± 53	384 ± 54	638 ± 53	143.4	1.29	2	0.65
CWISEP J015613.24+325526.6	29.0568626	32.9235107	46	46	58,419.89	1138 ± 84	–373 ± 84	1197 ± 84	204.0	8.55	8	1.07
CWISEP J020103.10+293801.8	30.2636947	29.6333653	34	31	58,456.75	508 ± 67	–235 ± 69	560 ± 67	69.4	1.65	2	0.82
CWISEP J020938.72+180427.7	32.4119873	18.0741597	32	45	58,451.63	487 ± 61	–161 ± 63	513 ± 61	70.0	5.14	8	0.64
CWISEP J021243.55+053147.2	33.1813030	5.5299336	29	30	58,588.49	–102 ± 63	56 ± 65	116 ± 63	3.4	4.05	6	0.67
CWISEP J021921.66–265451.8	34.8407666	–26.9139810	74	73	58,517.37	353 ± 74	484 ± 76	599 ± 76	62.8	5.39	2	2.70
CWISEP J022122.41–564125.0	35.3440503	–56.6902923	24	21	58,454.17	243 ± 43	33 ± 42	245 ± 43	32.3	3.58	2	1.79
CWISEP J022513.27+154854.8	36.3056408	15.8152988	132	81	58,384.82	229 ± 54	85 ± 52	245 ± 54	20.7	4.24	8	0.53
CWISEP J022631.82–203439.4	36.6321750	–20.5783558	70	73	58,362.17	–325 ± 65	–538 ± 65	628 ± 65	92.7	1.99	6	0.33
CWISEP J022935.43+724616.4 N	37.3982422	72.7714650	78	72	55,436.54	–144 ± 28	–145 ± 27	204 ± 28	54.0	43.37	4	10.84
CWISEP J022935.43+724616.4 S	37.3968899	72.7711547	74	67	55,368.95	139 ± 28	75 ± 27	158 ± 28	32.7	13.11	4	3.28
CWISEP J023842.60–133210.7	39.6774081	–13.5375104	61	54	58,569.96	–158 ± 74	–742 ± 76	758 ± 76	100.6	3.11	6	0.52
CWISEP J024204.91–225604.6	40.5224841	–22.9344630	29	31	58,586.09	1049 ± 77	169 ± 79	1062 ± 77	192.6	0.10	2	0.05
CWISEP J024710.25–145809.9	41.7926505	–14.9694556	67	43	58,571.14	–62 ± 88	89 ± 90	108 ± 89	1.5	5.86	2	2.93
CWISEP J024810.75–694127.9	42.0450051	–69.6911310	50	34	58,522.07	7 ± 59	–31 ± 55	32 ± 56	0.3	2.03	2	1.01
CWISEP J025747.92–205602.7	44.4496962	–20.9337098	23	35	58,452.11	55 ± 49	229 ± 50	235 ± 50	21.9	4.74	2	2.37
CWISEP J031130.28+035931.8	47.8768496	3.9924660	61	64	58,450.57	595 ± 105	138 ± 111	611 ± 106	33.4	6.58	2	3.29
CWISEP J031557.05+203552.4	48.9878240	20.5979615	42	39	58,577.83	62 ± 46	82 ± 48	102 ± 48	4.6	4.88	2	2.44
CWISEP J031908.60+081120.4	49.7855761	8.1888656	75	73	58,434.99	–243 ± 102	205 ± 106	318 ± 104	9.4	11.45	2	5.73
CWISEP J031935.50–041231.7	49.8985275	–4.2088561	37	41	58,600.25	519 ± 92	–99 ± 94	528 ± 92	33.2	0.95	2	0.48
CWISEP J032109.59+693204.5	50.2936284	69.5342819	37	40	58,443.81	972 ± 61	–297 ± 63	1016 ± 61	275.2	11.62	8	1.45
CWISEP J034336.27+184025.8	55.9007363	18.6736946	48	49	58,599.52	–61 ± 71	25 ± 74	66 ± 71	0.9	21.63	2	10.82
CWISEP J034514.82+173528.1	56.3120041	17.5909526	28	28	58,606.63	152 ± 52	–148 ± 54	212 ± 53	16.1	0.00	2	0.00
CWISEP J034755.11+123051.9	56.9797369	12.5149653	31	26	58,435.00	20 ± 37	380 ± 38	380 ± 38	98.3	5.27	8	0.66
CWISEP J034904.05–462827.9	57.2673653	–46.4736606	32	35	58,452.20	236 ± 54	494 ± 54	548 ± 54	103.3	2.51	2	1.26
CWISEP J040106.67+085748.5	60.2782164	8.9629526	29	38	58,452.79	357 ± 61	–359 ± 64	507 ± 62	65.9	2.71	8	0.34
CWISEP J040235.55–265145.4	60.6494799	–26.8635386	60	53	58,440.51	755 ± 32	–571 ± 33	947 ± 33	832.5	16.93	6	2.82
CWISEP J040324.67+185729.6	60.8526375	18.9581692	56	41	58,452.93	–98 ± 81	–95 ± 84	137 ± 83	2.7	3.57	2	1.79
CWISEP J040351.00–491605.6	60.9630254	–49.2679072	38	41	58,426.72	256 ± 44	157 ± 45	300 ± 44	46.2	3.65	2	1.82
CWISEP J041025.10+033807.2	62.6046231	3.6352786	33	31	58,627.10	–97 ± 83	–72 ± 87	121 ± 84	2.1	2.39	2	1.19
CWISEP J042455.68+000221.4	66.2322875	0.0392211	43	31	58,589.11	153 ± 39	–70 ± 40	169 ± 39	18.8	2.01	8	0.25
CWISEP J042404.54+665011.2	66.0202303	66.8363662	34	48	58,422.26	395 ± 39	7 ± 41	395 ± 39	104.2	2.19	2	1.10
CWISEP J043034.27+255653.7	67.6433968	25.9481134	31	32	58,559.18	401 ± 27	–197 ± 29	447 ± 27	267.5	0.87	2	0.44
CWISEP J043309.31+100902.9	68.2890654	10.1502782	27	36	58,424.36	174 ± 34	–384 ± 36	422 ± 35	141.9	6.99	8	0.87
CWISEP J044330.73+693828.3	70.8783551	69.6410275	50	46	58,623.07	111 ± 76	–156 ± 79	191 ± 78	6.0	11.28	2	5.64

Table 7
(Continued)

Name	α_0 (deg, ICRS)	δ_0 (deg, ICRS)	σ_{α_0} (mas)	σ_{δ_0} (mas)	MJD ₀	μ_{α} (mas yr ⁻¹)	μ_{δ} (mas yr ⁻¹)	μ_{tot} (mas yr ⁻¹)	χ^2_{motion}	χ^2	No. dof	χ^2_{ν}
CWISEP J044719.61+202158.1	71.8317332	20.3651770	32	29	58,618.86	41 ± 49	-620 ± 52	621 ± 52	144.6	5.47	8	0.68
CWISEP J050521.29-591311.7	76.3403687	-59.2215888	33	33	58,448.04	461 ± 36	-1003 ± 35	1104 ± 36	964.6	7.88	2	3.94
CWISEP J052346.34-545314.7	80.9439898	-54.8868202	42	37	58,455.92	419 ± 49	518 ± 51	667 ± 50	176.7	1.98	2	0.99
CWISEP J053644.82-305539.3	84.1868335	-30.9275925	32	24	58,457.06	46 ± 45	5 ± 46	47 ± 45	1.1	1.93	2	0.97
CWISEP J054233.06+793459.1	85.6379950	79.5831471	36	29	58,540.27	6 ± 58	75 ± 61	75 ± 61	1.5	1.18	2	0.59
CWISEP J055816.68-450233.6	89.5694062	-45.0425330	81	44	58,352.04	-81 ± 39	69 ± 39	106 ± 39	7.4	2.02	8	0.25
CWISEP J060132.96-592227.3	90.3874560	-59.3743566	50	52	56,767.53	-209 ± 20	414 ± 21	464 ± 21	497.4	8.30	6	1.38
CWISEPR J062436.84-071147.2	96.1534148	-7.1962981	39	27	58,446.95	-90 ± 28	106 ± 29	139 ± 28	24.2	6.76	8	0.84
CWISEP J062742.27-215908.1	96.9262310	-21.9860615	30	32	58,501.69	25 ± 58	-376 ± 62	377 ± 62	36.8	0.99	2	0.49
CWISEP J063257.49+274629.4	98.2393490	27.7750194	41	40	58,480.14	14 ± 67	92 ± 71	93 ± 71	1.7	5.16	2	2.58
CWISEP J063428.10+504925.9	98.6173188	50.8225904	38	33	58,487.08	190 ± 61	-1057 ± 64	1074 ± 64	280.6	6.35	8	0.79
CWISEP J063845.48-615937.2	99.6888430	-61.9933801	70	46	58,446.38	-311 ± 67	286 ± 69	423 ± 68	38.8	0.71	2	0.35
CWISEPR J065144.62-115106.1	102.9358948	-11.8519416	27	27	58,511.18	-74 ± 41	-196 ± 43	210 ± 43	23.8	4.86	8	0.61
CWISEP J070055.19+783834.0	105.2368732	78.6417616	46	46	58,482.39	814 ± 96	-966 ± 103	1263 ± 100	160.8	0.81	2	0.41
CWISEP J070214.84-544041.7	105.5618914	-54.6790057	45	47	58,491.25	-83 ± 67	-558 ± 71	564 ± 71	62.8	0.21	2	0.10
CWISEP J071626.02-371951.1	109.1083915	-37.3307807	39	34	58,512.21	37 ± 54	78 ± 58	86 ± 57	2.3	0.20	2	0.10
CWISEP J071813.30-061421.1	109.5559281	-6.2391499	69	68	58,485.30	466 ± 90	141 ± 96	487 ± 91	28.7	0.02	2	0.01
CWISEP J082400.43+075019.9	126.0016447	7.8389405	75	72	58,512.95	-43 ± 123	105 ± 132	113 ± 131	0.8	3.66	4	0.92
CWISEP J084726.55+233558.1	131.8607674	23.5992073	37	36	58,516.78	43 ± 66	-218 ± 71	222 ± 71	9.7	0.02	2	0.01
CWISEP J085348.15+112921.5	133.4506930	11.4891927	33	46	58,500.74	42 ± 47	-131 ± 51	138 ± 51	7.4	4.84	2	2.42
CWISEP J085820.46+500834.4	134.5850031	50.1428221	54	33	58,501.60	-141 ± 63	-27 ± 67	143 ± 63	5.1	0.12	2	0.06
CWISEP J085908.26+152527.1	134.7844045	15.4238600	29	47	58,492.65	-81 ± 40	-263 ± 43	275 ± 43	41.6	2.52	2	1.26
CWISEP J085938.95+534908.7	134.9117592	53.8186842	35	44	58,511.53	-230 ± 53	-298 ± 56	377 ± 55	46.7	5.67	8	0.71
CWISEP J090547.50+700239.8	136.4486544	70.0445205	27	21	58,547.11	196 ± 50	-10 ± 53	197 ± 50	15.3	7.26	2	3.63
CWISEP J090536.35+740009.1	136.4033148	74.0008111	31	48	58,494.02	465 ± 67	-1490 ± 71	1561 ± 70	493.5	0.44	2	0.22
CWISEP J091558.51+254713.2	138.9938542	25.7865366	39	44	58,517.10	120 ± 56	-206 ± 59	238 ± 59	16.6	4.79	6	0.80
CWISEP J093111.03+232502.1	142.7956140	23.4165857	32	33	58,528.96	-295 ± 69	-474 ± 73	558 ± 72	60.0	0.24	2	0.12
CWISEP J093236.66-180029.3	143.1521859	-18.0083844	35	31	58,547.74	-431 ± 56	-182 ± 60	468 ± 57	67.3	0.17	2	0.08
CWISEP J093852.89+063440.6	144.7211265	6.5770243	46	50	58,511.93	453 ± 54	-731 ± 57	860 ± 56	236.1	1.81	8	0.23
CWISEP J094005.50+523359.2	145.0222817	52.5660222	46	24	58,522.22	-343 ± 50	-299 ± 53	455 ± 52	78.1	2.95	10	0.29
CWISEP J094615.56+351434.3	146.5645538	35.2420221	58	51	58,502.54	-229 ± 61	-634 ± 65	674 ± 65	108.9	1.06	2	0.53
CWISEP J094742.83+384619.3	146.9283136	38.7717593	90	50	58,501.73	-135 ± 72	-212 ± 75	251 ± 74	11.6	0.26	2	0.13
CWISEP J094930.41+663937.2	147.3766137	66.6600392	54	45	58,515.07	-5 ± 59	-298 ± 62	298 ± 62	23.5	1.98	2	0.99
CWISEP J094957.15-422017.1	147.4885119	-42.3380471	105	104	58,439.05	261 ± 71	229 ± 74	347 ± 73	22.9	1.16	2	0.58
CWISEP J095930.71-401046.8	149.8781840	-40.1803387	111	110	58,512.73	-131 ± 101	-681 ± 106	693 ± 106	43.2	2.06	4	0.51
CWISEP J100629.01+105408.5	151.6205056	10.9023902	35	30	58,547.59	-259 ± 47	12 ± 49	259 ± 47	30.8	4.05	8	0.51
CWISEP J100854.84+203136.6	152.2283025	20.5265504	37	58	58,515.53	-136 ± 51	-208 ± 55	248 ± 54	21.1	0.37	2	0.18
CWISEP J101841.86+513108.8	154.6745261	51.5193433	41	44	58,531.16	50 ± 68	265 ± 72	270 ± 72	14.1	6.07	2	3.03
CWISEP J102201.27+145520.2	155.5045106	14.9220742	33	41	58,538.06	-537 ± 61	-189 ± 65	569 ± 61	86.8	1.16	8	0.14
CWISEP J103453.14+161228.0	158.7211188	16.2076055	34	62	58,435.26	-235 ± 29	-143 ± 32	275 ± 30	87.2	0.25	2	0.12
CWISEP J103607.94-304253.1	159.0328176	-30.7148463	54	54	58,562.14	-196 ± 78	-116 ± 82	228 ± 79	8.3	5.52	4	1.38
CWISEP J104104.20+221613.6	160.2671291	22.2697391	47	42	58,585.15	-325 ± 111	-467 ± 118	569 ± 115	24.4	1.53	2	0.76
CWISEP J104446.56+001754.9	161.1928198	0.2984562	33	34	58,572.66	-852 ± 85	-160 ± 90	866 ± 85	103.1	3.08	4	0.77
CWISEP J104756.81+545741.6	161.9854882	54.9613395	38	38	58,525.41	-462 ± 72	-132 ± 76	480 ± 73	43.8	8.08	8	1.01
CWISEP J110021.08+094652.9	165.0868452	9.7811543	40	39	58,531.96	-626 ± 47	-40 ± 49	627 ± 47	179.4	1.16	2	0.58
CWISEP J111055.12-174738.2	167.7296340	-17.7944962	64	40	58,410.16	24 ± 28	-395 ± 27	396 ± 27	212.6	9.24	2	4.62
CWISEP J113010.21+313947.3	172.5411784	31.6615769	42	62	58,486.91	-1185 ± 35	-1476 ± 38	1893 ± 37	2684.6	11.72	18	0.65

Table 7
(Continued)

Name	α_0 (deg, ICRS)	δ_0 (deg, ICRS)	σ_{α_0} (mas)	σ_{δ_0} (mas)	MJD ₀	μ_α (mas yr ⁻¹)	μ_δ (mas yr ⁻¹)	μ_{tot} (mas yr ⁻¹)	χ^2_{motion}	χ^2	No. dof	χ^2_{ν}
CWISEP J120444.33−235926.8	181.1843852	−23.9914417	31	31	58,557.19	−263 ± 37	−473 ± 38	542 ± 38	208.2	0.18	2	0.09
CWISEP J121358.13+294237.0	183.4922016	29.7101348	40	39	58,551.73	−189 ± 64	9 ± 68	189 ± 64	8.6	14.08	8	1.76
CWISEP J122010.03+281431.3	185.0412133	28.2417212	32	32	58,576.01	−345 ± 50	−237 ± 52	419 ± 50	69.4	0.34	2	0.17
CWISEP J124138.41−820051.9	190.4111402	−82.0142553	50	45	58,106.00	230 ± 23	65 ± 23	239 ± 23	105.1	9.52	8	1.19
CWISEP J130255.54+191145.9	195.7315475	19.1957537	53	80	58,491.72	95 ± 44	−232 ± 47	251 ± 47	29.0	2.10	2	1.05
CWISEP J131252.97+341746.5	198.2210708	34.2959882	55	49	58,562.62	289 ± 74	−228 ± 78	368 ± 75	24.0	0.20	2	0.10
CWISEP J131208.16−105231.8	198.0338602	−10.8757384	41	52	58,593.28	−49 ± 80	−166 ± 84	173 ± 83	4.3	5.83	2	2.92
CWISEP J131221.97−310845.7	198.0907598	−31.1465777	31	31	58,602.89	−421 ± 48	−312 ± 51	524 ± 49	113.6	1.81	8	0.23
CWISEP J131350.91−440352.2	198.4612845	−44.0647872	38	32	58,592.27	−471 ± 47	−202 ± 50	513 ± 48	116.5	0.45	2	0.23
CWISEP J134143.75+574112.9	205.4323635	57.6866713	30	74	58,492.38	−149 ± 34	−22 ± 38	151 ± 34	19.6	1.75	2	0.87
CWISEP J135336.29−003756.6	208.4012529	−0.6322388	223	238	56,701.39	−653 ± 84	−448 ± 90	792 ± 86	84.6	3.53	6	0.59
CWISEP J135937.65−435226.9	209.9063082	−43.8744784	36	42	58,615.69	−296 ± 72	−205 ± 77	360 ± 74	23.9	1.48	4	0.37
CWISEP J140118.30+432554.2	210.3260378	43.4309089	42	30	58,353.31	−172 ± 33	−659 ± 34	682 ± 34	400.7	3.83	8	0.48
CWISEP J140247.83+102132.6	210.6991320	10.3591566	44	39	58,216.97	−140 ± 17	57 ± 17	151 ± 17	83.5	8.51	8	1.06
CWISEP J141206.85+234412.4	213.0275676	23.7369981	48	34	58,590.72	−625 ± 58	204 ± 61	657 ± 58	126.7	3.67	2	1.84
CWISEP J141400.68+163153.9	213.5031181	16.5321538	60	68	58,524.98	143 ± 51	181 ± 54	231 ± 53	19.2	29.84	2	14.92
CWISEP J142552.36+485151.3	216.4679680	48.8647060	58	60	58,545.20	−141 ± 69	272 ± 72	306 ± 71	18.5	9.42	2	4.71
CWISEP J143439.23−134421.4	218.6627039	−13.7397557	53	46	58,611.75	−473 ± 74	−152 ± 78	497 ± 75	44.4	0.72	2	0.36
CWISEP J144606.62−231717.8	221.5262966	−23.2894624	34	37	58,616.31	−860 ± 69	−954 ± 69	1285 ± 69	342.6	21.41	20	1.07
CWISEP J145837.91+173450.1	224.6573867	17.5806926	32	27	58,554.34	−469 ± 25	215 ± 26	516 ± 25	436.3	4.76	2	2.38
CWISEP J150252.82−304232.8	225.7194826	−30.7092702	25	33	58,380.33	−458 ± 32	−132 ± 34	477 ± 32	222.3	2.05	2	1.02
CWISEP J151140.51−835918.0	227.9188793	−83.9884181	43	40	58,469.21	−35 ± 69	−125 ± 73	130 ± 73	3.2	4.08	6	0.68
CWISEP J151521.22−215736.9	228.8385873	−21.9601747	165	175	56,794.73	255 ± 66	−429 ± 70	499 ± 69	52.3	6.33	6	1.05
WISEA J153429.75−104303.3	233.6209262	−10.7235637	27	29	58,634.28	−1254 ± 65	−2387 ± 69	2697 ± 68	1565.8	5.08	8	0.63
CWISEP J153859.39+482659.1	234.7478251	48.4490749	44	52	58,296.88	98 ± 32	−450 ± 34	461 ± 34	184.2	0.52	2	0.26
CWISEP J154151.59+523025.0 N	235.4656234	52.5068123	55	80	58,291.34	409 ± 28	−48 ± 31	412 ± 28	216.9	17.12	8	2.14
CWISEP J154151.59+523025.0 S	235.4645297	52.5062999	57	82	58,266.45	−14 ± 28	−374 ± 31	374 ± 31	148.2	54.35	8	6.79
CWISEP J160311.60−104620.4	240.7991406	−10.7735237	30	26	58,454.23	547 ± 52	−740 ± 55	920 ± 54	288.2	1.27	2	0.63
CWISEP J160835.01−244244.7	242.1462779	−24.7125120	33	26	58,406.40	290 ± 37	−71 ± 39	299 ± 37	64.6	1.52	8	0.19
CWISEP J161822.86−062310.2	244.5952072	−6.3863681	26	31	58,453.28	303 ± 51	−201 ± 54	364 ± 52	48.5	8.53	6	1.42
CWISEP J162225.92+370118.8	245.6073116	37.0213231	38	46	58,425.10	−361 ± 46	−473 ± 49	595 ± 48	154.2	5.38	8	0.67
CWISEP J163200.11+002108.6	248.0005765	0.3525295	47	46	58,454.71	−31 ± 90	252 ± 95	254 ± 95	7.1	4.97	2	2.49
CWISEP J165215.62+022918.5	253.0656696	2.4885946	58	57	58,442.79	406 ± 82	145 ± 87	432 ± 83	27.2	0.24	2	0.12
CWISEP J165359.67+214457.2	253.4987525	21.7488879	40	33	58,640.88	60 ± 69	−221 ± 72	229 ± 72	10.1	1.35	2	0.68
CWISEP J170918.83+000950.5	257.3283154	0.1643273	27	27	58,656.23	−102 ± 55	175 ± 58	202 ± 57	12.5	1.37	2	0.68
CWISEP J172104.42+595047.7	260.2683795	59.8466722	58	40	53,261.59	−10 ± 16	−32 ± 17	33 ± 17	4.0	1.43	2	0.72
CWISEP J175746.31+195112.6	269.4428220	19.8535267	33	32	58,459.19	39 ± 72	27 ± 76	47 ± 73	0.4	3.20	2	1.60
CWISEP J182358.73−740246.0	275.9965126	−74.0463976	55	52	58,383.86	371 ± 58	−309 ± 60	483 ± 59	67.3	0.69	2	0.34
CWISEP J185658.80+601351.4	284.2443326	60.2296897	30	35	58,474.24	−228 ± 28	−776 ± 27	809 ± 27	872.4	5.98	8	0.75
CWISEP J193518.58−154620.3	293.8277840	−15.7723504	29	25	58,482.28	305 ± 61	40 ± 64	308 ± 61	25.5	1.25	2	0.63
WISENF J193656.08+040801.2	294.2323616	4.1312231	31	20	58,507.54	−479 ± 36	−1155 ± 37	1250 ± 37	1130.2	...	0	...
CWISEP J194027.48−345650.6	295.1144888	−34.9475130	48	47	58,481.29	−19 ± 108	−168 ± 114	169 ± 114	2.2	5.31	2	2.66
CWISEP J194101.59+542335.9	295.2567040	54.3930038	30	33	58,348.47	8 ± 22	−214 ± 22	215 ± 22	92.0	3.58	8	0.45
CWISEP J194812.42−322334.9	297.0512077	−32.3929568	42	27	58,480.41	−368 ± 67	2 ± 70	368 ± 67	29.9	1.67	2	0.84
CWISEP J201146.45−481259.7	302.9439641	−48.2169094	42	33	58,439.13	134 ± 35	−324 ± 36	350 ± 36	94.6	2.37	4	0.59
CWISEP J201510.68−675005.6	303.7940891	−67.8350564	30	35	58,309.55	−62 ± 20	−194 ± 21	204 ± 21	91.7	1.73	2	0.86
CWISEP J203821.53−064930.9	309.5894424	−6.8257801	37	25	58,498.59	−201 ± 68	−401 ± 71	448 ± 70	40.6	0.97	2	0.49

Table 7
(Continued)

Name	α_0 (deg, ICRS)	δ_0 (deg, ICRS)	σ_{α_0} (mas)	σ_{δ_0} (mas)	MJD ₀	μ_α (mas yr ⁻¹)	μ_δ (mas yr ⁻¹)	μ_{tot} (mas yr ⁻¹)	χ^2_{motion}	χ^2	No. dof	χ^2_ν
CWISEP J205019.99–253652.8	312.5830506	–25.6149376	26	36	58,461.39	–182 ± 32	–276 ± 34	330 ± 34	96.5	4.49	8	0.56
CWISEP J205908.95+024105.6	314.7886251	2.6841705	30	30	58,527.32	658 ± 48	–513 ± 49	834 ± 49	294.0	4.55	2	2.28
CWISEP J210007.87–293139.8	315.0334875	–29.5278805	37	38	58,493.21	372 ± 71	–128 ± 74	394 ± 72	30.3	0.23	2	0.11
CWISEP J211909.29–192117.4	319.7890460	–19.3548643	31	26	58,509.55	160 ± 82	–50 ± 84	168 ± 82	4.2	1.98	2	0.99
CWISEP J212828.05+352912.4	322.1167327	35.4863939	74	74	58,377.15	–290 ± 83	–299 ± 84	416 ± 84	24.8	7.89	2	3.95
CWISEP J213249.05+690113.7	323.2051650	69.0207454	50	42	58,158.47	244 ± 24	159 ± 22	291 ± 23	157.2	1.56	2	0.78
CWISEP J213838.74–313808.5	324.6622036	–31.6361072	22	35	58,481.77	542 ± 34	–325 ± 35	632 ± 34	336.9	0.63	8	0.08
CWISEP J213930.45+042721.6	324.8770200	4.4553757	25	22	58,524.32	162 ± 67	–465 ± 69	493 ± 68	51.8	1.79	2	0.90
CWISEP J215841.50+732842.7	329.6733966	73.4785142	89	29	58,200.99	162 ± 23	–32 ± 18	165 ± 23	52.0	10.01	8	1.25
CWISEP J220452.02+063343.4	331.2163311	6.5618894	63	44	58,524.83	–299 ± 83	–223 ± 85	373 ± 84	19.8	6.60	2	3.30
CWISEP J221736.94–222647.6	334.4039704	–22.4465251	49	38	58,510.64	82 ± 89	121 ± 90	146 ± 90	2.7	4.50	2	2.25
CWISEP J222035.35–810322.6	335.1488953	–81.0565232	51	43	58,383.55	262 ± 50	–226 ± 49	346 ± 50	48.5	0.67	2	0.33
CWISEP J223022.60+254907.5	337.5932596	25.8180721	47	38	58,527.52	–535 ± 68	–491 ± 69	726 ± 68	113.4	5.55	4	1.39
CWISEP J223138.55–383057.2	337.9114974	–38.5164936	35	28	58,513.68	441 ± 72	–433 ± 74	618 ± 73	72.6	2.18	2	1.09
CWISEP J224747.42–004103.6	341.9474932	–0.6842782	57	64	56,336.39	34 ± 116	378 ± 117	380 ± 117	10.5	23.44	2	11.72
CWISEP J224916.17+371551.4	342.3170746	37.2637442	32	31	58,545.41	–203 ± 84	–361 ± 85	414 ± 84	24.0	0.31	2	0.16
CWISEP J225059.28–432057.2	342.7475126	–43.3497456	38	73	58,503.31	225 ± 75	–434 ± 77	489 ± 76	40.9	0.73	2	0.36
CWISEP J225156.13+392408.4	342.9833992	39.4022511	25	29	58,399.63	–310 ± 48	–113 ± 48	330 ± 48	48.0	0.79	2	0.40
CWISEP J225109.50–074037.7	342.7905094	–7.6769274	40	36	58,493.01	696 ± 41	163 ± 41	715 ± 41	305.7	10.48	8	1.31
CWISEP J225511.56–191516.3	343.7980417	–19.2551834	130	130	58,505.94	–166 ± 186	–314 ± 190	355 ± 189	3.5	20.39	2	10.19
CWISEP J225628.97+400227.3	344.1221247	40.0407842	29	29	58,535.53	696 ± 43	–165 ± 43	716 ± 43	278.4	5.26	8	0.66
CWISEP J230158.30–645858.3	345.4933541	–64.9835116	34	21	58,442.51	107 ± 30	–441 ± 29	453 ± 29	246.9	24.25	18	1.35
CWISEP J231047.80+362004.6	347.6996243	36.3347544	37	34	58,563.06	286 ± 86	37 ± 87	288 ± 86	11.2	12.91	2	6.45
CWISEP J231114.50+135148.5	347.8100199	13.8635280	32	48	58,536.94	–295 ± 63	17 ± 64	296 ± 63	22.1	1.97	2	0.98
CWISEP J233216.39–290025.0	353.0683272	–29.0073009	29	22	58,532.57	72 ± 65	–360 ± 66	367 ± 66	31.3	1.53	2	0.76
CWISEP J235130.42–185800.2	357.8775955	–18.9668268	40	28	58,394.73	492 ± 47	–46 ± 48	494 ± 47	111.2	0.17	2	0.09
CWISEP J235547.99+380438.9	358.9511591	38.0775517	38	41	58,395.29	666 ± 64	51 ± 65	668 ± 64	108.7	6.49	8	0.81
CWISEP J235644.78–481456.3	359.1881598	–48.2492296	30	30	58,403.37	1048 ± 91	–133 ± 90	1056 ± 91	133.4	0.49	4	0.12

Note. χ^2_ν is the reduced χ^2 of the linear motion fit, defined as $\chi^2_\nu = \chi^2/(\text{no. of dof})$.

(This table is available in machine-readable form.)

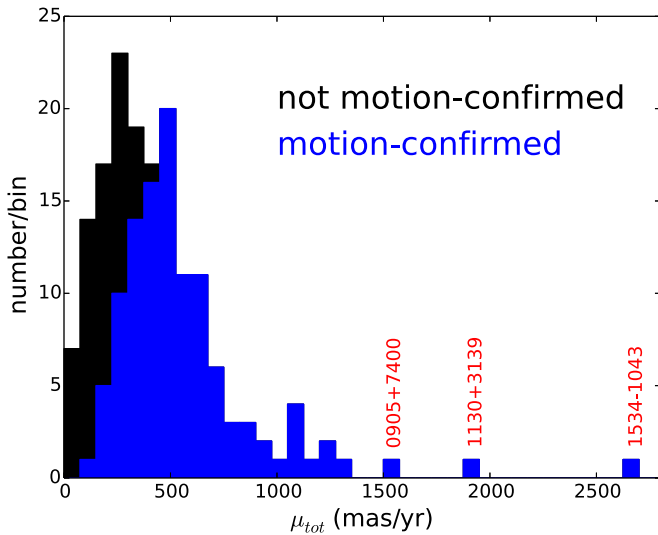


Figure 6. Histogram of total motion measurements resulting from our sample’s linear motion fits (Section 8.5). The number of targets per bin that we could not motion-confirm is shown in black, stacked on top of the number of motion-confirmed targets per bin (blue). We exclude the six spurious candidates (Table 2), four CPM objects, and two targets that each have two *Spitzer* counterparts (Section 7.2). Three of our motion-confirmed discoveries have best-fit $\mu_{\text{tot}} > 1500 \text{ mas yr}^{-1}$, and 12 have $\mu_{\text{tot}} > 1000 \text{ mas yr}^{-1}$.

2 minutes per dither represents a typical observing sequence for one object.

9.3. Archival NIR Photometry

9.3.1. 2MASS

By selection, we expect very few of our targets to have 2MASS counterparts. Nevertheless, we checked our entire sample for 2MASS counterparts. We used our best-fit *WISE*+*Spitzer* proper motions from Table 7 to predict each target’s (R.A., decl.) at a fiducial 2MASS epoch of year = 1999.5, then visually inspected the 2MASS images to look for a counterpart at that location. In all, we only found 2MASS counterparts²⁹ to two discoveries in our sample: CWISEP 1402+1021 and CWISEP 2015–6750. Both of these are relatively bright/blue members of our sample, selected specifically because we expected they may be mid-T brown dwarfs potentially within a distance of 20 pc. Both 2MASS counterparts are detected only in $J_{2\text{MASS}}$, and in both cases, the $J_{2\text{MASS}}$ magnitude is in good agreement with that predicted based on ch2 magnitude and *Spitzer* phototype. Table 8 lists the two 2MASS counterparts recovered. The magnitude limits in Table 8 are based on 95% confidence flux upper limits.

9.3.2. UKIRT/WFCAM and VISTA/VIRCAM

We searched the entire WFCAM Science Archive (WSA) and VISTA Science Archive (VSA) for JHK/K_S counterparts to our brown dwarf candidates. Specifically, we searched all “pawprint” exposure sets³⁰ through 2017 January 1 in VSA and 2014 March 7 in WSA.³¹ We queried for counterparts within a

²⁹ In both cases, the 2MASS counterpart is drawn from the point-source reject table.

³⁰ <http://www.vista.ac.uk/glossary.htm#pawprint>

³¹ Public availability of data in VSA/WSA becomes a relatively complex issue at later dates.

Table 8
2MASS Counterparts

Name	2MASS Desig.	$J_{2\text{MASS}}$	$H_{2\text{MASS}}$	$K_{S,2\text{MASS}}$
CWISEP J140247.83	2MASS J14024796	16.443 ± 0.139	>15.692	>16.369
+102132.6	+1021318			
CWISEP J201510.68	2MASS J20151069	17.027 ± 0.181	>16.731	>16.374
–675005.6	–6750029			

5” radius of a nominal epoch ~ 2014 position for each target, based on our linear motion solutions. We retrieved all matched VSA/WSA detections within this relatively large 5” radius, allowing us to perform more detailed disambiguation downstream. Further, when possible, we retrieved available 5σ magnitude limits in cases where no matches were found within a 5” radius yet archival VSA/WSA imaging at the target location exists.

In total, we retrieved ~ 1100 VSA/WSA matched detections or magnitude limits in JHK/K_S . These were drawn predominantly from the UKIRT Hemisphere Survey (UHS; Dye et al. 2018) and VISTA Hemisphere Survey (VHS; McMahon et al. 2013) but also incorporate contributions from a variety of other smaller-area surveys, including ULAS (Lawrence et al. 2007), VIKING (Edge et al. 2013), and a few PI programs. In many cases, a single brown dwarf candidate has multiple VSA/WSA detections/limits in one NIR band.

We therefore sought to condense/vet our raw VSA/WSA query results and thereby compose a summary consisting of at most one VSA or WSA magnitude or magnitude limit per NIR band per target. To do so, we used the linear motion solutions from Table 7 to predict the moving target’s position at each VSA/WSA pawprint MJD. We then retained only matches within $1''.5$ of each predicted position. In cases where a single target has multiple matched detections within $1''.5$ in a single band, we adopt the magnitude of the closest match. When a target has no counterparts in a given band within $1''.5$, we quote a magnitude limit in that band if one is available. In cases where there is no counterpart but multiple limits, we adopt the deepest limit. We also enforced a veto list containing a small handful of VSA/WSA detections that were noted to be static contaminants (wrong cross-matches) based on visual inspection of the VIRCAM/WFCAM imaging. We additionally discarded all VSA/WSA detections with nonzero PERRBITS data quality flags³² and/or an extended morphological classification (CLASS = 1), so as to avoid artifacts and incorrectly matched galaxies.

Photometry from WFCAM JHK and VIRCAM JH is in the MKO system, whereas VIRCAM employs a K_S filter.

9.3.3. Merging Archival and Follow-up NIR Photometry

In order to produce color–color diagrams such as those of Figures 7 and 8, we seek to merge our Palomar, Gemini, WFCAM, VIRCAM, and 2MASS NIR photometry into a single compilation with at most one magnitude or magnitude limit per NIR band per target. In doing so, we always give precedence to our dedicated CatWISE follow-up over archival information in the J band when both options are available. In one isolated instance, we have archival photometry available

³² <http://wsa.roe.ac.uk/ppErrBits.html>

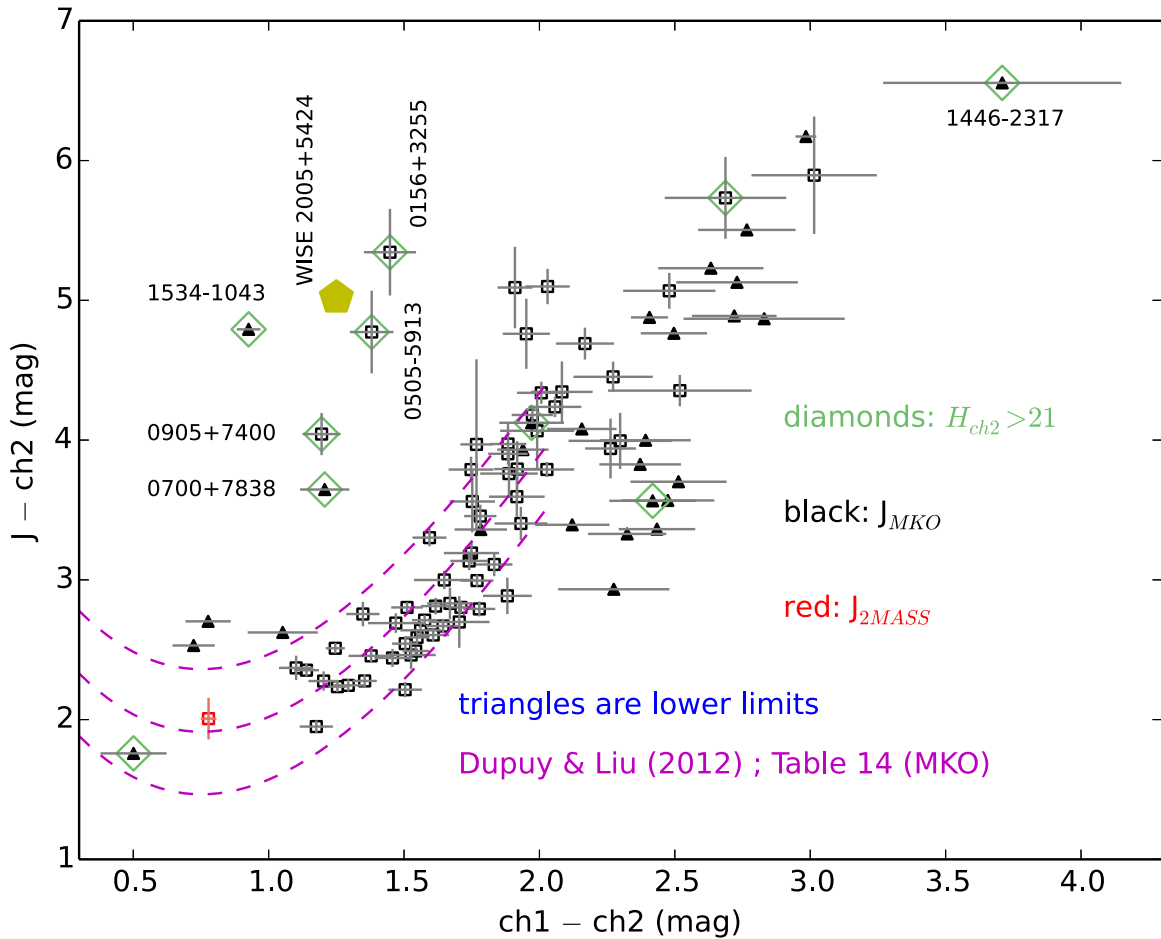


Figure 7. Shown is $J - \text{ch2}$ vs. $\text{ch1} - \text{ch2}$ for motion-confirmed discoveries with *Spitzer* photometry available. The J -band photometry is drawn from our Gemini/FLAMINGOS-2 and Palomar/WIRC follow-up, the WFCAM and VISTA archives, and 2MASS. The purple dashed lines trace the expected trend for late-type brown dwarfs from Dupuy & Liu (2012), plus/minus the scatter in the relevant relations from their Table 14. Our motion-confirmed brown dwarf candidates largely follow this trend while continuing (as expected) to become even redder in $J - \text{ch2}$ beyond T9, where the Dupuy & Liu (2012) relations are not intended to be applicable. Light green diamonds indicate targets with exceptionally large reduced proper motion, $H_{\text{ch2}} > 21$ mag. Five targets (each specially labeled with its short name) are anomalously red in $J - \text{ch2}$ relative to their $\text{ch1} - \text{ch2}$ colors, inhabiting a region of parameter space with $J - \text{ch2} > 3.5$ and $\text{ch1} - \text{ch2} < 1.5$. All five of these major color outliers have $H_{\text{ch2}} > 21$, suggesting that they may represent a low-metallicity subpopulation. Color limits are based on 5σ J -band flux limits. The yellow pentagon denotes the location of the benchmark T8 subdwarf WISE 2005+5424 within this color-color space.

from both VISTA and 2MASS while lacking CatWISE follow-up: the J band for CWISEP 2015–6750. In this case, we adopt the much higher S/N measurement from VISTA. Table 9 provides the merged compilation of VSA/WSA and follow-up JHK/K_S magnitudes and limits for motion-confirmed discoveries with at least one such NIR magnitude or limit available. The 2MASS photometry is listed separately in Table 8. All limits quoted in Table 9 are 5σ . Finally, Table 10 lists our Palomar and Gemini J -band follow-up for sources that were not motion-confirmed by our astrometric analysis.

10. Discussion

10.1. Photometric Spectral Type Estimates

Obtaining photometric spectral type estimates was the primary motivation for conducting our *Spitzer* p14034 follow-up campaign. We use the $\text{ch1} - \text{ch2}$ colors from Table 1 to estimate spectral types. We do not attempt to fold NIR magnitudes/limits into our phototyping in this work. For our spectral type estimates, we use a type versus $\text{ch1} - \text{ch2}$ color

grid constructed from the Kirkpatrick et al. (2019a) relation for T5.5-Y1 and Kirkpatrick et al. (2011) for T0–T5. These grids are quantized at the level of 0.5 type. Quoted spectral type estimates result from evaluating these type versus $\text{ch1} - \text{ch2}$ grids at the best-fit (i.e., central) $\text{ch1} - \text{ch2}$ color from Table 1. Our photometric type estimates do not extend colder than Y1 due to the scarcity of empirical data in this regime, and as a result, objects with best-fit phototypes of Y1 are listed as $\geq Y1$ in Tables 11 and 12. Table 11 presents a number of derived properties for each of our motion-confirmed discoveries, including our spectral type estimates in a column labeled “SpT” for short.

Figure 9 shows a histogram of our measured $\text{ch1} - \text{ch2}$ colors for motion-confirmed brown dwarf candidates. The median $\text{ch1} - \text{ch2}$ color within our motion-confirmed sample is 1.75 mag, corresponding to a spectral type of approximately T8. Here CWISEP 0959–4010 has the bluest $\text{ch1} - \text{ch2}$ color of any motion-confirmed target in our sample, $\text{ch1} - \text{ch2} = 0.50 \pm 0.12$ mag, for which we obtain a spectral type estimate of T3.5. The reddest best-fit $\text{ch1} - \text{ch2}$ color of any motion-confirmed target in

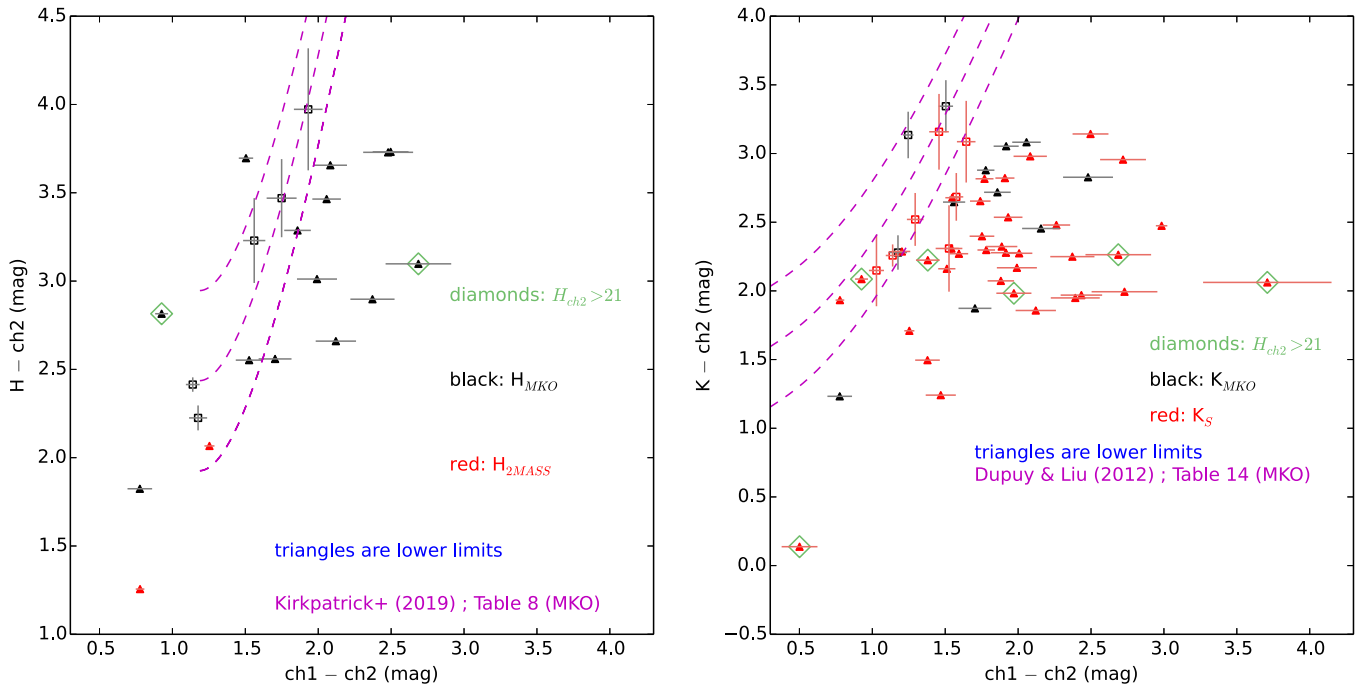


Figure 8. Same as Figure 7 but for $H - ch2$ (left) and $K - ch2$ (right). Relative to J , there are far fewer targets with available data at H and K , in part reflecting the availability of VISTA/UKIRT archival observations but also because our NIR imaging follow-up campaigns at Gemini and Palomar only employ the J band. The limited number of detections follow the literature trends reasonably well. In each panel, the CWISEP 1402+1021 and CWISEP 2015–6750 color lower limits are based on 95% confidence flux upper limits from 2MASS. All other color lower limits are based on 5σ flux upper limits.

our sample is 3.71 ± 0.44 mag for CWISEP 1446–2317, which has its reported spectral type estimate listed as $\geq Y1$.

We caution against overinterpretation of our spectral type estimates on an object-by-object basis, since we regard these as considerably uncertain for a number of reasons. The Kirkpatrick et al. (2019a) tabulation of $ch1 - ch2$ versus spectral type does not provide a direct formula for spectral type as a function of $ch1 - ch2$ color or a prescription for quoting uncertainties on spectral type estimates inferred from *Spitzer* color. Additionally, spectral typing becomes relatively poorly defined at types $\gtrsim Y1$ due to a number of factors, including small sample size, lack of NIR spectroscopic data (e.g., WISE 0855–0714, WD 0806–661 B; Luhman et al. 2011), and difficulty fitting all examples into a common sequence of spectral morphology (see WISE 1828+2650; Beichman et al. 2013; Leggett et al. 2013).

Although these considerations lead us not to quote per-target spectral type errors, we can still use the Kirkpatrick et al. (2019a) compilation of spectral types and $ch1 - ch2$ colors to provide an overall sense of the level of uncertainty on our type estimates. We fit a second-order polynomial to the ($ch1 - ch2$, spectral type) pairs with $0.9 \leq ch1 - ch2 \leq 3.0$ in the bottom middle panel of Kirkpatrick et al. (2019a) Figure 4, using $ch1 - ch2$ as the independent variable. The residuals relative to the best fit show an rms scatter of ± 0.56 in spectral type. As a result of the p14034 observing strategy, our $ch1 - ch2$ color uncertainties ramp up from ~ 0.06 mag for $ch1 - ch2 < 1.2$ to ~ 0.2 mag at type $\sim Y1$. Propagating this color uncertainty through our best-fit polynomial relation for spectral type, this translates into a scatter of ~ 0.15 (~ 0.65) in type at mid-T (Y1). Adding the worst-case 0.65 type scatter in quadrature with that of the type versus $ch1 - ch2$ polynomial residuals and that from our 0.5 type quantization yields an overall error bar of roughly 1.0 in spectral type for our reported estimates.

We emphasize that it is not actually possible to measure a spectral type with the data at hand; our $ch1 - ch2$ colors are measured in a totally different wavelength regime than that in which the spectral type is defined (at the J and H bands), so we can only provide our best estimate as to NIR type based on its known correlation with *Spitzer* color. True spectral types can only be measured using spectra in the wavelength range of interest. In the absence of observationally prohibitive spectroscopic confirmations, spectral type estimation for our coldest motion-confirmed discoveries would greatly benefit from further astrometric follow-up in the future, with trigonometric distances yielding critical $ch2$ absolute magnitude estimates.

10.2. Photometric Absolute Magnitude and Distance Estimates

We use the Kirkpatrick et al. (2019a; Table 8) $ch1 - ch2$ to M_{ch2} relation to obtain photometric absolute magnitude estimates, which in turn yield corresponding photometric distance estimates. These derived properties for our motion-confirmed targets are presented in Table 11. When calculating uncertainties on these absolute magnitude estimates, we take into account both our 1σ $ch1 - ch2$ color uncertainties and the 0.3 mag residual scatter of the $M_{ch2}(ch1 - ch2)$ polynomial fit relative to its training data.

The Kirkpatrick et al. (2019a) $M_{ch2}(ch1 - ch2)$ relation is only valid for $0.9 \leq ch1 - ch2 \leq 3.7$. However, a handful of our motion-confirmed discoveries have $ch1 - ch2 < 0.9$ mag, and in these cases, we obtain M_{ch2} estimates by plugging our spectral type estimates from Table 11 into the Dupuy & Liu (2012; Table 14) $M_{ch2}(SpT)$ relation, which is applicable in the relevant early-to-mid-T regime.

Our only discovery with best-fit $ch1 - ch2$ color too red for the Kirkpatrick et al. (2019a) $M_{ch2}(ch1 - ch2)$ relation is CWISEP 1446–2317. In this case, we quote only a lower limit of $M_{ch2} > 16.23$. This limit is derived by applying the

Table 9
NIR Photometry from Gemini, Palomar, UKIRT, and VISTA for Motion-confirmed Targets

Name	J_{MKO} (mag)	Origin of J_{MKO}	H_{MKO} (mag)	Origin of H_{MKO}	K_{MKO} (mag)	Origin of K_{MKO}	K_S (mag)	Origin of K_S
CWISEP J000006.01–704851.2	18.28 ± 0.05	VIRCAM	18.99 ± 0.27	VIRCAM
CWISEP J001146.07–471306.8	19.22 ± 0.11	VIRCAM	19.79 ± 0.34	VIRCAM	>18.35	VIRCAM
CWISEP J003507.77–153233.8	19.13 ± 0.03	WIRC
CWISEP J004158.35+381811.9	19.26 ± 0.07	WIRC	19.54 ± 0.22	WFCAM
CWISEP J010650.61+225159.1	17.41 ± 0.03	WFCAM
CWISEP J012748.35–631056.1	17.82 ± 0.03	VIRCAM	18.10 ± 0.19	VIRCAM
CWISEP J015613.24+325526.6	21.46 ± 0.30	WIRC
CWISEP J020103.10+293801.8	17.91 ± 0.03	WFCAM	18.19 ± 0.06	WFCAM	18.24 ± 0.12	WFCAM
CWISEP J020938.72+180427.7	>19.50	WFCAM
CWISEP J022122.41–564125.0	18.78 ± 0.05	VIRCAM	>18.30	VIRCAM
CWISEP J023842.60–133210.7	>21.46	WIRC	>18.32	VIRCAM
CWISEP J024204.91–225604.6	>20.56	VIRCAM	>18.41	VIRCAM
CWISEP J031130.28+035931.8	>19.74	WFCAM	>18.86	WFCAM	>18.27	WFCAM
CWISEP J031935.50–041231.7	20.54 ± 0.19	WIRC
CWISEP J032109.59+693204.5	>21.16	WIRC
CWISEP J034755.11+123051.9	17.96 ± 0.05	WFCAM
CWISEP J034904.05–462827.9	18.77 ± 0.09	VIRCAM	>18.86	VIRCAM	18.61 ± 0.31	VIRCAM
CWISEP J040106.67+085748.5	19.47 ± 0.19	WFCAM	>18.73	WFCAM
CWISEP J040235.55–265145.4	>20.34	VIRCAM	>18.41	VIRCAM
CWISEP J040351.00–491605.6	20.19 ± 0.26	VIRCAM	>19.14	VIRCAM	>18.30	VIRCAM
CWISEP J042404.54+665011.2	19.45 ± 0.08	WIRC
CWISEP J043034.27+255653.7	17.30 ± 0.02	WFCAM	17.92 ± 0.16	WFCAM
CWISEP J043309.31+100902.9	17.94 ± 0.04	WFCAM	>18.03	WFCAM
CWISEP J044719.61+202158.1	>19.82	WFCAM	>18.20	WFCAM
CWISEP J050521.29–591311.7	20.93 ± 0.29	VIRCAM	>18.38	VIRCAM
CWISEP J052346.34–545314.7	>20.01	VIRCAM	>19.08	VIRCAM	>18.43	VIRCAM
CWISEPR J062436.84 –071147.2	18.61 ± 0.05	WIRC	>17.58	VIRCAM
CWISEP J063428.10+504925.9	>19.52	WFCAM
CWISEP J063845.48–615937.2	19.30 ± 0.05	FLAMINGOS-2	>17.85	VIRCAM
CWISEPR J065144.62 –115106.1	18.20 ± 0.02	WIRC	>17.56	VIRCAM
CWISEP J070055.19+783834.0	>20.36	WIRC
CWISEP J070214.84–544041.7	19.54 ± 0.05	FLAMINGOS-2
CWISEP J085908.26+152527.1	19.20 ± 0.14	WFCAM
CWISEP J085938.95+534908.7	>19.70	WFCAM
CWISEP J090536.35+740009.1	20.45 ± 0.14	WIRC
CWISEP J093111.03+232502.1	18.53 ± 0.10	WFCAM
CWISEP J093236.66–180029.3	20.04 ± 0.07	FLAMINGOS-2	>17.98	VIRCAM
CWISEP J093852.89+063440.6	21.03 ± 0.12 ^a	FLAMINGOS-2	>19.69	WFCAM	>18.79	WFCAM
CWISEP J094005.50+523359.2	>21.26	WIRC
CWISEP J094615.56+351434.3	18.45 ± 0.07	WFCAM
CWISEP J095930.71–401046.8	>19.49	VIRCAM	>17.87	VIRCAM
CWISEP J100629.01+105408.5	19.80 ± 0.06	FLAMINGOS-2	>19.02	WFCAM	>18.64	WFCAM
CWISEP J102201.27+145520.2	>19.76	WFCAM
CWISEP J103453.14+161228.0	17.68 ± 0.03	WFCAM
CWISEP J104104.20+221613.6	>19.58	WFCAM
CWISEP J104446.56+001754.9	20.34 ± 0.21	VIRCAM	>19.65	VIRCAM	>18.97	VIRCAM
CWISEP J104756.81+545741.6	>19.83	WFCAM
CWISEP J110021.08+094652.9	>18.91	WFCAM	>18.34	WFCAM
CWISEP J111055.12–174738.2	17.75 ± 0.02	WIRC	17.72 ± 0.17	VIRCAM
CWISEP J120444.33–235926.8	17.90 ± 0.03	VIRCAM
CWISEP J122010.03+281431.3	18.50 ± 0.03	WIRC	19.09 ± 0.23	WFCAM	>18.51	WFCAM
CWISEP J124138.41–820051.9	20.44 ± 0.12	FLAMINGOS-2
CWISEP J131252.97+341746.5	19.09 ± 0.17	WFCAM	>18.95	WFCAM	>18.27	WFCAM
CWISEP J131221.97–310845.7	18.70 ± 0.12	VIRCAM	>17.88	VIRCAM
CWISEP J131350.91–440352.2	18.27 ± 0.04	VIRCAM	18.68 ± 0.29	VIRCAM
CWISEP J135336.29–003756.6	19.97 ± 0.06	FLAMINGOS-2	>19.45	WFCAM	>18.94	VIRCAM
CWISEP J135937.65–435226.9	>19.31	VIRCAM	>17.91	VIRCAM
CWISEP J140118.30+432554.2	18.40 ± 0.08	WFCAM
CWISEP J143439.23–134421.4	>19.54	VIRCAM	>18.81	VIRCAM	>18.01	VIRCAM
CWISEP J144606.62–231717.8	>22.36	FLAMINGOS-2	>17.86	VIRCAM
CWISEP J145837.91+173450.1	18.39 ± 0.07	WFCAM

Table 9
(Continued)

Name	J_{MKO} (mag)	Origin of J_{MKO}	H_{MKO} (mag)	Origin of H_{MKO}	K_{MKO} (mag)	Origin of K_{MKO}	K_S (mag)	Origin of K_S
CWISEP J150252.82–304232.8	17.62 ± 0.03	VIRCAM	>17.71	VIRCAM
CWISEP J151521.22–215736.9	17.48 ± 0.03	VIRCAM	18.52 ± 0.38	VIRCAM
WISEA J153429.75–104303.3	>20.56	WIRC	>18.58	VIRCAM	>17.85	VIRCAM
CWISEP J153859.39+482659.1	20.26 ± 0.10	WIRC
CWISEP J160311.60–104620.4	19.13 ± 0.21	VIRCAM	>17.97	VIRCAM
CWISEP J160835.01–244244.7	17.66 ± 0.04	WFCAM	>18.81	WFCAM	18.46 ± 0.18	WFCAM
CWISEP J161822.86–062310.2	20.42 ± 0.24	WIRC
CWISEP J165215.62+022918.5	>19.48	WFCAM
CWISEP J182358.73–740246.0	17.84 ± 0.06	VIRCAM	>17.85	VIRCAM
CWISEP J193518.58–154620.3	>21.70	FLAMINGOS-2	>18.00	VIRCAM
WISENF J193656.08+040801.2	>19.57	WFCAM
CWISEP J194101.59+542335.9	17.72 ± 0.04	WFCAM
CWISEP J194812.42–322334.9	17.98 ± 0.25	VIRCAM
CWISEP J201146.45–481259.7	>20.08	VIRCAM	>19.05	VIRCAM	>18.46	VIRCAM
CWISEP J201510.68–675005.6	16.90 ± 0.02	VIRCAM
CWISEP J203821.53–064930.9	19.56 ± 0.20	VIRCAM	>18.10	VIRCAM
CWISEP J205019.99–253652.8	17.57 ± 0.01	WIRC	>17.39	VIRCAM
CWISEP J210007.87–293139.8	>19.96	WIRC	>17.91	VIRCAM
CWISEP J212828.05+352912.4	>19.68	WFCAM
CWISEP J213249.05+690113.7	19.45 ± 0.04	WIRC
CWISEP J213838.74–313808.5	18.59 ± 0.07	VIRCAM	>17.43	VIRCAM
CWISEP J213930.45+042721.6	20.44 ± 0.10	FLAMINGOS-2
CWISEP J215841.50+732842.7	19.13 ± 0.60	WIRC
CWISEP J222035.35–810322.6	18.46 ± 0.03	FLAMINGOS-2	>17.50	VIRCAM
CWISEP J223022.60+254907.5	>21.16	WIRC
CWISEP J223138.55–383057.2	19.69 ± 0.13	VIRCAM	>18.38	VIRCAM
CWISEP J224916.17+371551.4	>19.53	WFCAM
CWISEP J225059.28–432057.2	19.90 ± 0.16	VIRCAM	>18.47	VIRCAM
CWISEP J225109.50–074037.7	18.09 ± 0.03	FLAMINGOS-2	>17.92	VIRCAM
CWISEP J225628.97+400227.3	21.70 ± 0.41	WIRC
CWISEP J230158.30–645858.3	20.46 ± 0.28	VIRCAM	>18.19	VIRCAM
CWISEP J233216.39–290025.0	17.95 ± 0.03	FLAMINGOS-2	18.01 ± 0.03	VIRCAM	17.86 ± 0.07	VIRCAM
CWISEP J235130.42–185800.2	19.38 ± 0.04	WIRC
CWISEP J235547.99+380438.9	20.28 ± 0.10	WIRC
CWISEP J235644.78–481456.3	21.77 ± 0.28	FLAMINGOS-2	>19.14	VIRCAM	>18.30	VIRCAM

Note.

^a Here CWISEP 0938+0634 appears to be in a sky region with nebulosity based on our Gemini J -band image. While this may be contaminating its J -band photometry, CWISEP 0938+0634 is nevertheless a real compact source with unambiguously confirmed motion (see Figure 5).

Table 10
 J -band Follow-up for Candidates Not Motion Confirmed

CWISEP Designation	J_{MKO} (mag)	origin
J021243.55+053147.2	22.75 ± 0.78	WIRC
J042455.68+000221.4	19.66 ± 0.07	WIRC
J100854.84+203136.6	20.73 ± 0.39	WIRC
J121358.13+294237.0	18.97 ± 0.05	WIRC
J131208.16–105231.8	20.60 ± 0.09	FLAMINGOS-2
J172104.42+595047.7	20.42 ± 0.13	WIRC
J175746.31+195112.6	>21.36 ^a	WIRC
J221736.94–222647.6	>21.56 ^{a,b}	FLAMINGOS-2

Notes.

^a Quoted limits are 5σ .

^b A smudge appears at the location of CWISEP 2217–2226, for which we quote a J -magnitude lower limit.

Kirkpatrick et al. (2019a) $M_{\text{ch2}}(\text{ch1} - \text{ch2})$ relation to the $\text{ch1} - \text{ch2}$ color obtained by subtracting this object's 1σ *Spitzer* color uncertainty from its central $\text{ch1} - \text{ch2}$ color. Correspondingly, we

quote only a distance upper limit of 8.3 pc for CWISEP 1446–2317 based on its M_{ch2} lower limit. Such limits should be treated with caution given our poor constraint on this object's *Spitzer* color.

The middle panel of Figure 9 shows a histogram of our motion-confirmed sample's photometric distance estimates. As discussed in Section 10.9, we suspect that many of the objects with unusually large distance estimates ($\gtrsim 50$ pc) may be subdwarfs. The median distance estimate for motion-confirmed targets is 26 pc. Propagating our M_{ch2} estimates and their error bars into distance estimates, the 1σ fractional uncertainty on our photometric distances is typically $\sim 15\%$.

10.3. Photometric Effective Temperature Estimates

Table 11 also provides T_{eff} estimates based on the Kirkpatrick et al. (2019a; Table 8) $T_{\text{eff}}(\text{ch1} - \text{ch2})$ polynomial relation. When calculating uncertainties on these T_{eff} estimates, we take into account both our 1σ $\text{ch1} - \text{ch2}$ color uncertainties and the 81 K residual scatter of the $T_{\text{eff}}(\text{ch1} - \text{ch2})$ polynomial

Table 11
Derived Properties for Motion-confirmed Targets with *Spitzer* Imaging Available

Name	SpT (Phototype)	M_{ch2} (mag)	Distance (pc)	T_{eff} (K)	H_{ch2} (mag)	V_{tan} (km s $^{-1}$)
CWISEP J000006.01–704851.2	7.0	13.21 $^{+0.31}_{-0.30}$	33.5 $^{+5.1}_{-4.4}$	813 $^{+85}_{-85}$	18.34 $^{+0.29}_{-0.26}$	50 $^{+10}_{-9}$
CWISEP J000110.81–093215.5	7.5	13.43 $^{+0.31}_{-0.31}$	31.0 $^{+4.7}_{-4.1}$	720 $^{+85}_{-85}$	18.88 $^{+0.44}_{-0.36}$	58 $^{+14}_{-13}$
CWISEP J001146.07–471306.8	8.5	13.73 $^{+0.33}_{-0.32}$	26.1 $^{+4.2}_{-3.6}$	628 $^{+88}_{-87}$	18.50 $^{+0.44}_{-0.36}$	43 $^{+10}_{-10}$
CWISEP J003507.77–153233.8	8.0	13.67 $^{+0.31}_{-0.31}$	20.5 $^{+3.2}_{-2.8}$	646 $^{+85}_{-85}$	18.94 $^{+0.17}_{-0.16}$	54 $^{+9}_{-8}$
CWISEP J004158.35+381811.9	8.0	13.51 $^{+0.32}_{-0.32}$	32.5 $^{+5.2}_{-4.5}$	695 $^{+89}_{-89}$	18.43 $^{+0.41}_{-0.34}$	46 $^{+11}_{-10}$
CWISEP J005802.63+723330.3	4.5	12.43 $^{+0.24}_{-0.24}$	73.2 $^{+8.6}_{-7.8}$...	20.30 $^{+0.27}_{-0.24}$	178 $^{+30}_{-28}$
CWISEP J010527.69–783419.3	9.0	13.94 $^{+0.32}_{-0.32}$	17.9 $^{+2.8}_{-2.4}$	576 $^{+85}_{-84}$	18.09 $^{+0.12}_{-0.12}$	32 $^{+5}_{-5}$
CWISEP J010650.61+225159.1	6.5	13.12 $^{+0.30}_{-0.30}$	25.3 $^{+3.8}_{-3.3}$	858 $^{+83}_{-83}$	17.69 $^{+0.25}_{-0.22}$	39 $^{+7}_{-7}$
CWISEP J012748.35–631056.1	6.5	13.07 $^{+0.30}_{-0.30}$	31.7 $^{+4.7}_{-4.1}$	885 $^{+84}_{-84}$	19.89 $^{+0.11}_{-0.11}$	109 $^{+17}_{-15}$
CWISEP J014607.55–375705.6	7.5	13.47 $^{+0.31}_{-0.31}$	27.7 $^{+4.2}_{-3.7}$	707 $^{+85}_{-85}$	19.70 $^{+0.19}_{-0.18}$	84 $^{+15}_{-13}$
CWISEP J015613.24+325526.6	7.0	13.20 $^{+0.31}_{-0.31}$	38.3 $^{+3.9}_{-3.1}$	817 $^{+90}_{-90}$	21.51 $^{+0.16}_{-0.15}$	217 $^{+37}_{-33}$
CWISEP J020103.10+293801.8	6.0	12.99 $^{+0.30}_{-0.30}$	39.2 $^{+5.9}_{-5.1}$	939 $^{+85}_{-85}$	19.70 $^{+0.28}_{-0.25}$	104 $^{+20}_{-18}$
CWISEP J020938.72+180427.7	8.0	13.55 $^{+0.32}_{-0.32}$	33.0 $^{+5.2}_{-4.5}$	682 $^{+88}_{-88}$	19.69 $^{+0.28}_{-0.25}$	80 $^{+16}_{-15}$
CWISEP J021921.66–265451.8	5.0	12.86 $^{+0.30}_{-0.30}$	68.2 $^{+10.2}_{-8.9}$	1073 $^{+97}_{-96}$	20.92 $^{+0.30}_{-0.26}$	193 $^{+38}_{-35}$
CWISEP J022122.41–564125.0	8.0	13.50 $^{+0.31}_{-0.31}$	26.9 $^{+4.1}_{-3.6}$	698 $^{+85}_{-85}$	17.59 $^{+0.42}_{-0.35}$	31 $^{+7}_{-7}$
CWISEP J022631.82–203439.4	7.5	13.39 $^{+0.31}_{-0.31}$	32.8 $^{+5.1}_{-4.4}$	738 $^{+87}_{-87}$	19.95 $^{+0.24}_{-0.22}$	98 $^{+18}_{-17}$
CWISEP J023842.60–133210.7	≥ 11.0	15.05 $^{+0.54}_{-0.51}$	18.0 $^{+4.8}_{-4.0}$	399 $^{+97}_{-97}$	20.73 $^{+0.23}_{-0.21}$	65 $^{+18}_{-16}$
CWISEP J024204.91–225604.6	8.5	13.78 $^{+0.34}_{-0.34}$	33.8 $^{+5.7}_{-4.9}$	615 $^{+91}_{-90}$	21.56 $^{+0.16}_{-0.15}$	170 $^{+31}_{-28}$
CWISEP J031130.28+035931.8	5.0	12.53 $^{+0.25}_{-0.24}$	79.9 $^{+9.5}_{-8.7}$...	20.97 $^{+0.41}_{-0.35}$	231 $^{+49}_{-47}$
CWISEP J031935.50–041231.7	9.5	14.27 $^{+0.44}_{-0.42}$	28.5 $^{+6.0}_{-5.2}$	510 $^{+99}_{-96}$	20.16 $^{+0.41}_{-0.35}$	71 $^{+20}_{-18}$
CWISEP J032109.59+693204.5	10.5	14.86 $^{+0.48}_{-0.46}$	16.3 $^{+3.8}_{-3.2}$	421 $^{+94}_{-92}$	20.96 $^{+0.14}_{-0.13}$	79 $^{+19}_{-16}$
CWISEP J034755.11+123051.9	7.5	13.36 $^{+0.30}_{-0.30}$	22.8 $^{+3.4}_{-3.0}$	747 $^{+83}_{-83}$	18.05 $^{+0.23}_{-0.21}$	41 $^{+7}_{-7}$
CWISEP J034904.05–462827.9	7.0	13.27 $^{+0.31}_{-0.31}$	40.4 $^{+6.2}_{-5.4}$	784 $^{+89}_{-88}$	20.00 $^{+0.23}_{-0.21}$	105 $^{+19}_{-17}$
CWISEP J040106.67+085748.5	8.5	13.71 $^{+0.32}_{-0.32}$	24.7 $^{+3.9}_{-3.4}$	633 $^{+86}_{-86}$	19.20 $^{+0.29}_{-0.25}$	59 $^{+12}_{-11}$
CWISEP J040235.55–265145.4	≥ 11.0	15.03 $^{+0.43}_{-0.42}$	12.2 $^{+2.6}_{-2.2}$	401 $^{+89}_{-87}$	20.33 $^{+0.08}_{-0.08}$	55 $^{+12}_{-10}$
CWISEP J040351.00–491605.6	8.5	13.81 $^{+0.35}_{-0.35}$	29.0 $^{+5.0}_{-4.4}$	608 $^{+93}_{-92}$	18.52 $^{+0.35}_{-0.30}$	41 $^{+9}_{-9}$
CWISEP J042404.54+665011.2	8.0	13.50 $^{+0.31}_{-0.31}$	27.0 $^{+4.2}_{-3.6}$	696 $^{+86}_{-86}$	18.64 $^{+0.23}_{-0.20}$	51 $^{+9}_{-8}$
CWISEP J043034.27+255653.7	6.0	13.04 $^{+0.30}_{-0.30}$	22.4 $^{+3.3}_{-2.9}$	907 $^{+82}_{-82}$	18.04 $^{+0.14}_{-0.13}$	47 $^{+8}_{-7}$
CWISEP J043309.31+100902.9	8.0	13.54 $^{+0.31}_{-0.31}$	21.0 $^{+3.2}_{-2.8}$	684 $^{+84}_{-83}$	18.27 $^{+0.19}_{-0.18}$	42 $^{+7}_{-7}$
CWISEP J044719.61+202158.1	9.0	14.05 $^{+0.36}_{-0.35}$	21.8 $^{+3.8}_{-3.3}$	553 $^{+90}_{-89}$	19.71 $^{+0.19}_{-0.18}$	64 $^{+12}_{-11}$
CWISEP J050521.29–591311.7	6.5	13.14 $^{+0.31}_{-0.31}$	40.2 $^{+6.1}_{-5.3}$	846 $^{+88}_{-87}$	21.37 $^{+0.08}_{-0.07}$	210 $^{+33}_{-29}$
CWISEP J052346.34–545314.7	9.5	14.39 $^{+0.39}_{-0.38}$	22.8 $^{+4.4}_{-3.8}$	489 $^{+92}_{-90}$	20.30 $^{+0.17}_{-0.16}$	72 $^{+15}_{-13}$
CWISEPR J062436.84–071147.2	7.5	13.34 $^{+0.31}_{-0.31}$	24.8 $^{+3.8}_{-3.3}$	756 $^{+84}_{-84}$	16.03 $^{+0.49}_{-0.40}$	16 $^{+4}_{-4}$
CWISEP J062742.27–215908.1	7.5	13.47 $^{+0.32}_{-0.32}$	31.1 $^{+4.9}_{-4.2}$	709 $^{+88}_{-88}$	18.81 $^{+0.39}_{-0.33}$	56 $^{+13}_{-12}$
CWISEP J063428.10+504925.9	10.0	14.47 $^{+0.41}_{-0.40}$	19.8 $^{+4.0}_{-3.4}$	476 $^{+92}_{-91}$	21.11 $^{+0.14}_{-0.13}$	101 $^{+21}_{-18}$
CWISEP J063845.48–615937.2	7.0	13.22 $^{+0.31}_{-0.31}$	47.8 $^{+7.4}_{-6.5}$	808 $^{+91}_{-91}$	19.74 $^{+0.38}_{-0.32}$	96 $^{+21}_{-20}$
CWISEPR J065144.62–115106.1	7.0	13.26 $^{+0.30}_{-0.30}$	26.8 $^{+4.0}_{-3.5}$	790 $^{+84}_{-84}$	17.01 $^{+0.50}_{-0.41}$	27 $^{+7}_{-6}$
CWISEP J070055.19+783834.0	6.0	13.01 $^{+0.31}_{-0.30}$	54.9 $^{+5.1}_{-4.2}$	925 $^{+91}_{-90}$	22.22 $^{+0.18}_{-0.17}$	329 $^{+56}_{-51}$
CWISEP J070214.84–544041.7	7.5	13.39 $^{+0.32}_{-0.32}$	42.6 $^{+6.8}_{-5.9}$	734 $^{+92}_{-91}$	20.30 $^{+0.29}_{-0.26}$	114 $^{+23}_{-21}$
CWISEP J071813.30–061421.1	5.0	12.53 $^{+0.25}_{-0.24}$	81.3 $^{+9.7}_{-8.8}$...	20.51 $^{+0.45}_{-0.37}$	188 $^{+42}_{-41}$
CWISEP J085908.26+152527.1	8.0	13.67 $^{+0.31}_{-0.31}$	20.5 $^{+3.2}_{-2.7}$	645 $^{+84}_{-84}$	17.43 $^{+0.37}_{-0.31}$	27 $^{+6}_{-5}$
CWISEP J085938.95+534908.7	10.0	14.64 $^{+0.44}_{-0.42}$	18.7 $^{+4.0}_{-3.4}$	451 $^{+94}_{-91}$	18.88 $^{+0.34}_{-0.30}$	33 $^{+9}_{-8}$
CWISEP J090536.35+740009.1	6.0	13.01 $^{+0.30}_{-0.30}$	47.9 $^{+7.2}_{-6.3}$	930 $^{+87}_{-87}$	22.37 $^{+0.10}_{-0.10}$	354 $^{+56}_{-49}$
CWISEP J093111.03+232502.1	7.5	13.42 $^{+0.31}_{-0.31}$	28.6 $^{+3.9}_{-3.9}$	726 $^{+87}_{-87}$	19.44 $^{+0.30}_{-0.27}$	76 $^{+15}_{-14}$
CWISEP J093236.66–180029.3	8.5	13.83 $^{+0.32}_{-0.32}$	23.7 $^{+3.8}_{-3.3}$	602 $^{+86}_{-86}$	19.05 $^{+0.28}_{-0.25}$	52 $^{+11}_{-10}$
CWISEP J093852.89+063440.6	10.0	14.58 $^{+0.43}_{-0.41}$	18.9 $^{+4.0}_{-3.4}$	460 $^{+93}_{-91}$	20.63 $^{+0.15}_{-0.14}$	77 $^{+17}_{-15}$
CWISEP J094005.50+523359.2	≥ 11.0	15.12 $^{+0.47}_{-0.45}$	13.4 $^{+3.1}_{-2.6}$	391 $^{+91}_{-89}$	19.04 $^{+0.26}_{-0.23}$	29 $^{+7}_{-7}$
CWISEP J094615.56+351434.3	5.5	12.95 $^{+0.30}_{-0.30}$	42.2 $^{+6.3}_{-5.5}$	975 $^{+86}_{-86}$	20.22 $^{+0.22}_{-0.20}$	135 $^{+24}_{-22}$
CWISEP J094930.41+663937.2	9.5	14.24 $^{+0.36}_{-0.35}$	23.6 $^{+4.2}_{-3.6}$	517 $^{+89}_{-88}$	18.47 $^{+0.50}_{-0.41}$	33 $^{+9}_{-9}$
CWISEP J095930.71–401046.8	3.5	12.25 $^{+0.23}_{-0.23}$	124.8 $^{+14.6}_{-13.2}$...	21.94 $^{+0.36}_{-0.31}$	410 $^{+79}_{-76}$
CWISEP J100629.01+105408.5	8.5	13.90 $^{+0.33}_{-0.33}$	21.4 $^{+3.5}_{-3.0}$	585 $^{+87}_{-86}$	17.62 $^{+0.43}_{-0.36}$	26 $^{+6}_{-6}$
CWISEP J102201.27+145520.2	8.5	13.74 $^{+0.32}_{-0.32}$	26.2 $^{+4.2}_{-3.6}$	626 $^{+87}_{-87}$	19.61 $^{+0.25}_{-0.22}$	71 $^{+14}_{-12}$
CWISEP J103453.14+161228.0	7.5	13.46 $^{+0.30}_{-0.30}$	19.2 $^{+2.9}_{-2.5}$	710 $^{+83}_{-83}$	17.08 $^{+0.25}_{-0.22}$	25 $^{+5}_{-4}$
CWISEP J104104.20+221613.6	9.5	14.23 $^{+0.45}_{-0.43}$	30.4 $^{+6.7}_{-5.7}$	517 $^{+103}_{-99}$	20.43 $^{+0.49}_{-0.40}$	82 $^{+24}_{-23}$
CWISEP J104446.56+001754.9	9.0	13.94 $^{+0.34}_{-0.34}$	25.7 $^{+4.3}_{-3.8}$	577 $^{+89}_{-88}$	20.68 $^{+0.23}_{-0.21}$	106 $^{+21}_{-19}$
CWISEP J104756.81+545741.6	10.0	14.57 $^{+0.43}_{-0.41}$	21.7 $^{+4.6}_{-3.9}$	461 $^{+94}_{-91}$	19.66 $^{+0.36}_{-0.31}$	50 $^{+13}_{-12}$
CWISEP J110021.08+094652.9	8.0	13.64 $^{+0.32}_{-0.32}$	25.0 $^{+3.9}_{-3.4}$	655 $^{+87}_{-87}$	19.61 $^{+0.17}_{-0.16}$	74 $^{+13}_{-12}$

Table 11
(Continued)

Name	SpT (Prototype)	M_{ch2} (mag)	Distance (pc)	T_{eff} (K)	H_{ch2} (mag)	V_{tan} (km s $^{-1}$)
CWISEP J111055.12–174738.2	7.5	13.32 $^{+0.30}_{-0.30}$	22.1 $^{+3.3}_{-2.9}$	763 $^{+83}_{-83}$	18.03 $^{+0.16}_{-0.15}$	41 $^{+7}_{-6}$
CWISEP J113010.21+313947.3	6.0	13.05 $^{+0.30}_{-0.30}$	28.2 $^{+4.2}_{-3.7}$	901 $^{+83}_{-83}$	21.68 $^{+0.05}_{-0.05}$	253 $^{+38}_{-33}$
CWISEP J120444.33–235926.8	7.5	13.35 $^{+0.31}_{-0.30}$	24.5 $^{+3.7}_{-3.2}$	751 $^{+84}_{-84}$	18.97 $^{+0.16}_{-0.15}$	63 $^{+10}_{-9}$
CWISEP J122010.03+281431.3	7.0	13.30 $^{+0.31}_{-0.31}$	32.5 $^{+5.0}_{-4.3}$	770 $^{+86}_{-86}$	18.97 $^{+0.28}_{-0.25}$	64 $^{+13}_{-12}$
CWISEP J124138.41–820051.9	8.5	13.87 $^{+0.32}_{-0.32}$	19.7 $^{+3.1}_{-2.7}$	595 $^{+85}_{-85}$	17.23 $^{+0.22}_{-0.20}$	22 $^{+4}_{-4}$
CWISEP J130255.54+191145.9	8.0	13.59 $^{+0.32}_{-0.31}$	24.8 $^{+3.9}_{-3.4}$	670 $^{+86}_{-86}$	17.56 $^{+0.45}_{-0.37}$	30 $^{+7}_{-7}$
CWISEP J131252.97+341746.5	7.5	13.46 $^{+0.33}_{-0.32}$	38.7 $^{+6.2}_{-5.4}$	713 $^{+92}_{-91}$	19.22 $^{+0.50}_{-0.40}$	67 $^{+18}_{-17}$
CWISEP J131221.97–310845.7	8.0	13.67 $^{+0.32}_{-0.32}$	26.8 $^{+4.2}_{-3.7}$	646 $^{+87}_{-86}$	19.40 $^{+0.22}_{-0.20}$	67 $^{+12}_{-11}$
CWISEP J131350.91–440352.2	7.5	13.39 $^{+0.31}_{-0.31}$	27.7 $^{+4.2}_{-3.6}$	736 $^{+84}_{-84}$	19.15 $^{+0.21}_{-0.19}$	67 $^{+12}_{-11}$
CWISEP J135937.65–435226.9	10.0	14.50 $^{+0.39}_{-0.38}$	19.5 $^{+3.7}_{-3.2}$	472 $^{+90}_{-89}$	18.73 $^{+0.50}_{-0.40}$	33 $^{+9}_{-9}$
CWISEP J140118.30+432554.2	6.5	13.12 $^{+0.30}_{-0.30}$	32.0 $^{+4.8}_{-4.2}$	861 $^{+85}_{-85}$	19.81 $^{+0.11}_{-0.11}$	103 $^{+16}_{-14}$
CWISEP J140247.83+102132.6	5.0	12.53 $^{+0.25}_{-0.24}$	24.1 $^{+2.8}_{-2.6}$...	15.33 $^{+0.25}_{-0.23}$	17 $^{+3}_{-3}$
CWISEP J141206.85+234412.4	6.0	13.03 $^{+0.30}_{-0.30}$	43.4 $^{+6.5}_{-5.7}$	912 $^{+86}_{-86}$	20.31 $^{+0.20}_{-0.19}$	135 $^{+24}_{-21}$
CWISEP J143439.23–134421.4	9.0	14.00 $^{+0.36}_{-0.35}$	27.0 $^{+4.8}_{-4.2}$	565 $^{+92}_{-91}$	19.63 $^{+0.35}_{-0.30}$	63 $^{+15}_{-14}$
CWISEP J144606.62–231717.8	≥ 11.0	>16.23	<8.3	<381	21.35 $^{+0.12}_{-0.12}$	<53
CWISEP J145837.91+173450.1	8.0	13.61 $^{+0.31}_{-0.31}$	21.6 $^{+3.3}_{-2.9}$	664 $^{+84}_{-84}$	18.84 $^{+0.11}_{-0.10}$	53 $^{+9}_{-7}$
CWISEP J150252.82–304232.8	7.0	13.29 $^{+0.30}_{-0.30}$	22.3 $^{+3.3}_{-2.9}$	775 $^{+83}_{-83}$	18.42 $^{+0.15}_{-0.14}$	50 $^{+8}_{-7}$
WISEA J153429.75–104303.3	5.0	12.87 $^{+0.30}_{-0.30}$	38.0 $^{+5.6}_{-4.9}$	1062 $^{+83}_{-83}$	22.92 $^{+0.06}_{-0.06}$	485 $^{+73}_{-64}$
CWISEP J153859.39+482659.1	9.5	14.23 $^{+0.38}_{-0.37}$	20.7 $^{+3.9}_{-3.3}$	518 $^{+92}_{-91}$	19.13 $^{+0.17}_{-0.16}$	45 $^{+9}_{-8}$
CWISEP J160311.60–104620.4	8.0	13.51 $^{+0.31}_{-0.31}$	25.9 $^{+4.0}_{-3.5}$	694 $^{+87}_{-86}$	20.39 $^{+0.13}_{-0.13}$	113 $^{+19}_{-17}$
CWISEP J160835.01–244244.7	7.0	13.25 $^{+0.30}_{-0.30}$	23.6 $^{+3.5}_{-3.1}$	793 $^{+83}_{-83}$	17.49 $^{+0.29}_{-0.26}$	33 $^{+7}_{-6}$
CWISEP J161822.86–062310.2	8.5	13.76 $^{+0.32}_{-0.32}$	24.0 $^{+3.8}_{-3.3}$	621 $^{+86}_{-86}$	18.46 $^{+0.34}_{-0.29}$	41 $^{+9}_{-8}$
CWISEP J162225.92+370118.8	6.5	13.09 $^{+0.31}_{-0.30}$	42.2 $^{+6.4}_{-5.6}$	878 $^{+88}_{-88}$	20.09 $^{+0.18}_{-0.17}$	119 $^{+20}_{-18}$
CWISEP J165215.62+022918.5	4.5	12.43 $^{+0.24}_{-0.24}$	80.4 $^{+9.4}_{-8.6}$...	20.13 $^{+0.46}_{-0.38}$	165 $^{+37}_{-36}$
CWISEP J182358.73–740246.0	6.0	13.01 $^{+0.30}_{-0.30}$	32.4 $^{+4.8}_{-4.2}$	927 $^{+85}_{-84}$	18.98 $^{+0.28}_{-0.25}$	74 $^{+14}_{-13}$
CWISEP J185658.80+601351.4	6.0	13.01 $^{+0.30}_{-0.30}$	33.3 $^{+5.0}_{-4.3}$	930 $^{+84}_{-84}$	20.16 $^{+0.08}_{-0.08}$	128 $^{+20}_{-17}$
CWISEP J193518.58–154620.3	≥ 11.0	15.57 $^{+0.31}_{-0.31}$	9.8 $^{+5}_{-1.3}$	347 $^{+81}_{-81}$	17.97 $^{+0.48}_{-0.39}$	14 $^{+3}_{-3}$
WISENF J193656.08+040801.2	10.0	14.45 $^{+0.32}_{-0.32}$	11.1 $^{+1.8}_{-1.5}$	479 $^{+83}_{-83}$	20.17 $^{+0.07}_{-0.07}$	66 $^{+11}_{-9}$
CWISEP J194101.59+542335.9	7.0	13.25 $^{+0.31}_{-0.30}$	28.3 $^{+4.3}_{-3.7}$	793 $^{+85}_{-84}$	17.16 $^{+0.24}_{-0.22}$	29 $^{+5}_{-5}$
CWISEP J194812.42–322334.9	5.5	12.91 $^{+0.30}_{-0.30}$	38.3 $^{+5.7}_{-5.0}$	1011 $^{+84}_{-84}$	18.65 $^{+0.44}_{-0.37}$	67 $^{+16}_{-15}$
CWISEP J201146.45–481259.7	10.0	14.61 $^{+0.37}_{-0.36}$	13.9 $^{+2.5}_{-2.2}$	455 $^{+87}_{-86}$	18.04 $^{+0.24}_{-0.21}$	23 $^{+5}_{-4}$
CWISEP J201510.68–675005.6	6.0	13.05 $^{+0.30}_{-0.30}$	21.1 $^{+3.1}_{-2.7}$	903 $^{+82}_{-82}$	16.21 $^{+0.24}_{-0.22}$	20 $^{+4}_{-3}$
CWISEP J203821.53–064930.9	9.5	14.21 $^{+0.33}_{-0.33}$	19.1 $^{+3.1}_{-2.7}$	521 $^{+85}_{-85}$	18.88 $^{+0.37}_{-0.32}$	41 $^{+9}_{-9}$
CWISEP J205019.99–253652.8	7.0	13.29 $^{+0.30}_{-0.30}$	22.8 $^{+3.4}_{-3.0}$	777 $^{+83}_{-83}$	17.67 $^{+0.23}_{-0.21}$	36 $^{+6}_{-6}$
CWISEP J205908.95+024105.6	7.5	13.38 $^{+0.31}_{-0.31}$	26.8 $^{+4.1}_{-3.6}$	738 $^{+85}_{-85}$	20.13 $^{+0.13}_{-0.13}$	106 $^{+17}_{-15}$
CWISEP J210007.87–293139.8	9.5	14.43 $^{+0.42}_{-0.40}$	20.2 $^{+4.1}_{-3.5}$	484 $^{+94}_{-92}$	18.93 $^{+0.44}_{-0.36}$	38 $^{+10}_{-10}$
CWISEP J212828.05+352912.4	5.5	12.92 $^{+0.31}_{-0.31}$	67.1 $^{+10.2}_{-9.0}$	999 $^{+102}_{-101}$	20.16 $^{+0.49}_{-0.40}$	132 $^{+33}_{-32}$
CWISEP J213249.05+690113.7	8.5	13.79 $^{+0.32}_{-0.31}$	19.8 $^{+3.1}_{-2.7}$	614 $^{+85}_{-85}$	17.59 $^{+0.18}_{-0.17}$	27 $^{+5}_{-4}$
CWISEP J213838.74–313808.5	8.0	13.54 $^{+0.31}_{-0.31}$	20.8 $^{+3.2}_{-2.8}$	683 $^{+84}_{-84}$	19.14 $^{+0.12}_{-0.12}$	62 $^{+10}_{-9}$
CWISEP J213930.45+042721.6	9.0	14.07 $^{+0.34}_{-0.34}$	21.7 $^{+3.6}_{-3.1}$	550 $^{+88}_{-87}$	19.21 $^{+0.33}_{-0.28}$	51 $^{+11}_{-10}$
CWISEP J215841.50+732842.7	8.0	13.53 $^{+0.31}_{-0.31}$	21.2 $^{+3.2}_{-2.8}$	688 $^{+84}_{-84}$	16.25 $^{+0.33}_{-0.28}$	17 $^{+3}_{-3}$
CWISEP J222035.35–810322.6	6.5	13.14 $^{+0.31}_{-0.31}$	37.4 $^{+5.7}_{-5.0}$	847 $^{+88}_{-88}$	18.70 $^{+0.34}_{-0.29}$	61 $^{+13}_{-12}$
CWISEP J223022.60+254907.5	≥ 11.0	15.25 $^{+0.70}_{-0.64}$	16.1 $^{+5.6}_{-4.4}$	377 $^{+106}_{-98}$	20.59 $^{+0.22}_{-0.20}$	56 $^{+20}_{-16}$
CWISEP J223138.55–383057.2	8.5	13.71 $^{+0.33}_{-0.32}$	30.0 $^{+4.9}_{-4.2}$	634 $^{+88}_{-88}$	20.05 $^{+0.27}_{-0.24}$	88 $^{+18}_{-16}$
CWISEP J224916.17+371551.4	9.5	14.31 $^{+0.38}_{-0.37}$	23.9 $^{+4.5}_{-3.9}$	503 $^{+91}_{-90}$	19.28 $^{+0.50}_{-0.40}$	47 $^{+13}_{-12}$
CWISEP J225059.28–432057.2	8.0	13.67 $^{+0.33}_{-0.33}$	31.2 $^{+5.1}_{-4.4}$	644 $^{+89}_{-88}$	19.59 $^{+0.37}_{-0.32}$	72 $^{+16}_{-15}$
CWISEP J225156.13+392408.4	7.5	13.42 $^{+0.31}_{-0.31}$	27.5 $^{+4.7}_{-4.2}$	725 $^{+86}_{-85}$	18.21 $^{+0.34}_{-0.29}$	43 $^{+9}_{-8}$
CWISEP J225109.50–074037.7	8.0	13.53 $^{+0.31}_{-0.31}$	20.6 $^{+3.1}_{-2.7}$	687 $^{+84}_{-84}$	19.37 $^{+0.13}_{-0.12}$	70 $^{+11}_{-10}$
CWISEP J225628.97+400227.3	≥ 11.0	15.64 $^{+0.60}_{-0.56}$	10.8 $^{+3.2}_{-2.6}$	341 $^{+93}_{-89}$	20.08 $^{+0.14}_{-0.13}$	37 $^{+11}_{-9}$
CWISEP J230158.30–645858.3	8.5	13.70 $^{+0.31}_{-0.31}$	21.5 $^{+3.3}_{-2.9}$	636 $^{+84}_{-84}$	18.65 $^{+0.14}_{-0.14}$	46 $^{+8}_{-7}$
CWISEP J233216.39–290025.0	6.0	12.97 $^{+0.30}_{-0.30}$	33.5 $^{+5.0}_{-4.4}$	957 $^{+83}_{-83}$	18.42 $^{+0.43}_{-0.36}$	58 $^{+14}_{-13}$
CWISEP J235130.42–185800.2	8.5	13.86 $^{+0.33}_{-0.33}$	22.2 $^{+3.6}_{-3.1}$	595 $^{+88}_{-87}$	19.06 $^{+0.22}_{-0.20}$	52 $^{+10}_{-9}$
CWISEPJ235547.99+380438.9	10.0	14.65 $^{+0.58}_{-0.54}$	18.0 $^{+5.0}_{-4.2}$	450 $^{+109}_{-102}$	20.05 $^{+0.22}_{-0.20}$	57 $^{+17}_{-14}$
CWISEP J235644.78–481456.3	10.5	14.97 $^{+0.54}_{-0.51}$	16.4 $^{+4.3}_{-3.6}$	408 $^{+98}_{-94}$	21.16 $^{+0.20}_{-0.18}$	82 $^{+23}_{-19}$

Note. Photometric spectral type values are defined such that SpT = 6 for T6, SpT = 7 for T7, ..., SpT = 11 for Y1.

Table 12
Summary of Motion-confirmed Discoveries Meriting Further Follow-up to Better Assess Y Dwarf Candidacy

Name	SpT (Phototype)	ch1–ch2 (mag)	$[(\text{ch1}-\text{ch2})-2.4]/\sigma_{\text{ch1}-\text{ch2}}$ (Dimensionless)	$J - \text{ch2}$ (mag)
CWISEP J144606.62–231717.8	≥ 11.0	3.709 ± 0.435	3.01	>6.56
CWISEP J225628.97+400227.3	≥ 11.0	3.014 ± 0.227	2.71	5.90 ± 0.41
CWISEP J193518.58–154620.3	≥ 11.0	2.984 ± 0.034	17.15	>6.17
CWISEP J223022.60+254907.5	≥ 11.0	2.830 ± 0.293	1.47	>4.87
CWISEP J094005.50+523359.2	≥ 11.0	2.766 ± 0.175	2.09	>5.50
CWISEP J023842.60–133210.7	≥ 11.0	2.729 ± 0.220	1.50	>5.13
CWISEP J040235.55–265145.4	≥ 11.0	2.720 ± 0.152	2.10	>4.89
CWISEP J235644.78–481456.3	10.5	2.687 ± 0.220	1.31	5.73 ± 0.28
CWISEP J032109.59+693204.5	10.5	2.633 ± 0.190	1.23	>5.23
CWISEP J235547.99+380438.9	10.0	2.518 ± 0.261	0.45	4.35 ± 0.10^a
CWISEP J085938.95+534908.7	10.0	2.514 ± 0.173	0.66	>3.70
CWISEP J201146.45–481259.7	10.0	2.496 ± 0.118	0.82	>4.76
CWISEP J093852.89+063440.6	10.0	2.480 ± 0.166	0.48	5.07 ± 0.12
CWISEP J104756.81+545741.6	10.0	2.474 ± 0.168	0.44	>3.57
CWISEP J135937.65–435226.9	10.0	2.434 ± 0.137	0.25	>3.36
CWISEP J063428.10+504925.9	10.0	2.418 ± 0.155	0.12	>3.57
WISENF J193656.08+040801.2	10.0	2.407 ± 0.064	0.10	>4.88
Phototype < 10 , no $J < (\text{ch2}+5)$ detection, within 1σ of $\text{ch1}-\text{ch2} = 2.4$				
CWISEP J210007.87–293139.8	9.5	2.392 ± 0.163	–0.05	>4.00
CWISEP J052346.34–545314.7	9.5	2.372 ± 0.146	–0.19	>3.83
CWISEP J224916.17+371551.4	9.5	2.324 ± 0.140	–0.54	>3.33
CWISEP J104104.20+221613.6	9.5	2.274 ± 0.201	–0.62	>2.93
Phototype < 10 , $\text{ch1}-\text{ch2} > 2.11$ mag, no $J < (\text{ch2}+5)$ detection, not within 1σ of $\text{ch1}-\text{ch2} = 2.4$				
CWISEP J094930.41+663937.2	9.5	2.276 ± 0.120	–1.03	...
CWISEP J044719.61+202158.1	9.0	2.156 ± 0.124	–1.97	>4.08
CWISEP J143439.23–134421.4	9.0	2.121 ± 0.133	–2.10	>3.39

Notes. Photometric spectral type values are defined such that SpT = 6 for T6, SpT = 7 for T7, ..., SpT = 11 for Y1.

^a The relatively blue $J - \text{ch2}$ color of CWISEP 2355+3804 suggests that it is a late-T dwarf despite its *Spitzer*-based phototype of Y0.

fit relative to its training data. This floors our quoted T_{eff} uncertainties at 81 K.

The Kirkpatrick et al. (2019a) $T_{\text{eff}}(\text{ch1}-\text{ch2})$ relation is only valid for $0.9 \leq \text{ch1}-\text{ch2} \leq 3.7$. We omit T_{eff} estimates for the handful of our motion-confirmed discoveries with $\text{ch1}-\text{ch2} < 0.9$ mag. There is currently no $T_{\text{eff}}(\text{ch1}-\text{ch2})$ relation available in this early-to-mid-T regime, and within this range of spectral types, T_{eff} maintains a roughly uniform value of ~ 1400 – 1500 K anyway (e.g., Kirkpatrick 2005; Figure 7).

The best-fit CWISEP 1446–2317 *Spitzer* color is too red for the Kirkpatrick et al. (2019a) $T_{\text{eff}}(\text{ch1}-\text{ch2})$ relation. We therefore quote only an upper limit of $T_{\text{eff}} < 381$ K for CWISEP 1446–2317. This value arises from evaluating the $T_{\text{eff}}(\text{ch1}-\text{ch2})$ formula at a color 1σ bluer than the central value and further adding the aforementioned 81 K systematics floor of the T_{eff} relation in an attempt to be conservative.

10.4. Reduced Proper Motions and Tangential Velocities

Reduced proper motions (H_{ch2}) can be calculated entirely on the basis of directly measured quantities: μ_{tot} (Table 7) and apparent ch2 magnitude (Table 1). In calculating uncertainties on H_{ch2} , we account for the uncertainties on both μ_{tot} and ch2 magnitude. Table 11 lists H_{ch2} for all motion-confirmed targets with *Spitzer* imaging available. Figure 10 shows a scatter plot of H_{ch2} versus $\text{ch1}-\text{ch2}$ color for the same set of our discoveries, plus all Y dwarfs from the prior literature to provide context. Interestingly, all three of our motion-confirmed discoveries with $H_{\text{ch2}} > 22$ mag are rather blue in $\text{ch1}-\text{ch2}$ color relative to the bulk of our sample. These three

objects (CWISEP 0700+7838, CWISEP 0905+7400, and WISEA 1534–1043) have $\text{ch1}-\text{ch2} < 1.25$ mag, making all of them bluer in *Spitzer* color than at least 85% of our motion-confirmed sample.

Computing V_{tan} values requires making use of our photometric distance estimates from Section 10.2. In computing uncertainties on V_{tan} , we account for the uncertainties on both μ_{tot} and our distance estimates. Table 11 provides our V_{tan} estimates for motion-confirmed targets with *Spitzer* imaging available. The bottom panel of Figure 9 displays a histogram of the central V_{tan} values for this sample. As discussed in Section 10.9, a number of our highest V_{tan} motion-confirmed discoveries are also color outliers.

For CWISEP 1446–2317, our distance upper limit from Table 11 translates into a V_{tan} upper limit, $V_{\text{tan}} < 53 \text{ km s}^{-1}$.

10.5. Y Dwarf Candidates

Seventeen of our motion-confirmed discoveries have best-fit phototypes $\geq Y0$. In practice, within the spectral type estimation framework described in Section 10.1, this is to say that 17 of our motion-confirmed targets have central $\text{ch1}-\text{ch2}$ colors of at least 2.40 mag. Plots of our astrometric measurements and linear motion fits for all 17 of these Y dwarf candidates are shown in Figure 5. An 18th target, CWISEP 0212+0531, has $\text{ch1}-\text{ch2} > 2.40$ mag, but its motion appears to be disconfirmed (or else very small) in light of our combined *WISE* and *Spitzer* astrometry.

Given our Section 10.1 appraisal that the spectral type estimates for our reddest objects carry an uncertainty of

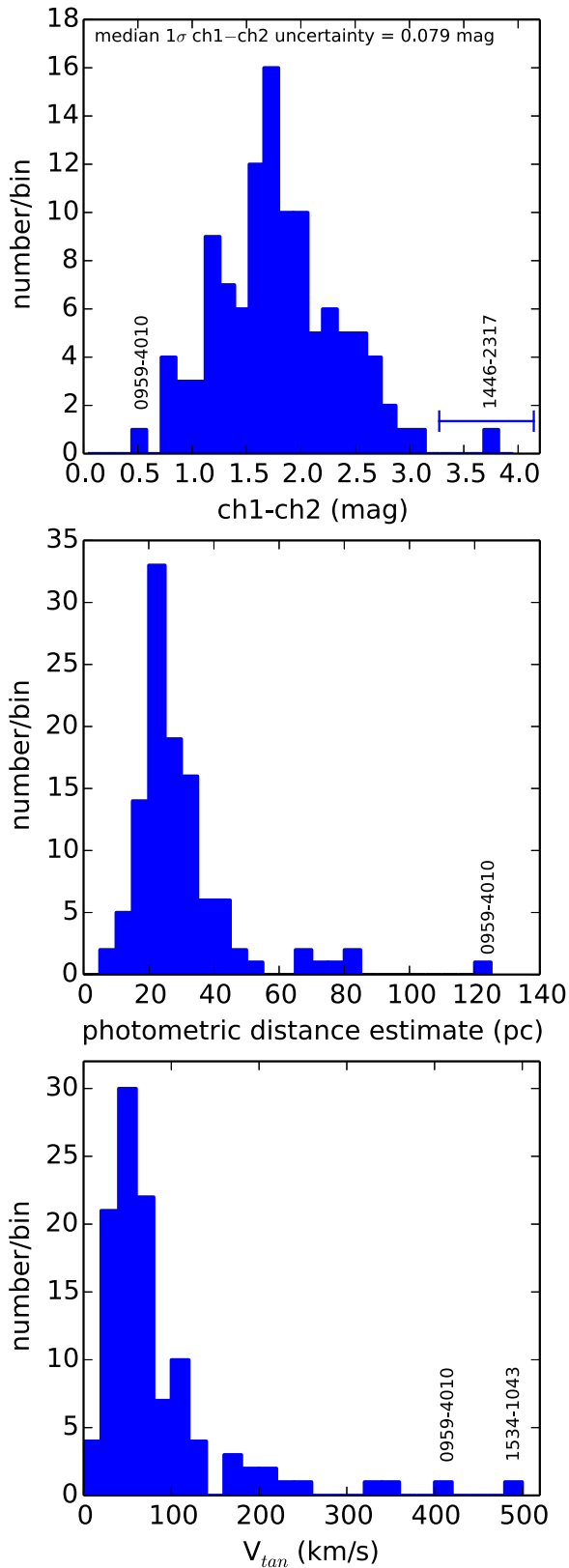


Figure 9. Histograms of measured *Spitzer* colors (top) and selected derived parameters (middle: photometric distance estimates; bottom: V_{tan} estimates) from Table 11 for motion-confirmed discoveries with *Spitzer* photometry available. The short names of outliers are added as annotations. As discussed in Section 10.9, we hypothesize that several objects with unusually large V_{tan} and/or distance estimates may be late-type subdwarfs.

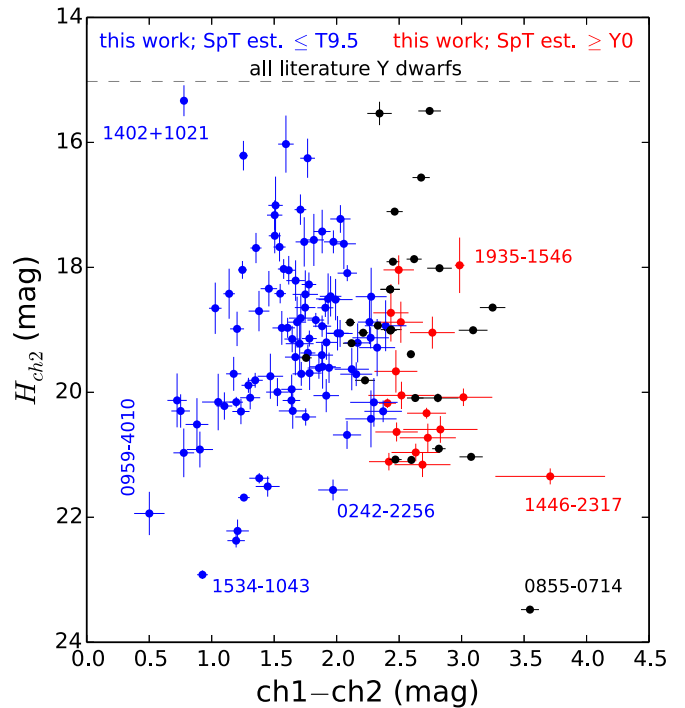


Figure 10. Reduced proper-motion diagram showing all Y dwarfs from the prior literature (black) and all motion-confirmed discoveries from this study with *Spitzer* photometry available. Our targets with the best-fit $\text{ch1}-\text{ch2}$ color most consistent with spectral type Y are shown in red, while all of our discoveries with earlier spectral type estimates are shown in blue.

roughly one type, we cannot yet specify an exact list of our targets that will ultimately turn out to fall on the late-type side of the T/Y boundary. Nevertheless, we can perform some cross-checks on the hypothesis that our 17 reddest motion-confirmed discoveries are indeed Y dwarfs and rate the relative likelihood that particular objects in this sample are or are not in fact “merely” T dwarfs.

We find that the archival and follow-up JHK/K_S NIR photometry assembled in Section 9 is consistent with the proposition that most motion-confirmed objects with $\text{ch1}-\text{ch2} \geq 2.4$ mag are Y dwarfs. All 17 targets with phototypes $\geq Y0$ have J -band imaging available. Four of these targets have J -band detections: CWISEP 0938+0634, CWISEP 2256+4002, CWISEP 2355+3804, and CWISEP 2356–4814. Their respective $J - \text{ch2}$ colors are 5.07 ± 0.12 , 5.90 ± 0.41 , 4.35 ± 0.10 , and 5.73 ± 0.28 mag. Three of these $J - \text{ch2}$ colors are consistent with Y spectral types. The fourth $J - \text{ch2}$ color, for CWISEP 2355+3804, seems to provide an indication that this target may actually be a late-T dwarf.

The remaining 13 targets with type estimates $\geq Y0$ have $J - \text{ch2}$ limits available. Among these, five objects have 5σ J limits establishing that $J - \text{ch2} > 5$ mag, bolstering the case (though still not guaranteeing) that they are Y dwarfs: CWISEP 0238–1332 ($J - \text{ch2} > 5.13$), CWISEP 0321+6932 ($J - \text{ch2} > 5.23$), CWISEP 0940+5233 ($J - \text{ch2} > 5.50$), CWISEP 1446–2317 ($J - \text{ch2} > 6.56$), and CWISEP 1935–1546 ($J - \text{ch2} > 6.17$). Another four motion-confirmed candidates with $\text{ch1}-\text{ch2} \geq 2.40$ mag have $J - \text{ch2}$ limits corresponding to minimum colors that would be extremely red among the latest T dwarfs: CWISEP 0402–2651 ($J - \text{ch2} > 4.89$), WISENF 1936+0408 ($J - \text{ch2} > 4.88$),

CWISEP 2011–4812 ($J - \text{ch2} > 4.76$), and CWISEP 2230 +2549 ($J - \text{ch2} > 4.87$). Lastly, four targets with type estimates $\geq Y0$ have J nondetections establishing relatively weak $J - \text{ch2}$ limits in the 3.35–3.70 mag range (CWISEP 0634+5049, CWISEP 0859+5349, CWISEP 1047+5457, and CWISEP 1359–4352). Clearly, deeper J -band imaging follow-up would be highly valuable in pinning down which side of the T/Y boundary each of our $\geq Y0$ phototype discoveries falls on.

None of our $\geq Y0$ phototype targets have detections at the H band. Three of our $\geq Y0$ phototype targets have H nondetections establishing $H - \text{ch2}$ limits in the range of 3.1–3.75 mag (CWISEP 0938+0634, CWISEP 2011–4812, and CWISEP 2356–4814). While these color limits are consistent with spectral type Y, they are essentially uninformative; an $H - \text{ch2}$ limit would need to reach $\gtrsim 5$ mag in order to begin disfavoring late-T spectral types (e.g., Kirkpatrick et al. 2019a; Figure 4).

None of our $\geq Y0$ phototype targets have detections at K or K_S . Eight such objects have K/K_S nondetections establishing weak $K - \text{ch2}$ (or $K_S - \text{ch2}$) limits in the range of 1.97–3.14 mag. A lack of bright K/K_S counterparts is consistent with these eight $\geq Y0$ phototype targets being very late T or Y dwarfs.

Table 12 lists 24 of our motion-confirmed discoveries that we believe merit further follow-up to better refute or confirm their status as Y dwarf candidates. There are three subclasses of objects listed in Table 12. Within each of the three subclasses, our discoveries are listed from reddest (top) to bluest (bottom) in terms of $\text{ch1} - \text{ch2}$ color. The first 17 targets are those with *Spitzer*-based phototypes $\geq Y0$. We include CWISEP 2355 +3804 in this list, even though its $J - \text{ch2}$ color suggests a more likely spectral type of late T. The second class of Y dwarf candidates listed are those sufficiently red to have $\text{ch1} - \text{ch2}$ colors within 1σ of our phototyping grid’s T/Y boundary at $\text{ch1} - \text{ch2} = 2.4$ mag, excluding candidates with J detections establishing $J - \text{ch2} < 5$ mag. There are four such discoveries. The final class of possible Y dwarf candidates listed are those not within 1σ of the T/Y color boundary but nevertheless having measured $\text{ch1} - \text{ch2}$ redder than that of the bluest known Y dwarf in terms of this color³³ and lacking a J detection establishing $J - \text{ch2} < 5$ mag. Three of our discoveries fall in this category. We emphasize that Table 12 targets in the latter two groups of Y dwarf candidates are likely to be late-T dwarfs, but they nevertheless stand out as our most plausible Y dwarf candidates in the $2.1 \lesssim \text{ch1} - \text{ch2} \lesssim 2.4$ regime, where T and Y dwarfs overlap considerably.

The Table 12 column labeled $[(\text{ch1} - \text{ch2}) - 2.4] / \sigma_{\text{ch1} - \text{ch2}}$ measures how much redder/bluer each candidate is than the adopted T/Y boundary at $\text{ch1} - \text{ch2} = 2.4$ in units of each target’s *Spitzer* color uncertainty $\sigma_{\text{ch1} - \text{ch2}}$. This metric helps provide a sense of how certain we can be about whether each object is a T dwarf versus a Y dwarf. Five of our targets with phototype $\geq Y0$ are redder than our grid’s T/Y boundary by more than 2σ . Much more follow-up is warranted in order to better measure/constrain the spectral types of the Y dwarf candidates presented in this section.

³³ For the bluest $\text{ch1} - \text{ch2}$ color of any known Y dwarf, we adopt a value of $\text{ch1} - \text{ch2} = 2.11$, corresponding to the Y0 dwarf WISE 2056+1459. Here WISE 1141–3326 (type Y0) has a bluer reported color of $\text{ch1} - \text{ch2} = 1.76 \pm 0.04$ (Kirkpatrick et al. 2019a), but this anomaly is thought to result from blending with a background source (Tinney et al. 2018).

10.6. Fastest-moving Discoveries

The median μ_{tot} of our motion-confirmed targets is 490 mas yr^{-1} . At the high-motion tail of this distribution, three of our discoveries have best-fit $\mu_{\text{tot}} > 1''.5 \text{ yr}^{-1}$ (CWISEP 0905–7400, CWISEP 1130+3139, and WISE 1534–1043). An additional nine of our motion-confirmed discoveries have $1''.0 \text{ yr}^{-1} < \mu_{\text{tot}} < 1''.5 \text{ yr}^{-1}$. Of our motion-confirmed discoveries, WISEA 1534–1043 has the highest total motion ($\mu_{\text{tot}} = 2697 \pm 68 \text{ mas yr}^{-1}$) and reduced proper motion ($H_{\text{ch2}} = 22.92 \pm 0.06 \text{ mag}$). The five largest H_{ch2} values among our sample all belong to objects with $\text{ch1} - \text{ch2} \leq 1.26$ mag, meaning that these targets occupy the bluest 20% of our sample in terms of $\text{ch1} - \text{ch2}$ color. Figure 10 shows a ch2 reduced proper-motion diagram for all of our motion-confirmed targets with *Spitzer* imaging available, plus the entire sample of Y dwarfs from the prior literature for context. While our targets with phototypes $\geq Y0$ generally inhabit the $18 \lesssim H_{\text{ch2}} \lesssim 21.5$ regime broadly consistent with that of literature Y dwarfs, none of our very red ($\text{ch1} - \text{ch2} > 2.4$ mag) Y dwarf candidates come within 2 mag of WISE 0855–0714 in terms of H_{ch2} .

Using the Section 10.2 distance estimates, we obtain many V_{tan} values well exceeding the typical “high kinematics” threshold of 100 km s^{-1} (e.g., Faherty et al. 2009). Twenty-seven (13, 8, 4, 2) of our motion-confirmed discoveries have central V_{tan} estimates in excess of 100 (150, 200, 300, 400) km s^{-1} . As discussed in Section 10.9, we suspect that many of our highest V_{tan} discoveries may be low-metallicity, subluminoous objects, in which case, their true tangential velocities would be lower than we have derived using the Kirkpatrick et al. (2019a) $M_{\text{ch2}}(\text{ch1} - \text{ch2})$ relation.

10.7. Nearest Discoveries

Our sample’s only object with a central distance estimate placing it within 10 pc is CWISEP 1935–1546 (Table 11). However, with $d = 9.8^{+1.5}_{-1.3} \text{ pc}$, CWISEP 1935–1546 may well reside outside of the 10 pc volume. Meanwhile, the poorly constrained color of CWISEP 1446–2317 translates to a distance upper limit of $d < 8.3 \text{ pc}$. Three additional discoveries have central distance estimates falling outside of 10 pc but are within their 1σ lower distance uncertainties of being closer than 10 pc (CWISEP 0402–2651, WISENF 1936+0408, and CWISEP 2256+4002).

10.8. The 20 pc Sample

Completing the 20 pc census at types $\gtrsim T5$ represents a crucial step toward constraining late-type space densities and, ultimately, the low-mass cutoff of the substellar mass function (e.g., Kirkpatrick et al. 2019a). According to Table 11, 21 of our motion-confirmed discoveries have central distance estimates (or a distance upper limit, in the case of CWISEP 1446–2317) within 20 pc. These 21 targets have phototypes ranging from T7.5 to $\geq Y1$. An additional 24 of our motion-confirmed discoveries have central distance estimates larger than 20 pc but are within their 1σ lower distance uncertainties of being closer than 20 pc. Seven of our discoveries have 1σ high distances still contained within 20 pc. Trigonometric distances will be needed to conclusively determine which of our discoveries indeed reside within 20 pc and take these new objects into account when computing space densities. In the absence of trigonometric distances, spectroscopic types could

help refine absolute magnitude and hence distance estimates for our discoveries.

10.9. NIR/Mid-IR Color–Color Plots

Our Section 9 compilation of follow-up and archival JHK/K_S photometry allows us to make a set of NIR/mid-IR color–color plots and thereby identify objects/populations with unusual spectral energy distributions. Figure 7 provides a $J - \text{ch2}$ versus $\text{ch1} - \text{ch2}$ color–color diagram for motion-confirmed targets with *Spitzer* photometry and J -band detections or limits available. By and large, our discoveries are in reasonable agreement with the literature trend for mid-to-late-T dwarfs shown in magenta (Dupuy & Liu 2012). Our sample continues to display a rising $J - \text{ch2}$ trend toward the highest $\text{ch1} - \text{ch2}$ colors (latest spectral types), as anticipated.

However, we note a distinct subpopulation with anomalously large $J - \text{ch2}$ colors ($J - \text{ch2} > 3.5$ mag) given their relatively blue *Spitzer* colors ($\text{ch1} - \text{ch2} < 1.5$ mag) among our sample. Five of our discoveries are clear-cut members of this color outlier population: CWISEP 0156+3255, CWISEP 0505–5913, CWISEP 0700+7838, CWISEP 0905+7400, and WISEA 1534–1043. In all such cases, the measured $J - \text{ch2}$ colors/limits are at least 1.4 mag redder than the Dupuy & Liu (2012) T dwarf trend (middle dashed magenta line in Figure 7).

There are several potential physical explanations for brown dwarf color outliers, including metallicity, low/high gravity, and binarity. Binarity is difficult to judge given our complete lack of trigonometric distances, spectroscopy, and high-resolution imaging follow-up. On the other hand, kinematics can be helpful in assessing whether our color outliers may be unusually old (low metallicity, high gravity) or young (high metallicity, low gravity). Indeed, all five of our color outliers have unusually large reduced proper motions, $H_{\text{ch2}} > 21$ mag (see Figure 10). Only 10 of the 93 discoveries in Figure 7 have $H_{\text{ch2}} > 21$ mag, and five of these are our color outliers, with another three much redder in $\text{ch1} - \text{ch2}$ phototyped as Y dwarfs. Additionally, all five color outliers have estimated $V_{\text{tan}} > 200$ km s^{−1}, suggesting that they may be members of a halo population. In contrast, binarity would lead our V_{tan} estimates to be biased low and also tend to favor relatively low H_{ch2} . Young objects would also preferentially have low kinematics. Thus, the high kinematics of our color outliers provide strong indications that this subsample is old, with relatively low metallicity and high gravity.

Our color outliers bear a striking resemblance to the benchmark T8 subdwarf WISE J200520.38+542433.9 (Mace et al. 2013b), one of the best-characterized mid-to-late-T subdwarfs. Similar to our color outliers, WISE 2005+5424 is unusually red in $J - \text{ch2}$ ($J - \text{ch2} = 5.02 \pm 0.09$ mag) relative to its modest $\text{ch1} - \text{ch2}$ color of $\text{ch1} - \text{ch2} = 1.25 \pm 0.03$ mag. WISE 2005+5424 is shown in Figure 7 as a yellow pentagon and falls squarely amidst our five color outliers. As noted by Mace et al. (2013b), the models of Burrows et al. (2006) do indeed predict that low-metallicity objects with temperatures from 700 to 2200 K will have relatively red $J - \text{ch2}$ colors. We therefore believe that our color outliers are best considered mid-to-late-T subdwarf candidates. If subdwarfs, their lower luminosities would correspond to smaller distances and hence help rein in their exceptionally large V_{tan} values we have derived assuming an $M_{\text{ch2}}(\text{ch1} - \text{ch2})$ relation applicable to typical T dwarfs.

Mace et al. (2013b) considered the ensemble of T dwarf color outliers, suggesting that $J - H$ color is useful in differentiating between old and young objects (see especially their Table 3 and Figure 8). Unfortunately, none of our five subdwarf candidates have an archival H -band detection available. Only CWISEP 1534–1043 has an H -magnitude lower limit, and this corresponds to an uninformative color limit of $J - H < 1.98$ mag. It would be interesting to obtain deeper H -band follow-up of our five late-type subdwarf candidates to determine whether they match the $J - H > -0.2$ mag trend noted by Mace et al. (2013b) for old, low-metallicity T dwarfs.

Figure 8 shows color–color diagrams analogous to Figure 7 but for $H - \text{ch2}$ (left) and $K - \text{ch2}$ (right) rather than $J - \text{ch2}$. These plots provide at best a sanity check showing that the few targets with $H/K/K_S$ detections line up roughly along the expected trends for late-type brown dwarfs. For the most part, our targets either have no archival $H/K/K_S$ imaging available or else obtain weak magnitude limits corresponding to essentially uninformative color limits.

10.10. Notes on Individual Objects

10.10.1. CWISEP J021243.55+053147.2

Among our 18 targets phototyped at $\geq Y0$, 17 have χ^2_{motion} values exceeding our significance threshold for motion confirmation. The remaining candidate with $\text{ch1} - \text{ch2}$ color in the Y dwarf regime is CWISEP 0212+0531. For this object, our *Spitzer* astrometric data point clearly shows that despite its extremely red $\text{ch1} - \text{ch2}$ color, this object is consistent with being stationary (see Figure 5). We do not count CWISEP 0212+0531 among our list of motion-confirmed Y dwarf candidates.

10.10.2. CWISEP J022935.43+724616.4

As noted in Section 7.2, CWISEP 0229+7246 has two ch2 counterparts but just one blended/elongated ch1 counterpart. We therefore consider it likely that CWISEP 0229+7246 is neither a single moving object nor a pair of closely spaced CPM objects but rather some form of contaminant. For completeness, we can check the motion obtained by combining the ch2 center-of-light position with our $W2$ astrometry, as would be appropriate in the closely spaced CPM scenario. The resulting linear motion is $\mu_\alpha = 9 \pm 27$, $\mu_\delta = -29 \pm 26$ mas yr^{−1}. This corresponds to $\chi^2_{\text{motion}} = 1.4$, further disfavoring the close CPM system hypothesis.

10.10.3. CWISEP J144606.62–231717.8

The brown dwarf candidate CWISEP 1446–2317 has the reddest best-fit $\text{ch1} - \text{ch2}$ color among our entire sample, with $\text{ch1} - \text{ch2} = 3.71 \pm 0.44$ mag. While this color nominally rivals that of WISE 0855–0714, the reddest known brown dwarf in $\text{ch1} - \text{ch2}$ and also the coldest known brown dwarf, we cannot claim that CWISEP 1446–2317 may be similarly cold (see Marocco et al. 2020), for additional follow-up/characterization of this source). Our Gemini J -band imaging with FLAMINGOS-2 confirms that CWISEP 1446–2317 is a Y dwarf by establishing a 5σ limit of $J > 22.36$ mag, which corresponds to a 5σ color lower limit of $J - \text{ch2} > 6.56$ mag.

Given our photometric distance constraint of $d < 8.3$ pc (Section 10.2), we sought to perform a custom *WISE*+*Spitzer* astrometric analysis capable of enabling a combined parallax and proper-motion measurement. Our typical linear motion-fitting approach (Section 8) relies on extracting *W2* detections from coadds spanning multiple *WISE* sky passes, posing challenges for parallax measurement, which is best suited to fitting *WISE* astrometry from single exposures or sky passes where the spacecraft position is well defined. Although CWISEP 1446–2317 is extremely faint at *W2* ~ 16 , we nevertheless performed astrometry only on *W2* coadds of single *WISE* sky passes for this target. We also folded in the recently released 2018 NEOWISE *W2* imaging for CWISEP 1446–2317 so as to leverage these two additional *WISE* sky passes. Using the Sanchez et al. (2019) *WISE* coaddition and source detection methodology, we obtained *W2* detections during 11 of the 12 available *WISE* sky passes throughout the 2010–2018 time period. These positional measurements are provided in Table 3. We were unable to extract a CWISEP 1446–2317 *W2* detection corresponding to the 2017 February NEOWISE sky pass.

We combined our 11 epochs of *WISE* astrometry with our *Spitzer* ch2 position from Table 4 to perform a parallax plus proper-motion fit accounting for the *WISE* and *Spitzer* ephemerides. These yielded a motion solution with $\mu_\alpha = -774 \pm 82$, $\mu_\delta = -978 \pm 71$ mas yr⁻¹ and a parallax of -501 ± 248 mas, with $\chi^2 = 17.4$ for 19 degrees of freedom (dof). The negative parallax is clearly neither physical nor statistically significant. Consequently, we revert to the simple linear motion fitting used for the rest of our sample (Section 8.5) when quoting the CWISEP 1446–2317 motion in Table 7. Regardless of the fitting details, the CWISEP 1446–2317 linear motion is detected at very high significance.

We also checked the CatWISE `par_pm` parameter for CWISEP 1446–2317. This provides a parallax estimate based only on *WISE* data spanning 2010–2016 by comparing linear motion fits computed separately for ascending and descending scans, with *WISE* observing from ~ 1 au on opposite sides of the Sun during opposite scan directions. Here CWISEP 1446–2317 has CatWISE `par_pm` = 253 ± 329 mas, which is again not statistically significant. More *Spitzer*-precision astrometric follow-up will be needed to obtain a reliable trigonometric parallax for this source (see Marocco et al. (2020) for additional CWISEP 1446–2317 astrometry).

Figure 11 shows *WISE*, *Spitzer*, Gemini, and VISTA image cutouts illustrating the motion and colors of CWISEP 1446–2317. Note that this figure only shows 2 yr out of the 6 total yr worth of *W1*/*W2* imaging available. The three red circles remain fixed in all panels at the 2010 *WISE*, 2015 *WISE*, and 2019.41 *Spitzer* positions. There is no 2019.41 *Spitzer* counterpart at the 2010 *WISE* position or *WISE* counterpart during either 2011 or 2015 at the *Spitzer* 2019.41 position. The 2015 *W2* position does not appear perfectly consistent with a linear interpolation between the 2010 *W2* and 2019.41 *Spitzer* positions, seemingly dragged slightly southeast by a noise excursion. This underscores the difficulty of performing astrometry for such a faint *W2* source so close to the background noise limit. There is no trace of a counterpart in either *W1*, Gemini *J*, or VISTA *K_S*. The ch1 counterpart shown is very weak, leading to the large uncertainty on our measured

ch1–ch2 color. VISTA provides only a weak $K_S - \text{ch2} > 2.06$ mag limit.

Lastly, it is interesting to compare the reduced proper motion of CWISEP 1446–2317 ($H_{\text{ch2}} = 21.35 \pm 0.12$ mag) to that of the previously known Y dwarf sample. Among all Y dwarfs from the prior literature, only WISE 0855–0714 has a larger H_{ch2} than CWISEP 1446–2317, as can be seen in Figure 10. However, CWISEP 1446–2317 is a very distant second, with the WISE 0855–0714 H_{ch2} being more than 2 mag larger.

10.10.4. WISEA J153429.75–104303.3

In our sample, WISEA 1534–1043 is the fastest-moving discovery by multiple metrics: total linear motion ($\mu_{\text{tot}} = 2697 \pm 68$ mas yr⁻¹), ch2 reduced proper motion ($H_{\text{ch2}} = 22.92 \pm 0.06$ mag), and estimated tangential velocity ($V_{\text{tan}} = 485_{-64}^{+73}$ km s⁻¹). With $J - \text{ch2} > 4.79$ mag and $\text{ch1} - \text{ch2} = 0.93 \pm 0.04$ mag, WISEA 1534–1043 joins a small subpopulation of color outliers within our motion-confirmed sample, as illustrated in Figure 7. As discussed in Section 10.9, we favor an explanation for the unusual properties of WISEA 1534–1043 in which it is a mid-to-late-T subdwarf, based on kinematics and the striking similarity of our color outlier population to the benchmark T8 subdwarf WISE 2005+5424. It is entirely undetected in our Palomar/WIRC *J*-band follow-up, and deeper *J*-band imaging would be useful for establishing just how anomalously red this object is in its $J - \text{ch2}$ color. If WISEA 1534–1043 is indeed a subdwarf, that would place it at a closer distance than our current $38.0_{-4.9}^{+5.6}$ pc estimate and correspondingly reduce its exceptionally large V_{tan} estimate.

Figure 5 includes a scatter plot displaying the measured (R.A., decl.) trajectory of WISEA 1534–1043. For WISEA 1534–1043, we attempted the same *WISE*+*Spitzer* parallax-fitting methodology as used in Section 10.10.3 for CWISEP 1446–2317. In the case of WISEA 1534–1043, the joint parallax plus proper-motion fit yields $\mu_\alpha = -1254 \pm 116$, $\mu_\delta = -2406 \pm 84$ mas yr⁻¹ and a parallax of 329 ± 422 mas, with $\chi^2 = 8.5$ for 9 dof. The lower number of dof results from the fact that we could only extract single sky pass *W2* detections for seven of 12 *WISE* sky passes. Our parallax measurement is not at all statistically significant. No CatWISE `par_pm` parallax estimate is available for WISEA 1534–1043, since this target is wholly absent from the CatWISE catalog. More high-precision astrometric follow-up of WISEA 1534–1043 would help pin down its ch2 absolute magnitude and thereby test our subdwarf hypothesis.

Figure 12 shows *WISE*, *Spitzer*, Palomar, and VISTA image cutouts in the vicinity of WISEA 1534–1043. In this case, we do not smooth the *WISE* images, since the moving target shifts into a position adjacent to much brighter static sources over time. There is an extremely faint, but nonetheless legitimate, *W1* counterpart to WISEA 1534–1043. It is quite blue in ch1–ch2 relative to the bulk of our sample, and it is very well detected in both *Spitzer* channels. There is no trace of a counterpart detection in the NIR panels at the bottom. As mentioned in Section 10.9, deeper *H*-band follow-up would be of interest in determining whether WISEA 1534–1043 matches the $J - H > -0.2$ mag trend noted by Mace et al. (2013b) for mid-to-late-T subdwarfs.

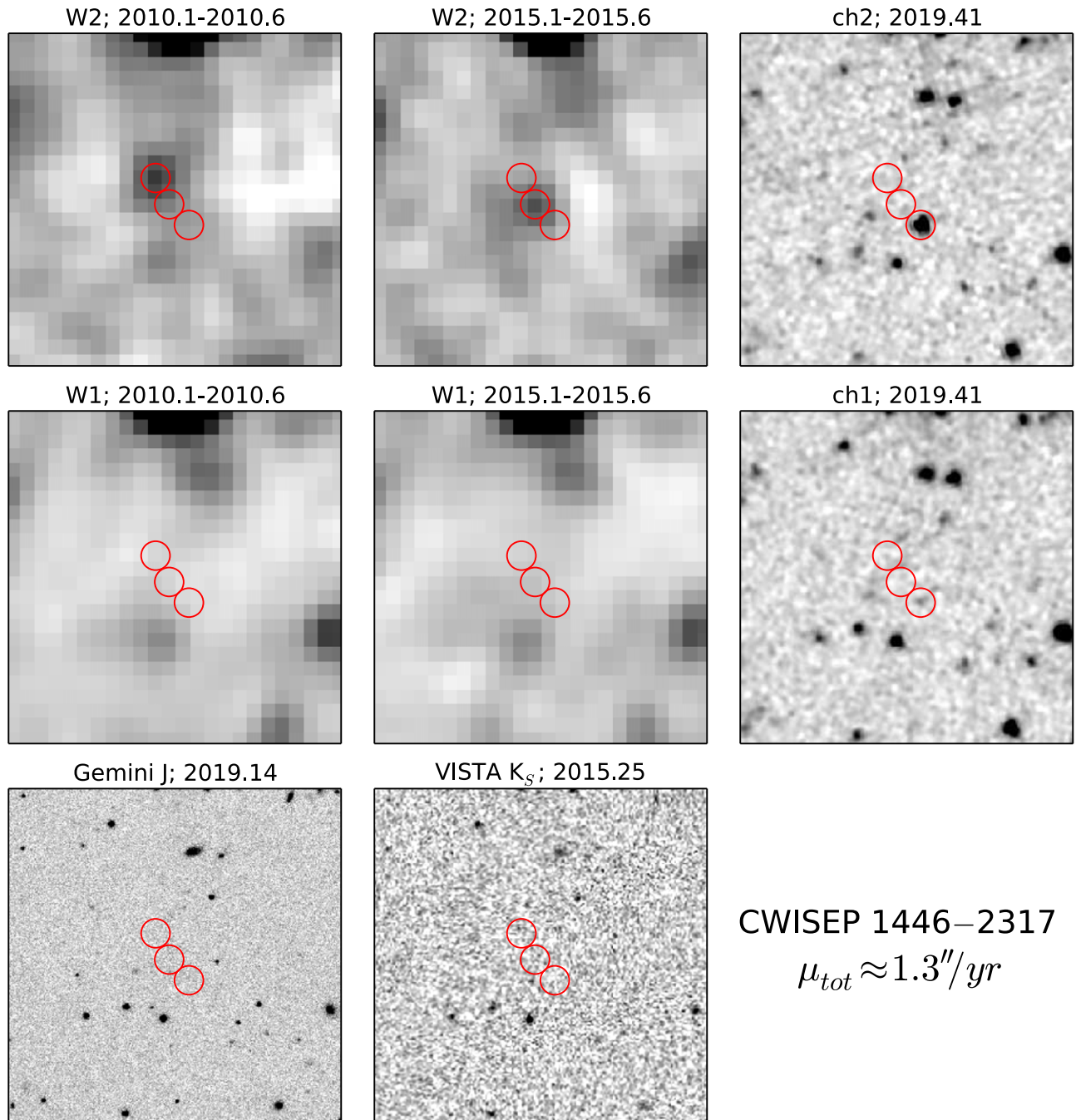


Figure 11. Postage stamps showing available archival and follow-up imaging for CWISEP 1446–2317, our sample’s reddest target in terms of best-fit ch1–ch2 color. Each cutout is $1''.1$ on a side. East is left, and north is up. Within each panel, the red circles indicate the 2010.1–2010.6 *WISE* (northeastern circle), 2015.1–2015.6 *WISE* (middle circle), and 2019.41 *Spitzer* (southwestern circle) positions. In *W1*, Gemini/FLAMINGOS-2 *J*-band follow-up (PI: C. R. Gelino), and archival VISTA K_s imaging from VHS, CWISEP 1446–2317 appears undetected. *Spitzer* imaging comes from our p14034 campaign. The ch1 detection is very weak, leading to a very large uncertainty on the measured ch1–ch2 color. The *WISE* images are 1 yr unWISE meta-coadds, spanning 2010 (2015) in the left (middle) column, and have been smoothed by a $6''.5$ FWHM Gaussian kernel.

10.10.5. CWISEP J154151.59+523025.0

This target has two *Spitzer* counterparts with similar magnitudes in both ch1 and ch2. Further complicating matters, the potentially moving *W2* source appears contaminated by blending with a much bluer stationary object. Additional follow-up would be needed to conclusively determine whether CWISEP 1541+5230 is a pair of red extragalactic sources or two companion brown dwarfs. Both *Spitzer* counterparts, if

assumed to be late-type brown dwarfs, have photometric distances consistent with $d \approx 38$ pc and T8 spectral type estimates. The two *Spitzer* sources are separated by $3''.65$, which would translate to a projected physical separation of 139 au using $d = 38$ pc. If we assume that CWISEP 1541+5230 is a CPM system, then we obtain a linear motion of $\mu_\alpha = 208 \pm 27$, $\mu_\delta = -209 \pm 29$ mas yr $^{-1}$ by fitting the *W2* astrometry in combination with the ch2 center-of-light position.

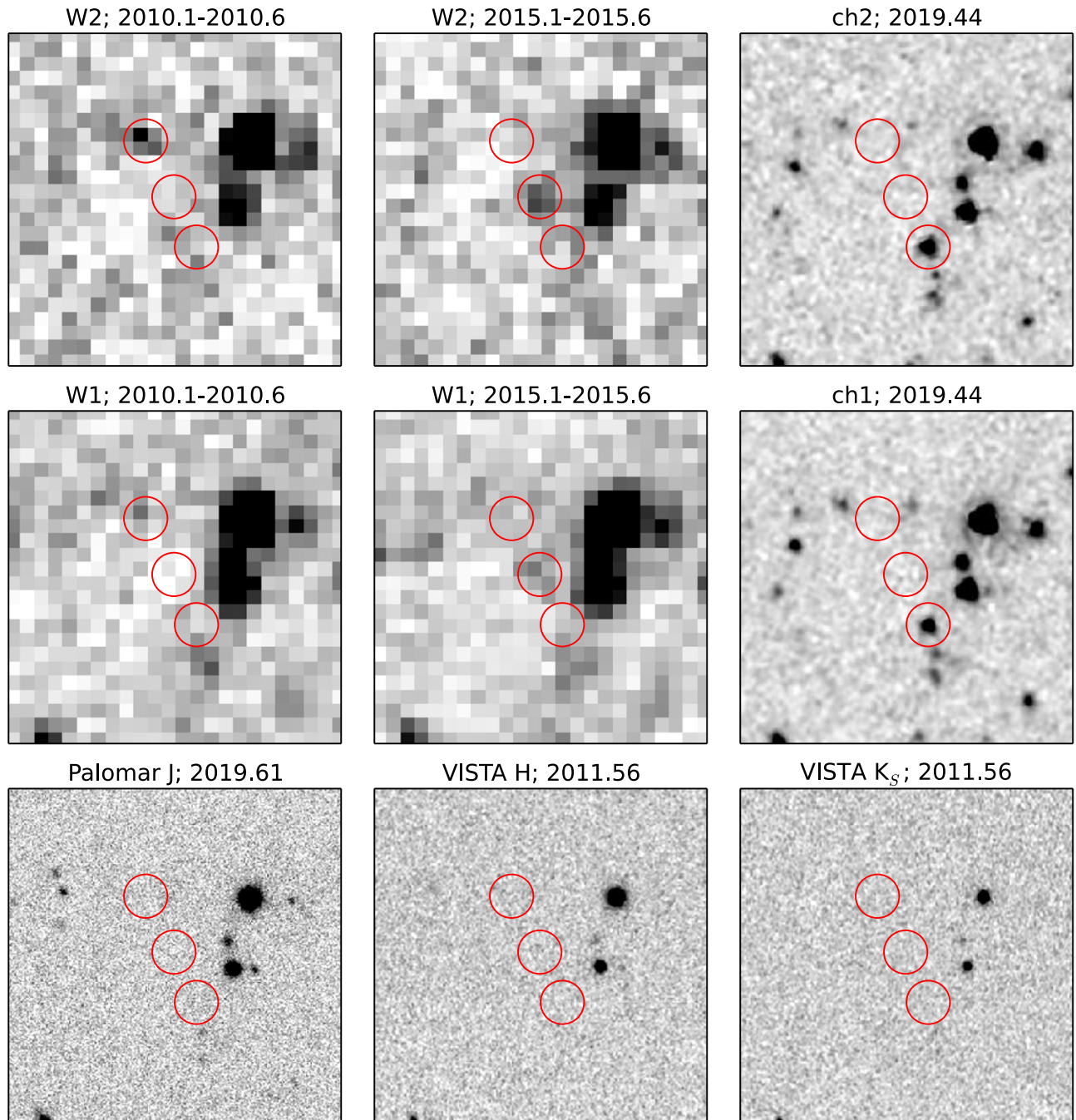


Figure 12. Postage stamps showing available archival and follow-up imaging for WISEA 1534–1043, our sample’s highest proper-motion target ($\mu_{\text{tot}} \approx 2''.7 \text{ yr}^{-1}$), which also has the largest ch2 reduced proper motion of any target in our sample ($H_{\text{ch2}} \approx 22.9 \text{ mag}$). Each cutout is $1''.1$ on a side. East is left, and north is up. Within each panel, the red circles indicate the 2010.1–2010.6 *WISE* (northeastern circle), 2015.1–2015.6 *WISE* (middle circle), and 2019.44 *Spitzer* (southwestern circle) positions. It has an extremely faint *W1* counterpart. It is undetected in our Palomar/WIRC *J*-band follow-up (PI: F. Marocco) and archival VISTA *H* and *K_S* imaging from VHS. *Spitzer* imaging comes from our p14034 campaign. Interestingly, this source has a relatively bright ch1 counterpart, occupying an unusual region of color-color space with $\text{ch1} - \text{ch2} < 1$ and $J - \text{ch2} > 4.5$. The *WISE* images are 1 yr unWISE meta-coadds, spanning 2010 (2015) in the left (middle) column. In this case, the *WISE* images are kept unsmoothed for clarity because the target moves into a position adjacent to much brighter static sources over time.

10.10.6. CWISEP J193518.59–154620.3

Our p14034 photometry of CWISEP 1935–1546 yielded an exceptionally red, though very noisy, *Spitzer* color estimate of $3.24 \pm 0.31 \text{ mag}$ (Marocco et al. 2019). Because this color interval overlapped with that of the coldest known brown dwarf (WISE 0855–0714; $\text{ch1} - \text{ch2} = 3.55 \pm 0.07$), we obtained much deeper ch1 imaging via *Spitzer* DDT program 14279 (p14279; PI: F. Marocco). We also obtained additional ch2 astrometry via observations executed immediately back-to-

back with those of p14279, allowing us to measure a much higher S/N color based on nearly simultaneous imaging in both IRAC bands. These additional ch2 astrometric observations were part of DDT program 14224 (p14224; PI: Kirkpatrick). Our total p14279 ch1 integration time was 3600 s, as compared to just 210 s with p14034.

Combining the p14279 and p14224 data acquired on 2019 August 7, we obtain a refined color measurement of $\text{ch1} - \text{ch2} = 2.984 \pm 0.034 \text{ mag}$. So the original CWISEP 1935

–1546 color from p14034 appears to have scattered $\sim 1\sigma$ relative to the more accurate value now in hand. In Table 1, we list the newer, higher-S/N CWISEP 1935–1546 ch1–ch2 color rather than that from p14034. This color places CWISEP 1935–1546 squarely in the Y1 phototype regime, with a corresponding photometric distance estimate of $9.8^{+1.3}_{-1.3}$ pc. This also corresponds to a $V_{\text{tan}} = 14^{+4}_{-3}$ km s $^{-1}$ estimate that is significantly refined relative to that initially presented in Marocco et al. (2019). Despite being the third reddest motion-confirmed discovery in our entire sample by central ch1–ch2 color, CWISEP 1935–1546 has the lowest H_{ch2} among our motion-confirmed targets with $\geq Y0$ phototypes.

11. Conclusion

We have undertaken an extensive effort to mine the CatWISE proper-motion catalog—and, more generally, the combined WISE +NEOWISE data set—to discover extremely cold brown dwarfs hitherto overlooked by prior searches. By leveraging the 6.5+ yr time baseline afforded by the combination of prehibernation and postreactivation W1/W2 imaging, we are able to perform much deeper motion-based brown dwarf selections than prior all-sky WISE moving-object surveys. As a result, we have discovered many faint moving objects with exceptionally red *Spitzer* colors and hence extremely cold temperatures. Based on *Spitzer* ch1–ch2 color measurements and WISE+*Spitzer* motion validation, our sample contains 17 newly discovered motion-confirmed brown dwarfs with best-fit spectral types $\geq Y0$, 16 of which have $J - \text{ch2}$ detections/limits consistent with being Y dwarfs. Much more follow-up will be required in order to determine which of our Y dwarf candidates listed in Table 12 are indeed Y dwarfs and ultimately obtain spectral types.

One of our Y dwarf candidates, CWISEP 1446–2317, stands out from the rest with an exceptionally large, though very uncertain, *Spitzer* color of ch1–ch2 = 3.71 ± 0.44 . This source in particular merits additional follow-up to refine its photometry and astrometry (see Marocco et al. 2020 for additional characterization of this source).

Table 12 illustrates that deeper J -band follow-up will help push many of our Y dwarf candidates securely into a $J - \text{ch2}$ regime so red as to exclude late-T dwarfs. Further astrometric follow-up will be highly valuable on a number of fronts. Trigonometric parallaxes will provide absolute magnitudes that can discriminate between late-T and Y spectral types. Trigonometric parallaxes will also be necessary to determine which of our discoveries fall within the 20 pc volume and incorporate these into accurate space density estimates. Deeper H -band imaging follow-up will be particularly useful in determining whether our sample of fast-moving color outliers are indeed mid-to-late-T subdwarfs, as we have hypothesized.

We anticipate many more very late type CatWISE brown dwarf discoveries in the future. A second and final CatWISE data processing is underway, expected to catalog an additional ~ 1 billion WISE-selected objects by virtue of more aggressive source detection/deblending. However, *Spitzer* is a uniquely efficient resource for obtaining spectral type estimates of such discoveries, and upon *Spitzer*'s retirement, it will become much more challenging to sift for promising Y dwarf candidates among W2-only moving objects.

The upcoming decade will provide exciting opportunities to discover and characterize the coldest ($T_{\text{eff}} \lesssim 300$ K) substellar constituents of the solar neighborhood (e.g., Kirkpatrick et al. 2019b; Leggett et al. 2019). The community will need to select

JWST Y dwarf targets of maximum scientific value to better understand both brown dwarfs themselves and giant exoplanet atmospheres (Leggett et al. 2019). The Near Earth Object Surveyor (formerly NEOCam) will be able to reveal colder, fainter, and more distant Y dwarfs than WISE given resources for coadded processings analogous to those of AllWISE/unWISE/CatWISE (Kirkpatrick et al. 2019b). Determining the low-mass cutoff of star formation will require a complete sample out to distances of 20–50 pc (Leggett et al. 2019), far beyond the volume currently mapped (Kirkpatrick et al. 2019a). CatWISE is already making progress on these fronts by mining the WISE/NEOWISE data set for Y dwarf discoveries to its faintest attainable depths.

We wish to thank the anonymous referee. We thank Nicholas Cross for assistance with compiling archival UKIRT/VISTA detections. This research was partially carried out at the Jet Propulsion Laboratory, California Institute of Technology, under a contract with NASA.

CatWISE is funded by NASA under Proposal No. 16-ADAP16-0077 issued through the Astrophysics Data Analysis Program and uses data from the NASA-funded WISE and NEOWISE projects. A.M.M. acknowledges support from Hubble Fellowship HST-HF2-51415.001-A. F.M. is supported by an appointment to the NASA Postdoctoral Program at the Jet Propulsion Laboratory, administered by the Universities Space Research Association under contract with NASA.

This work is based in part on observations made with the *Spitzer Space Telescope*, which is operated by the Jet Propulsion Laboratory, California Institute of Technology, under a contract with NASA.

Based in part on observations obtained at the Gemini Observatory, which is operated by the Association of Universities for Research in Astronomy, Inc., under a cooperative agreement with the NSF on behalf of the Gemini partnership: the National Science Foundation (United States), National Research Council (Canada), CONICYT (Chile), Ministerio de Ciencia, Tecnología e Innovación Productiva (Argentina), Ministério da Ciência, Tecnologia e Inovação (Brazil), and Korea Astronomy and Space Science Institute (Republic of Korea).

Facilities: *Spitzer*(IRAC), WISE/NEOWISE, Gemini(FLAMINGOS-2), Hale(WIRC), UKIRT(WFCAM), VISTA(VIRCAM), 2MASS.

Software: XGBoost (Chen & Guestrin 2016), MOPEX (Makovoz & Khan 2005; Makovoz & Marleau 2005), WiseView (Caselden et al. 2018).

ORCID iDs

Aaron M. Meisner  <https://orcid.org/0000-0002-1125-7384>
 J. Davy Kirkpatrick  <https://orcid.org/0000-0003-4269-260X>
 Federico Marocco  <https://orcid.org/0000-0001-7519-1700>
 Michael C. Cushing  <https://orcid.org/0000-0001-7780-3352>
 Edward L. Wright  <https://orcid.org/0000-0001-5058-1593>
 Jacqueline K. Faherty  <https://orcid.org/0000-0001-6251-0573>
 Edward F. Schlafly  <https://orcid.org/0000-0002-3569-7421>

References

- Abbott, T. M. C., Abdalla, F. B., Allam, S., et al. 2018, *ApJS*, 239, 18
 Beichman, C., Gelino, C. R., Kirkpatrick, J. D., et al. 2013, *ApJ*, 764, 101
 Bertin, E., & Arnouts, S. 1996, *A&AS*, 117, 393

- Burningham, B. 2018, *Handbook of Exoplanets* (Cham: Springer), 118
- Burrows, A., Sudarsky, D., & Hubeny, I. 2006, *ApJ*, 640, 1063
- Caselden, D., Westin, P., III, Meisner, A., Kuchner, M., & Colin, G. 2018, *WiseView: Visualizing Motion and Variability of Faint WISE Sources*, Astrophysics Source Code Library, ascl:1806.004
- Chambers, K. C., Magnier, E. A., Metcalfe, N., et al. 2016, arXiv:1612.05560
- Chen, T., & Guestrin, C. 2016, in Proc. 22nd ACM SIGKDD Int. Conf. Knowledge Discovery and Data Mining, KDD '16 (New York: ACM), 785
- Cushing, M. C., Kirkpatrick, J. D., Gelino, C. R., et al. 2011, *ApJ*, 743, 50
- Cutri, R. M., Mainzer, A., & Conrow, T. 2015, Explanatory Supplement to the NEOWISE Data Release Products, Tech. Rep.
- Cutri, R. M., Wright, E. L., & Conrow, T. 2013, Explanatory Supplement to the AllWISE Data Release Products, Tech. Rep.
- Dey, A., Schlegel, D. J., Lang, D., et al. 2019, *AJ*, 157, 168
- Dupuy, T. J., & Liu, M. C. 2012, *ApJS*, 201, 19
- Dupuy, T. J., Liu, M. C., & Leggett, S. K. 2015, *ApJ*, 803, 102
- Dye, S., Lawrence, A., Read, M. A., et al. 2018, *MNRAS*, 473, 5113
- Edge, A., Sutherland, W., Kuijken, K., et al. 2013, *Msngr*, 154, 32
- Eikenberry, S., Elston, R., Raines, S. N., et al. 2006, *Proc. SPIE*, 6269, 626917
- Eisenhardt, P. R. M., Marocco, F., Fowler, J. W., et al. 2019, arXiv:1908.08902
- Faherty, J. K., Burgasser, A. J., Cruz, K. L., et al. 2009, *AJ*, 137, 1
- Fazio, G. G., Hora, J. L., Allen, L. E., et al. 2004, *ApJS*, 154, 10
- Gaia Collaboration, Brown, A. G. A., Vallenari, A., et al. 2018, *A&A*, 616, A1
- Gardner, J. P., Mather, J. C., Clampin, M., et al. 2006, *SSRv*, 123, 485
- Griffith, R. L., Kirkpatrick, J. D., Eisenhardt, P. R. M., et al. 2012, *AJ*, 144, 148
- Hodgkin, S. T., Irwin, M. J., Hewett, P. C., & Warren, S. J. 2009, *MNRAS*, 394, 675
- Kirkpatrick, J. D. 2005, *ARA&A*, 43, 195
- Kirkpatrick, J. D., Cushing, M. C., Gelino, C. R., et al. 2011, *ApJS*, 197, 19
- Kirkpatrick, J. D., Gelino, C. R., Cushing, M. C., et al. 2012, *ApJ*, 753, 156
- Kirkpatrick, J. D., Kellogg, K., Schneider, A. C., et al. 2016, *ApJS*, 224, 36
- Kirkpatrick, J. D., Martin, E. C., Smart, R. L., et al. 2019a, *ApJS*, 240, 19
- Kirkpatrick, J. D., Metchev, S. A., Hillenbrand, L. A., et al. 2019b, *BAAS*, 51, 108
- Kirkpatrick, J. D., Schneider, A., Fajardo-Acosta, S., et al. 2014, *ApJ*, 783, 122
- Kuchner, M. J., Faherty, J. K., Schneider, A. C., et al. 2017, *ApJL*, 841, L19
- Lang, D. 2014, *AJ*, 147, 108
- Lawrence, A., Warren, S. J., Almaini, O., et al. 2007, *MNRAS*, 379, 1599
- Leggett, S., Apai, D., Burgasser, A., et al. 2019, *BAAS*, 51, 95
- Leggett, S. K., Morley, C. V., Marley, M. S., et al. 2013, *ApJ*, 763, 130
- Lépine, S., Shara, M. M., & Rich, R. M. 2002, *AJ*, 124, 1190
- Liu, M. C., Dupuy, T. J., Bowler, B. P., Leggett, S. K., & Best, W. M. J. 2012, *ApJ*, 758, 57
- Luhman, K. L. 2013, *ApJL*, 767, L1
- Luhman, K. L. 2014a, *ApJ*, 781, 4
- Luhman, K. L. 2014b, *ApJL*, 786, L18
- Luhman, K. L., Burgasser, A. J., & Bochanski, J. J. 2011, *ApJL*, 730, L9
- Mace, G. N., Kirkpatrick, J. D., Cushing, M. C., et al. 2013a, *ApJS*, 205, 6
- Mace, G. N., Kirkpatrick, J. D., Cushing, M. C., et al. 2013b, *ApJ*, 777, 36
- Mainzer, A., Bauer, J., Cutri, R., et al. 2014, *ApJ*, 792, 30
- Mainzer, A., Bauer, J., Grav, T., et al. 2011a, *ApJ*, 731, 53
- Mainzer, A., Cushing, M. C., Skrutskie, M., et al. 2011b, *ApJ*, 726, 30
- Makovoz, D., & Khan, I. 2005, in ASP Conf. Ser. 347, *Astronomical Data Analysis Software and Systems XIV*, ed. P. Shopbell, M. Britton, & R. Ebert (San Francisco, CA: ASP), 81
- Makovoz, D., & Marleau, F. R. 2005, *PASP*, 117, 1113
- Marocco, F., Caselden, D., Meisner, A. M., et al. 2019, *ApJ*, 881, 17
- Marocco, F., Kirkpatrick, J. D., Meisner, A. M., et al. 2020, *ApJL*, 888, L19
- Martin, E. C., Kirkpatrick, J. D., Beichman, C. A., et al. 2018, *ApJ*, 867, 109
- McMahon, R. G., Banerji, M., Gonzalez, E., et al. 2013, *Msngr*, 154, 35
- Meisner, A. M., Lang, D., Schlafly, E. F., & Schlegel, D. J. 2019, *PASP*, 131, 124504
- Meisner, A. M., Lang, D., & Schlegel, D. J. 2018a, *RNAAS*, 2, 1
- Meisner, A. M., Lang, D., & Schlegel, D. J. 2018b, *AJ*, 156, 69
- Meisner, A. M., Lang, D. A., & Schlegel, D. J. 2018c, *RNAAS*, 2, 202
- Patten, B. M., Stauffer, J. R., Burrows, A., et al. 2006, *ApJ*, 651, 502
- Pinfield, D. J., Gomes, J., Day-Jones, A. C., et al. 2014a, *MNRAS*, 437, 1009
- Pinfield, D. J., Gromadzki, M., Leggett, S. K., et al. 2014b, *MNRAS*, 444, 1931
- Sanchez, J. A., Reddy, V., Thirouin, A., et al. 2019, *ApJL*, 881, L6
- Schlafly, E. F., Meisner, A. M., & Green, G. M. 2019, *ApJS*, 240, 30
- Schneider, A. C., Greco, J., Cushing, M. C., et al. 2016, *ApJ*, 817, 112
- Tinney, C. G., Faherty, J. K., Kirkpatrick, J. D., et al. 2012, *ApJ*, 759, 60
- Tinney, C. G., Kirkpatrick, J. D., Faherty, J. K., et al. 2018, *ApJS*, 236, 28
- Werner, M. W., Roellig, T. L., Low, F. J., et al. 2004, *ApJS*, 154, 1
- Wilson, J. C., Eikenberry, S. S., Henderson, C. P., et al. 2003, *Proc. SPIE*, 4841, 451
- Wright, E., Eisenhardt, P., Mainzer, A., et al. 2010, *AJ*, 140, 1868
- Wright, E. L., Mainzer, A., Kirkpatrick, J. D., et al. 2014, *AJ*, 148, 82